The Manipulation of Hydrophobicity in Catalyst Design for Applications of Aerobic Alcohols Oxidation and Electrocatalytic Water Oxidation

Dissertation by
Batian Chen

In Partial Fulfillment of the Requirements
For the Degree of
Doctor of Philosophy

King Abdullah University of Science and Technology
Thuwal, Kingdom of Saudi Arabia, 2016

The dissertation of Batian Chen is approved by the examination committee.

Committee Chairperson: Prof. Valentin O. Rodionov

Committee Co-Chair: Prof. Nikolaos Hadjichristidis

Committee Member: Prof. Kazuhiro Takanabe

Committee Member: Prof. Mikhail Moshkov

Committee Member: Prof. Vlamidir Sidorov

ABSTRACT

The Manipulation of Hydrophobicity in Catalyst Design for Applications of

Aerobic Alcohols Oxidation and Electrocatalytic Water Oxidation

Batian Chen

Hydrophobicity is the generalized characteristic of non-polar substances that brings about their exclusion from aqueous phases. This property, entropic in its nature, drives key self-assembly and phase separation processes in water. Protein folding, the formation of DNA double helix, the existence of lipid bilayers and the wetting properties of leaf surfaces are all due to hydrophobic interactions. Inspired by Nature, we aimed to use hydrophobicity for creating novel and improved catalytic systems.

(I) A number of fluorous amphiphilic star block-copolymers containing a tris(benzyltriazolylmethyl)amine motif have been prepared. These polymers assembled into well-defined nanostructures in water, and their mode of assembly could be controlled by changing the composition of the polymer. The polymers were used for enzyme-inspired catalysis of alcohol oxidation.

(II) An enzyme-inspired catalytic system based on a rationally designed multifunctional surfactant was developed. The resulting micelles feature metal-binding sites and stable free radical moieties as well as fluorous pockets that attract and preconcentrate molecular oxygen. In the presence of copper ions, the micelles effect

chemoselective aerobic alcohol oxidation under ambient conditions in water, a transformation that is challenging to achieve nonenzymatically.

(III) Development of a facile means of photo/electrocatalytic water splitting is one of the main barriers to establishing of a solar hydrogen economy. Of the two half-reactions involved in splitting water into O_2 and H_2, water oxidation presents the most challenge due to its mechanistic complexity. A practical water oxidation catalyst must be highly active, yet inexpensive and indefinitely stable under harsh oxidative conditions. Here, I shall describe the synthesis of a library of molecular water oxidation catalysts based on the Co complex of tris(2-benzimidazolylmethyl)amine, $(BimH)_3$. A wide range of catalysts differing in their electronic properties, surface affinity, and steric bulk was explored. We identified hydrophobicity as the key variable in mediating the catalytic competence of Co-$(BimH)_3$ complexes. The change in this parameter correlates both with the conformational mobility of the ligand core and the structural changes in the local solvent environment around the catalytic metal site. The optimal ligand identified is superhydrophobic due to three fluorinated side chains. The corresponding Co complex catalyzes water electrooxidation efficiently, with an onset potential equal to that for the well-established CoPi heterogeneous system, albeit with a dramatically higher turnover frequency (TOF) and in the absence of soluble Co salts. As an added benefit, the hydrophobic catalyst can be immobilized through physisorption, and remains stable after prolonged controlled-potential electrolysis. A DFT calculation was also performed to understand the catalytic pathway.

ACKNOWLEDGEMENTS

This work would not have been possible without the support, help, and encouragement I have received from many people.

First of all, I am deeply grateful to my supervisor Prof. Valentin O. Rodionov for his continuous support and encouragement of my PhD study and research, for teaching me with new ways of thinking about science, for sharing his enthusiasm in chemistry, and also for his wonderful Physical Organic Chemistry class. None of this work would have been possible without him.

I am grateful to my committee members: Professors Nikolaos Hadjichristidis, Kazuhiro Takanabe, Mikhail Moshkov and Vladimir Sidorov for helpful discussions and suggestions.

I would like to thanks Prof. Luigi Cavallo for his advices in DFT calculations and also an amazing Theoretical Chemistry class.

My thanks also go to Dr. Konstantin Bukhryakov for his assistance in organic synthesis. To Dr. Clément Mugemana and Yogesh Patil for their help with polymer synthesis. And to Dr. Natalia Morlanés for her great contribution in electrochemistry.

Thanks to all the rest members that are working or used to work in Rodionov group: Vera A. Solovyeva, John-Paul O'Shea, Kif Merican, Khanh B. Vu, Sarah R. Almahdali, Tianyou Chen and Mykyta Tretiakov for helpful discussions, advices, and most importantly, for making the lab with a lot of fun.

TABLE OF CONTENTS

LIST OF ABBREVIATIONS

Abbreviation	Name/description
(BimH)$_3$	tris(2-benzimidazolylmethyl)amine
AFM	atomic force microscopy
ATR-FTIR	attenuated total reflectance–fourier transform infrared spectroscopy
BnOH	benzyl alcohol
bpy	2,2'-bipyridine
CPE	controlled potential electrolysis
Cryo-TEM	cryogenic transmission electron microscopy
CTAB	cetyl trimethylammonium bromide
CV	cyclic voltammogram
DABCO	1,4-diazabicyclo[2.2.2]octane
DBU	1,8-diazabicyclo[5.4.0]undec-7-ene
DFT	density functional theory
DIPEA	N,N-diisopropylethylamine
DLS	dynamic light scattering
DMAP	4-dimethylaminopyridine
DMF	dimethylformamide
DMSO	dimethylsulfoxide
DO	dissolved oxygen
ESI	electrospray ionization
FBA	2,2,3,3,4,4,4-heptafluorobutyl acrylate
FDA	1H,1H,2H,2H-perfluorodecyl acrylate
FE	faradaic efficiency
FS	2,3,4,5,6-pentafluorostyrene
FTO	fluorine-doped tin oxide
GC-MS	gas chromatography – mass spectrometry
HOMO	highest occupied molecular orbital
HRMS	high resolution mass spectrometry
i_{cat}	catalytic current density
ICP	inductively coupled plasma spectroscopy
idiff	diffusional current density

LC-MS	liquid chromatography – mass spectrometry
LUMO	lowest unoccupied molecular orbital
MeCN	acetonitrile
M_n	number-average molecular weight
M_w	weight-average molecular weight
NHE	normal hydrogen electrode
NMI	N-methylimidazole
NMP	nitroxide-mediated polymerization
NMR	nuclear magnetic resonance spectroscopy
OEGMa	oligo(ethylene glycol) methacrylate
OEGSt	oligo(ethylene glycol) styrene
PCET	proton-coupled electron transfer
PDI	polydispersity index
PS	polystyrene
PTFE	polytetrafluoroethylene
RHE	reversible hydrogen electrode
RID	refractive index detector
SDS	sodium dodecyl sulfate
SEC	size exclusion chromatography
SHE	standard hydrogen electrode
SPM	scanning probe microscopy
TBTA	tris[(1-benzyl-1H-1,2,3-triazol-4-yl)methyl]amine
TCD	thermal conductivity detector
TEMPO	2,2,6,6-tetramethyl-1-piperidinyloxyl
THF	tetrahydrofuran
TLC	thin-layer chromatography
TMS	tetramethylsilane
TOF	turnover frequency
TON	turnover number
UV-Vis	ultraviolet-visible absorption spectroscopy
WNA	water nucleophilic attack
WO	water oxidation
WOC	water-oxidation catalyst
Γ	surface loading, mol / cm^2

LIST OF SCHEMES

LIST OF FIGURES

LIST OF TABLES

Chapter 1.

Introduction – Hydrophobicity and Catalysis

1.1 Hydrophobicity

1.1.1 The Origin of Hydrophobicity

In chemistry, hydrophobicity is the generalized characteristic of non-polar substances that is seemingly repelled from aqueous phases.[1] The hydrophobic interaction, in its nature, is mostly an entropic effect.

Water molecule has an electrical dipole moment (1.84 D) and tend to form hydrogen bonding network with each other. However, water molecules are not able to form hydrogen bonds with non-polar substances such as a alkyl chain or a nonpolar domain of a large molecule. Therefore, such a non-hydrogen bonding motif in water will cause disruption in the hydrogen bonding network among the surrounding water molecules. The water molecules tend to rearrange and interact as much as possible with themselves, thus results in clumps of non-polar substances to minimize their surface area which exposed to aqueous phase and also lower the whole system's entropy.[2] Hence, hydrophobic substances usually cluster together in water and form complex aggregates such as micelles. On hydrophobic surfaces, water will exhibit a high contact angle.

1.1.2 The Hydrophobicity of Fluorocarbons

Hydrophobic substances are usually lipophilic, silicones and fluorocarbons are exceptions, which are both hydrophobic and lipophobic.

Fluorocarbons are organofluorine compounds with the formula C_xF_y.[3] Fluorine is the most electronegative element in the periodic table, which results in the low polarizability of fluorocarbons. Also, fluorocarbons have extremely low intermolecular attractive forces and are especially hydrophobic, as well as lipophobic,[4] due to their weak susceptibility to the fleeting dipoles. Hence, immiscibility of fluorocarbons with both water and hydrocarbons are expected.

In addition to the hydrophobicity and lipophobicity, fluorocarbons are also compressible and demonstrate a good ability to dissolve gases such as oxygen and carbon dioxide, making them of great interest in the field of blood substituents and gas carriers. This property will also be discussed in **Chapter 2**.

1.2 Enzymes: Catalysis in Hydrophobic Pockets

1.2.1 The Structure and Properties of Enzymes
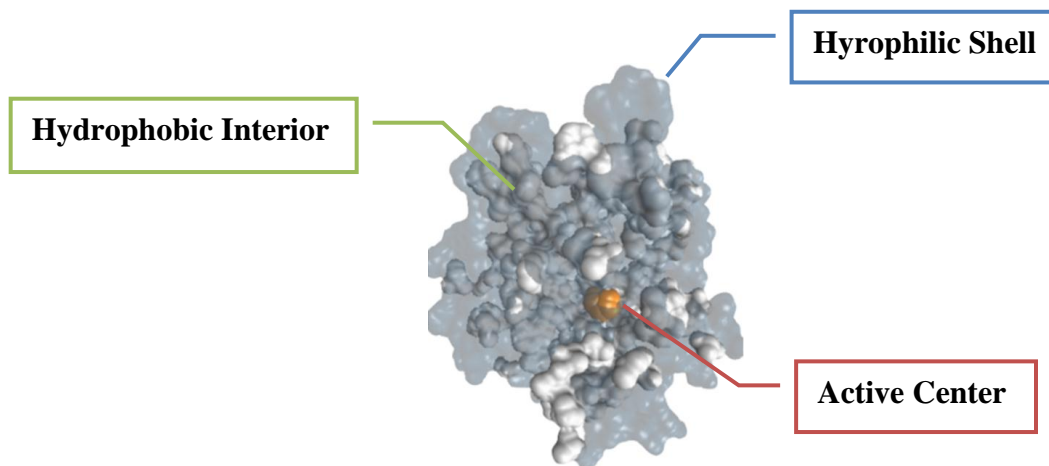
Figure 1.1 A representative structure of enzymes.

Nature's enzymes are extremely efficient catalysts that are capable of facilitating thousands of challenging reactions with perfect fidelity and selectivity. They are generally globular proteins, acting alone or in larger complexes. Their exquisite level of functionality is achieved through precise, programmed folding into intricate tertiary structures[5] and close participation of cofactors, prosthetic groups and metal ions. Often, the active sites and cofactor binding pockets are separated from the bulk aqueous phase and buried in the hydrophobic interior of the protein.

Hydrophobic effect is essential to the understanding of the protein folding and enzyme structures. Hydrophobic amino acids, including alanine, leucine, isoleucine, tryptophan, valine, methionine and phenylalanine (**Figure 1.2**) tend to cluster together within the protein. The resulting structures of proteins have their hydrophobic side chains buried

from water, while charged and polar side chains stayed on the surface and exposed to water molecules. In other words, the principal driving force of the protein folding process is to minimize the exposure of hydrophobic side chains to water.[6]
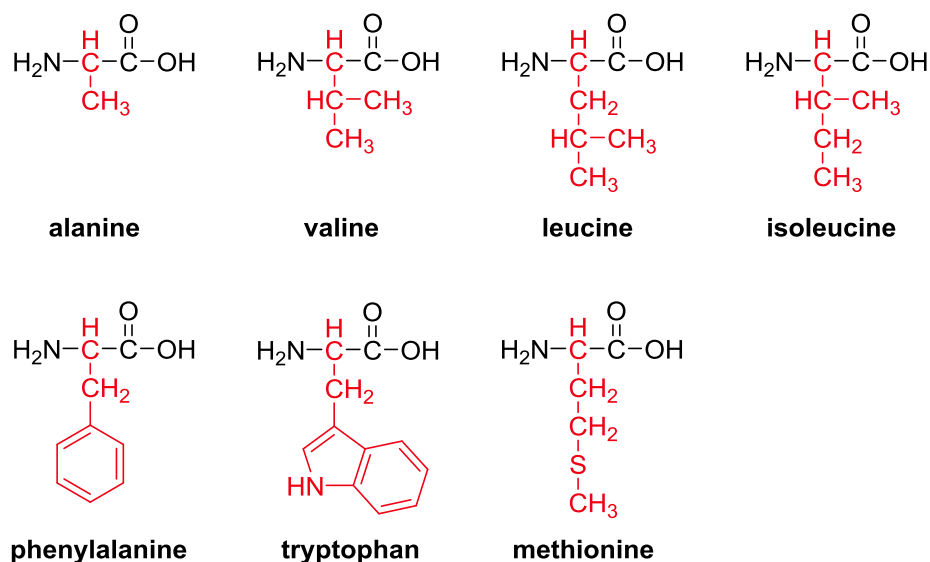
Figure 1.2 Hydrophobic amino acids. The hydrophobic components are marked as red.

1.2.2 Galactose Oxidase

In **Chapter 2**, two enzyme-inspired catalytic systems for aerobic oxidation of primary alcohols to aldehydes will be described. Herein, I would like to have a brief introduction about how nature does the same job.

Galactose oxidase (GO) is a well-studied enzyme that perform two-electron redox chemistry using a copper (II)-tyrosyl radical unit.[7] GO catalyze the oxidation of primary alcohols to aldehydes in physiological condition coupling with the reduction of O_2 to H_2O_2 (**Scheme 1.1**). The substrate for GO is not limited with D-galactose, it also

catalyzed a wide range of substrates such as aliphatic alcohols, aromatic alcohols and sugars. The oxidation is extremely regioselective, no secondary alcohols are oxidized.

$$R\diagup OH \xrightarrow{\text{GO; } O_2;\ \text{r.t.}} R\diagup O \ + \ H_2O_2$$
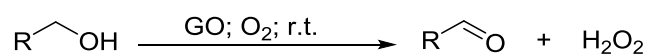
Scheme 1.1 Aerobic oxidation of primary alcohols to aldehydes catalyzed by galactose oxidase.

Mature GO is a monomer containing one copper center per protein, its molecular mass is 68 kDa. In the active site of GO, a mononuclear Cu ion was bound by Tyr272, Tyr495, His496, His581 and also a water molecule to form a distorted five-coordinate metal center.[7] The X-ray structure of the "inactive" form of GO and its mechanism[8] are shown in **Figure 1.3**.
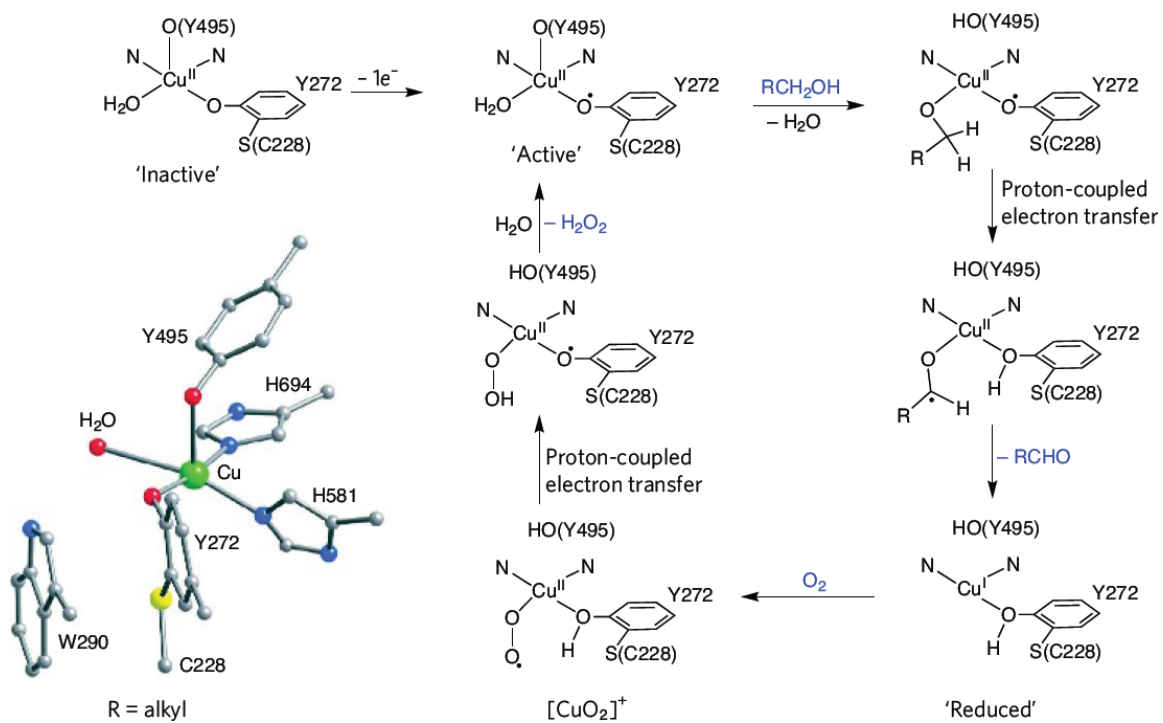
Figure 1.3 Aerobic alcohol oxidation mechanism catalyzed by GO.

1.3 Micellar Catalysts: Catalysts Inspired by Enzymes

1.3.1 The Self-assembly of Amphiphiles in Water

Amphiphiles are molecules that compose of both hydrophobic and hydrophilic domains, such as small molecule surfactants and block copolymers. In water, amphiphiles tend to form aggregates with their hydrophobic domains clumping to each other and their hydrophilic domains pointing to aqueous phase. The morphology and size of the self-assembled aggregates are a function of many factors: (i) the composition ratio of hydrophobic and hydrophilic parts, (ii) the molecular structure/geometry and (iii) the solution conditions such as amphiphile concentration, temperature, pH, and ionic strength.[9] The typical morphologies of self-assembled aggregates include spherical micelles, vesicles, cylindrical micelles, bilayer sheets and etc. (**Figure 1.4**)
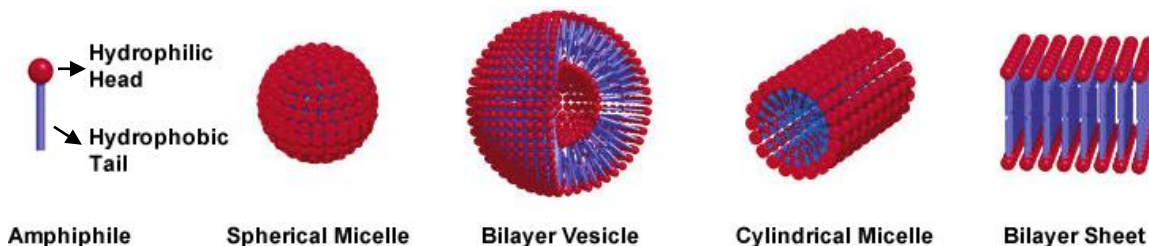
Figure 1.4 Typical morphologies of aggregates self-assembled from amphiphiles.

1.3.2 Micellar Catalysts

Micelles, vesicles and emulsion droplets have gained a lot of attention in the catalysis field and are referred as to micellar catalysts.[10, 11] They are capable of solubilizing both polar and nonpolar reactants and impact the rate and (stereo)selectivity of a reaction in

that way, due to the polarity difference between the hydrophobic core of a micelle and its hydrophilic surface.[12] The enhancement impact could be ascribed to the following phenomena: (i) increase local concentration of the reactants in the interior of the micelle or at the surface; (ii) stabilize the transition state of a reaction by a favorable interaction with the surfactant molecules; and (iii) a combined polarity, charge effect and microviscosity inside the micelle.[13]

From a certain point of view, micellar catalysts have a lot in common with enzymes: (i) nanoscale sizes, (ii) consist of hydrophobic core and hydrophilic shell, (iii) encapsulate substrates and isolate species from the bulk solvent, (iv) compartmentalize and enhance local concentration of substrates and (v) catalyze reactions in water.[11]

1.4 Catalysis on Hydrophobic Surface

1.4.1 Water on Hydrophobic Surface

When put a drop of water on different surfaces, it will exhibit different contact angles. For water droplet on ceramic or bare metallic surfaces, the droplet will completely spread out on the solid surface (the contact angle is ~ 0 °), because of the strong attraction between water molecules and the solid molecules. Generally, we considered the solid surface as hydrophilic if the contact angle of the water droplet on the surface is smaller than 90 °. If the contact angle of water droplet on the surface is larger than 90 °, then we considered the solid surface hydrophobic.[14]

By incorporation of various inorganic and organic materials onto the surfaces, the wetting contact angle could be controlled. Surfaces modified with surface energy materials such as perfluorinated carbon tails may have water contact angles as high as ~120°. A water contact angle greater than 150° could even be reached by using some materials with highly rough surfaces, due to the air pockets under the liquid drop. These are called superhydrophobic surfaces, such as the leaves of the lotus plant.

1.4.2 Hydrophobic Catalysts

The wettability of heterogeneous catalysts on surfaces plays important roles in reactions involving polar molecules (e.g. water, alcohols) as reactant, product or solvent. The surface wettability regulates the interaction between catalysts, substrates and polar molecules and thus has a great impact on the reaction activity and selectivity. Many examples of this kind have been reported. For instances, Xiao group and Liu group has demonstrated that hydrophobic solid acid catalysts were excellent catalysts for esterification[15] and trans-esterification.[16] Corma group has shown that the epoxidation reaction could catalyzed by hydrophobic molecular sieve with enhanced activity and selectivity,[17] etc.

Therefore, the special interaction between water molecules and hydrophobic surfaces makes it of great interest to study the reaction of water (such as water oxidation) catalyzed by a hydrophobic catalyst. This part of work will be described in **Chapter 3**.

Chapter 2.

Enzyme-Inspired Nanoreactors with Hydrophobic Interior for Chemoselective Aerobic Oxidation of Primary Alcohols to Aldehydes in Water

2.1 Introduction

The chemoselective oxidation of primary alcohols to the corresponding aldehydes is among the most important reactions in chemical and pharmaceutical industrial processes. To date, vary oxidation reagents and catalysts have been developed,[18] however, stoichiometric expensive and polluting oxidants (notably Cr^{IV} based reagents) are usually implemented. Therefore, the development of transition metal catalyzed aerobic oxidation[19, 20] which utilizing oxygen (or even better air) as stoichiometric oxidant is of great interest, not only for economic benefit but also environmental concerns.

Cu/TEMPO catalyst systems, first introduced by Semmelhack[21] in 1984 and further developed by Sheldon,[22] Stahl[23] and other groups[24] have recently emerged as some of the most effective catalysts for chemoselective aerobic alcohol oxidation (**Scheme 2.1**). In spite of many advantages these systems have achieved so far (high conversion, selectivity,

and turn over frequency; wide scope, tolerance of many functional groups; under room temperature and ambient pressure), they are still facing challenges such as tedious product separation and the involvement of environmental unfriendly and flammable (higher risk when along with oxygen) organic solvent. Thus, it is highly desirable to further improve these systems to be greener, safer and practical in aqueous medium.[25]
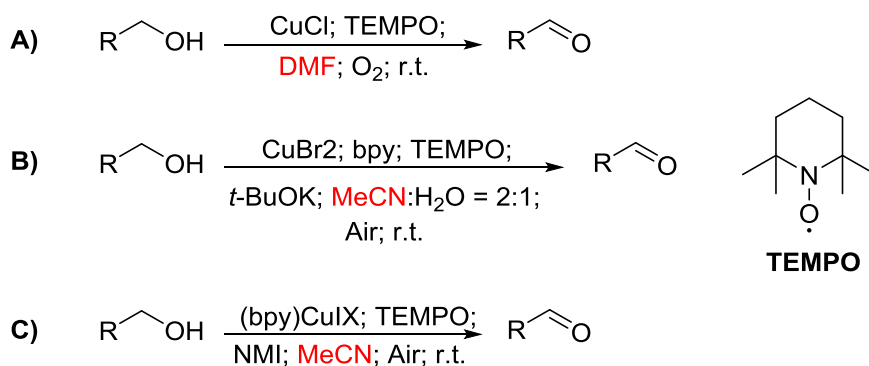
Scheme 2.1 Cu/TEMPO catalytic systems developed by **(A)** Semelhack group; **(B)** Sheldon group; **(C)** Stahl group.

Similar with the strategy of Sheldon's Pd-catalyzed aerobic alcohol oxidation system in water (**Scheme 2.2**),[26] some efforts trying to introduce Cu/TEMPO systems into water have been reported by several groups recently (**Scheme 2.3**).[27, 28] Typically, elevated pressure, high temperature and water-soluable ligands were implemented to increase the oxygen concentration, enhance the substrate/catalyst solubility and lower the transition-state barrier.
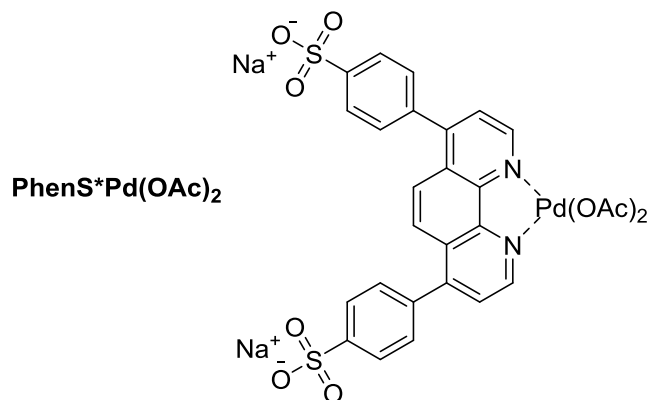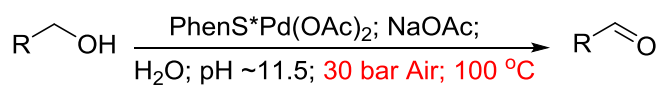
Scheme 2.2 Aerobic oxidation using a water soluble catalyst.
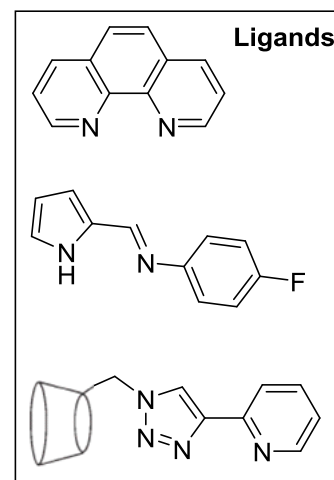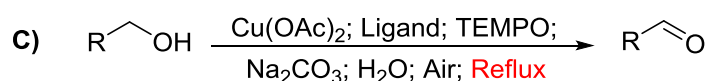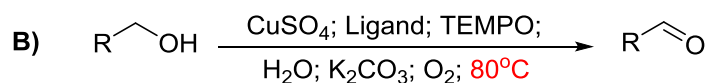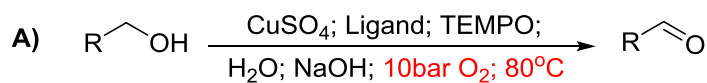
Scheme 2.3 Several attempts trying to transfer Cu/TEMPO catalytic system into water.

Different with these protocols, we aimed to design enzyme-inspired micellar catalysts that could enable the transfer of this catalytic system to pure water. Such a transfer could enable large-scale applications of Cu/TEMPO, while circumventing the usual safety concerns associated with combining oxygen and organic solvents. Two enzyme-inspired

catalytic materials based on star block-copolymers and functional surfactants will be presented.

2.2 Nanoreactors Self-assembled from Three-Arm Star Block-copolymers[29]

In this section, we present a pathway to enzyme-inspired catalytic materials based on star block-copolymers with limited branching. These polymers incorporate hydrophilic, superhydrophobic, and polydentate metal-binding characteristics. The interplay of these structural characteristics determines the mode of self-assembly and the catalytic competence of the macromolecules.
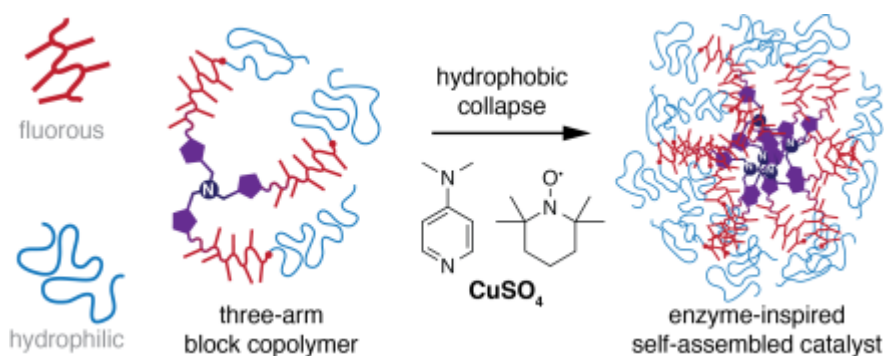
Figure 2.1 Amphiphilic block copolymer micelle with metal binding sites at the core.

2.2.1 Synthesis and Characterization of Star Block Copolymers

We envisioned that amphipolar, globular assemblies, with metal-binding sites buried inside hydrophobic cores (**Figure 2.1**), could provide the necessary site isolation of the catalytic metal centers.[30-32] However, the accumulation of hydrophobic reaction products inside such assemblies would be undesirable, as the transfer of additional alcohol

substrate to the active site would be hindered. To avoid this potential problem, we chose "everything-phobic" fluorous monomers as building blocks for the cores of our prospective catalysts.[33, 34] Understanding that perfluorocarbons and their emulsions in water are capable of dissolving substantial amounts of O_2,[35, 36] we reasoned that a fluorous core of a polymer globule could pre-concentrate oxygen in the vicinity of the active metal site.
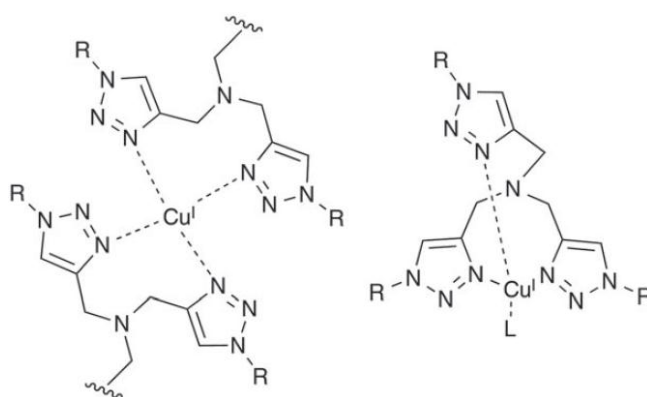
Figure 2.2 Some of the modes of coordination possible for a TBTA-type ligand.

We selected the tris(benzyltriazolylmethyl) amine (TBTA) motif[37] as a metal-binding site, due to its ability to stabilize the Cu^I oxidation state, its versatile coordination chemistry[38, 39] (**Figure 2.2**), and its easy synthetic accessibility. Starting with the TBTA-based polymerization initiator (**Figure 2.3**, upper left), we proceeded to synthesize a number of superhydrophobic three-arm polymers via nitroxide-mediated polymerization (NMP).[40] We chose this mode of polymerization over synthetically simpler atom-transfer radical polymerization,[41] as the latter can be affected by the presence of Cu^I binding sites in the target polymers.
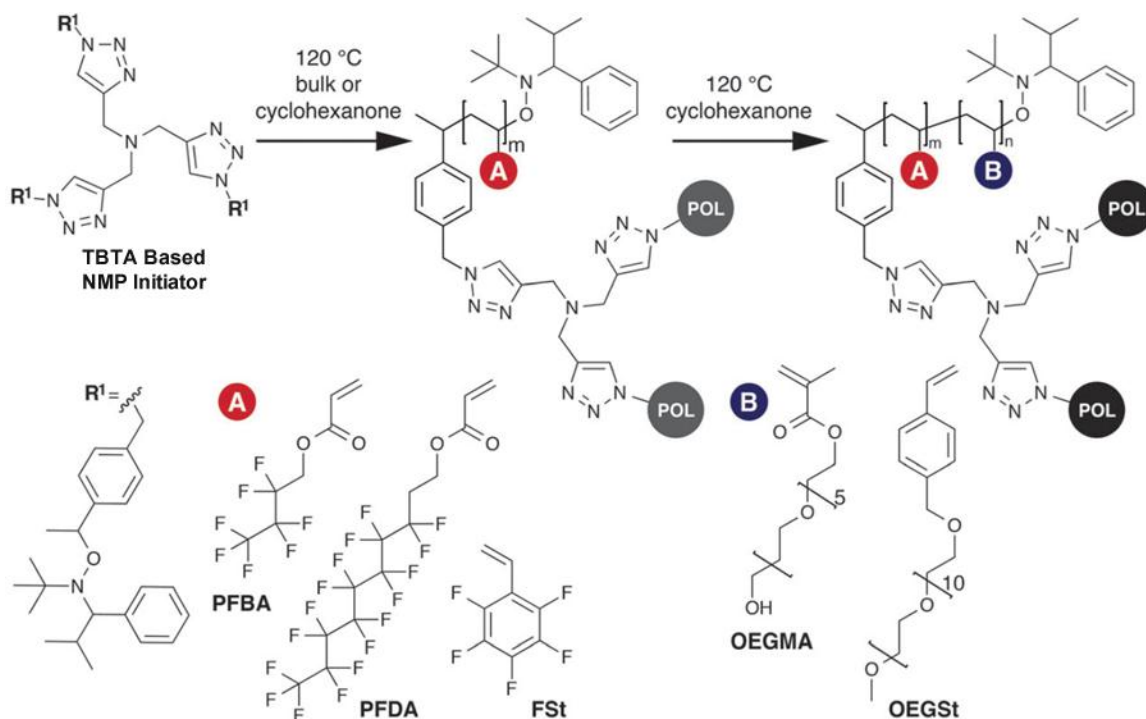
Figure 2.3 Synthesis of amphiphilic star block copolymers.

Pentafluorostyrene (PFS), 2,2,3,3,4,4,4-heptafluorobutyl acrylate (PFBA) and 1*H*,1*H*,2*H*,2*H*-perfluorodecyl acrylate (PFDA) were polymerized with the TBTA-based NMP initiator, either in the bulk or in cyclohexanone at 120 °C. For each fluorinated monomer, we aimed to create at least two macroinitiators with different degrees of polymerization (DP) to evaluate the effects of the hydrophobic core size on catalytic competency (**Table 2.1**). A DP higher than 4 could not be reached for PFDA due to the anomalously low solubility of resulting polymers.

Table 2.1 Characterization of hydrophobic macroinitiators.

Entry	Polymer	$M_n{}^a$	$M_w{}^a$	PDI_{SEC}	DLS $(nm)^b$	PDI_{DLS}
1	$(PFS_7)_3$	3843	4260	1.10	-	-
2	$(PFS_{10})_3$	5550	6380	1.16	-	-
3	$(PFS_{16})_3$	7950	9650	1.20	40	0.5

4	(PFBA$_7$)$_3$	4154	4710	1.13	-	-
5	(PFBA$_{14}$)$_3$	7782	9100	1.17	50	0.8
6	(PFBA$_{20}$)$_3$	9209	10126	1.11	90[c]	0.4
7	(PFDA$_4$)$_3$	7125	7651	1.08	30	0.5

[a] Determined by SEC. Calibration was performed against linear polystyrene. [b] Diameter of macroinitiators obtained by DLS in DMF at 1g/l. [c] Diameter of macroinitiators obtained by DLS in trifluorotoluene at 1g/l.

The hydrophobic macroinitiators were used for the polymerization of two hydrophilic monomers, *p*-oligo(ethylene glycol) styrene (OEGSt) and oligo(ethylene glycol) methacrylate (OEGMA). OEGSt was polymerized in cyclohexanone, leading to a range of amphiphilic star copolymers (**Table 2.2**, Entries 1-5). Although NMP is rarely a polymerization of choice for methacrylates,[42] we obtained a higher DP for the copolymerization of OEGMA than we did for styrenic OEGSt (**Table 2.2**, Entries 6-9). Size exclusion chromatography (SEC) on all the copolymerization reactions indicated a clean shift of population towards a higher number-average molecular weight (M$_n$), with little to no tailing (although limited aggregation was observed for (PFDA$_4$-*b*-OEGSt$_4$)$_3$ and (PFBA$_{20}$-*b*-OEGSt$_4$)$_3$).

Table 2.2 Characterization of amphiphilic star block copolymers.

Entry	Polymer[a]	M$_n$[b]	M$_w$[b]	PDI$_{SEC}$	DLS (nm)[c]	PDI$_{DLS}$	AFM (nm)[d]	TEM (nm)
1	(PFS$_7$-*b*-OEGSt$_3$)$_3$	5900	6600	1.12	20(90%) / 160(10%)	0.23	76 ±10	20 ±2[f]
2	(PFS$_{10}$-*b*-OEGSt$_4$)$_3$	11200	13216	1.18	28(30%) / 135(70%)	0.22	44 ±6	26 ±2[f]
3	(PFS$_{16}$-*b*-OEGSt$_4$)$_3$	12400	15130	1.22	70(70%) / 130(30%)	0.24	46 ±4	42 ±4[e]
4	(PFBA$_{20}$-*b*-OEGSt$_4$)$_3$	12800	16400	1.28	70	0.36	100 ±14	120-350[f]
5	(PFDA$_4$-*b*-OEGSt$_4$)$_3$	11500	14720	1.28	20(90%) / 140(10%)	0.54	74 ±4	22 ±1[f]
6	(PFS$_{16}$-*b*-OEGMA$_{30}$)$_3$	13500	16470	1.22	120(42%) / 200(58%)	0.22	70 ±6	44 ±8[f]
7	(PFBA$_7$-*b*-OEGMA$_{18}$)$_3$	11230	13360	1.19	30(48%) /	0.28	70 ±8	58 ±10[e]

| 8 | (PFBA$_{14}$-b-OEGMA$_{30}$)$_3$ | 13200 | 15970 | 1.21 | 30(89%) / 250(11%) | 0.29 | 88 ±4 | 52 ±10 [e] |
| 9 | (PFDA$_4$-b-OEGMA$_{30}$)$_3$ | 11000 | 12320 | 1.12 | 40(86%) / 255(14%) | 0.44 | 76 ±10 | 24 ±4 [f] |

Note: the fragment "300(52%)" appears above row 8, associated with the preceding entry's DLS column.

[a] Degree of polymerization determined by ^{1}H NMR. [b] Determined by SEC (calibration against linear polystyrene). [c] Hydrodynamic diameters determined by dynamic light scattering (DLS) in water at 1 g·L^{-1}. For multimodal distributions, diameters are estimated based on intensity distribution, and relative ratios based on volume distribution. [d] Diameters of aggregates determined from AFM height images. [e] Diameter of aggregates determined from TEM images. [f] Diameter of aggregates determined from cryo-TEM images.

We investigated the self-assembly modes of the copolymers by obtaining cryogenic transmission electron microscopy (cryo-TEM) and atomic force microscopy (AFM) images of their aggregates. Spherical aggregates with diameters between 20 and 50 nm were the main type of assemblies for (PFS$_7$-b-OEGSt$_3$)$_3$, (PFS$_{10}$-b-OEGSt$_4$)$_3$, (PFBA$_7$-b-OEGMa$_{18}$)$_3$, (PFBA$_{14}$-b-OEGMa$_{30}$)$_3$, (PFDA$_4$-b-OEGMa$_{30}$)$_3$, and (PFS$_{16}$-b-OEGMA$_{30}$)$_3$ (**Figure 2.4a-c**, **Section 2.2.4.4** and **2.2.4.5**). AFM phase images (**Figure 2.4b** and **Section 2.2.4.4**) revealed the separation between the hydrophobic aggregate cores and hydrophilic coronas. The size of the aggregates observed was consistent between cryo-TEM and AFM, taking into account the flattening/spreading of soft material on the substrate (**Table 2.2**).
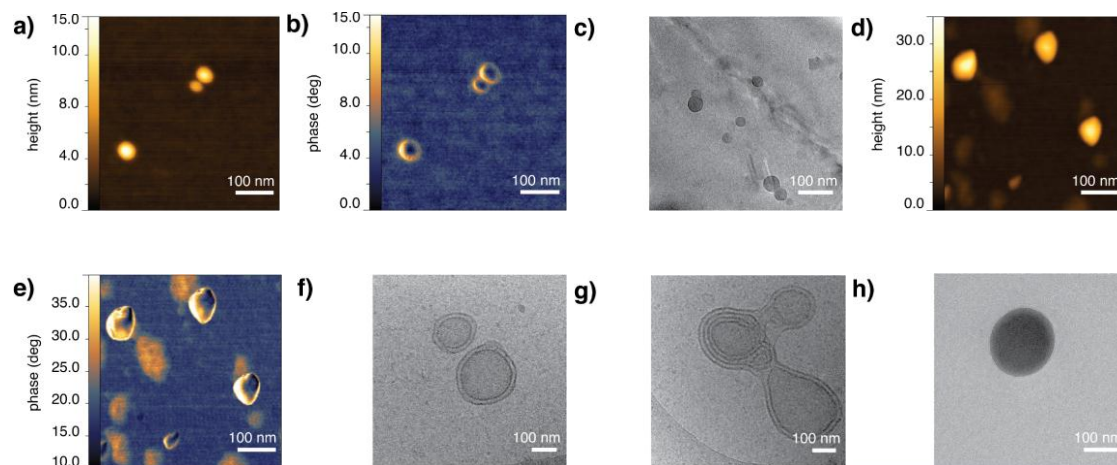
Figure 2.4 a) and b) AFM height and phase images of $(PFS_{16}\text{-}b\text{-}OEGMA_{30})_3$ block copolymer micelles spin-coated onto Si substrate. c) Cryo-TEM image of $(PFS_{16}\text{-}b\text{-}OEGMA_{30})_3$ block copolymer micelles in water. d) and e) AFM height and phase images of $(PFBA_{20}\text{-}b\text{-}OEGSt_4)_3$ vesicular structures. f) and g) Cryo-TEM images of $(PFBA_{20}\text{-}b\text{-}OEGSt_4)_3$ vesicular structures, unilamellar and multilamellar. h) Cryo-TEM image of a $(PFBA_{20}\text{-}b\text{-}OEGSt_4)_3$ vesicle in the presence of $CuSO_4$.

We found that by increasing the weight fraction of the fluorinated block in the copolymer, more complex morphologies could be triggered. $(PFBA_{20}\text{-}b\text{-}OEGSt_4)_3$ copolymer, which contains 67 wt % of the fluorous monomer, assembled into well-defined vesicles, unilamellar (**Figure 2.4f**), as well as multilamellar (**Figure 2.4g**). The thickness of the vesicle boundaries was ca. 9 nm, which suggests that they were formed by a single layer of macromolecules. The AFM image of $(PFBA_{20}\text{-}b\text{-}OEGSt_4)_3$ showed that some vesicles remain intact even in the partially dry state. Objects with diameters ranging from ca. 60 to 120 nm and with heights from 30 to 40 nm were observed. In addition to the aggregates with pronounced height, flat structures of similar lateral dimensions could be seen (**Figure 2.4d-e**). We presume that some of the vesicles retain their interior water when deposited on the substrate, while others "deflate" and spread. Unlike spherical aggregates, the "deflated" vesicles show no core-corona contrast in the AFM phase image. The vesicular structures persisted after addition of $CuSO_4$. A significant amount of Cu was sequestered in the vesicle's boundary, as is evidenced by the increased contrast in the cryo-TEM image (**Figure 2.4h**).

Examination of aqueous polymer solutions by DLS (see **Section 2.2.4.3**) revealed 20-70 nm aggregates in agreement with AFM and TEM images, as well as larger species with hydrodynamic diameters varying from ca. 100 to 300 nm. It is likely that the larger species are not abundant enough to feature prominently in TEM images, and unravel/disassemble when spread on AFM substrates. Much smaller, 5-20 nm species were observed in the polymer solutions prepared in good organic solvents, such as DMF and THF.

2.2.2 Aerobic Oxidation of Benzyl Alcohol

The catalytic competency of the star polymers was evaluated for a Cu/TEMPO-catalyzed alcohol oxidation reaction, using a modification of the protocol originally reported by Stahl.[8] Polymers were dispersed in water, the "cofactors" TEMPO and 4-dimethylaminopyridine (DMAP) were added, and the solutions were treated with ultrasound. $CuSO_4$ and benzyl alcohol were added to start the reaction. The rate of oxidation was negligible in the absence of the star polymers (**Table 2.3**, Entries 1 and 2). Addition of PFS and PFDA copolymers led to a marginal improvement of reaction yields (**Table 2.3**, Entries 3, 5 and 7). To our delight, the TEMPO/Cu system became catalytically competent in the presence of star polymers with PFBA hydrophobic cores (**Table 2.3**, Entries 4, 6 and 8). The nature of the hydrophilic monomer, the degree of polymerization, or the weight fraction of the fluorinated monomer had little influence on the catalytic competency: $(PFBA_{20}$-b-$OEGSt_4)_3$, $(PFBA_7$-b-$OEGMA_{18})_3$, and $(PFBA_{14}$-b-$OEGMA_{30})_3$ were similar in their capacity for catalyzing alcohol oxidation. Upon further

optimization of reaction conditions (**Table 2.3**, Entries 9-12), an almost quantitative yield of benzaldehyde was obtained in the presence of (PFBA$_{14}$-*b*-OEGMA$_{30}$)$_3$.

Table 2.3 Catalytic oxidation of benzyl alcohol in the presence of block-copolymer micellar aggregates.
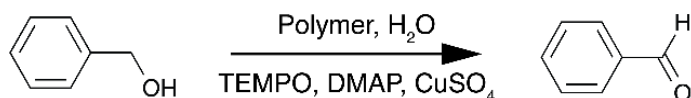
Entry	Block Copolymer	Time [h]	TEMPO [mol %] [a]	DMAP [mol %] [a]	CuSO$_4$ [mol %] [a]	Polymer [*wt* %]	Conversion [%] [b]
1	-	36	1	5	0.2	-	<1
2	-	44	2.5	50	2	-	5
3	(PFS$_{10}$-*b*-OEGSt$_4$)$_3$	36	1	5	0.2	0.04	6
4	(PFBA$_{20}$-*b*-OEGSt$_4$)$_3$	36	1	5	0.2	0.04	28
5	(PFS$_{16}$-*b*-OEMa$_{30}$)$_3$	36	1	5	0.2	0.04	5
6	(PFBA$_7$-*b*-OEGMa$_{18}$)$_3$	36	1	5	0.2	0.04	25
7	(PFDA$_4$-*b*-OEGMa$_{30}$)$_3$	36	1	5	0.2	0.04	6
8	(PFBA$_{14}$-*b*-OEGMa$_{30}$)$_3$	36	1	5	0.2	0.04	22
9	(PFBA$_{14}$-*b*-OEGMA$_{30}$)$_3$	37	2.5	25	4	3.11	46
10	(PFBA$_{14}$-*b*-OEGMA$_{30}$)$_3$	31	2.5	25	2	1.56	53
11	(PFBA$_{14}$-*b*-OEGMA$_{30}$)$_3$	21	5	25	2	1.27	61
12	(PFBA$_{14}$-*b*-OEGMA$_{30}$)$_3$	44	2.5	50	2	1.56	90

[a] Relative to benzyl alcohol. [b] Determined by ^{1}H NMR.

2.2.3 Dissolved Oxygen Capacity

The capacity of the polymers to pre-concentrate molecular oxygen was assessed next. Polymer solutions (2 wt %) were saturated with O$_2$ by vigorous shaking them in vials in an atmosphere of pure oxygen. Following this, the vial headspace was vented, and the concentration of O$_2$ in solution was measured in 5 min intervals using an Inlab 605 probe (Mettler Toledo). For both pure water and (PFS$_{16}$-*b*-OEGSt$_4$)$_3$ solution, the dissolved O$_2$ concentration dropped to its air-saturated value of ~9 mg·L^{-1} in ~25 min (**Figure 2.5**).

Similar equilibration kinetics was observed for the 2 wt % solution of Pluronic P123. Since Pluronic solutions are prone to foaming, the slightly slower O_2 release in this case compared to pure water can be attributed to gas retention in foam bubbles. The behavior of the $(PFBA_{14}\text{-}b\text{-}OEGMA_{30})_3$ solution was markedly different. After 30 min, the dissolved O_2 concentration was still ~20 $mg \cdot L^{-1}$, which is approximately 200% of air-saturated concentration in pure water. This suggests that the catalytic competency of amphiphilic PFBA copolymers is due to their capacity to attract and pre-concentrate O_2 in the hydrophobic environment surrounding the metal-binding site.
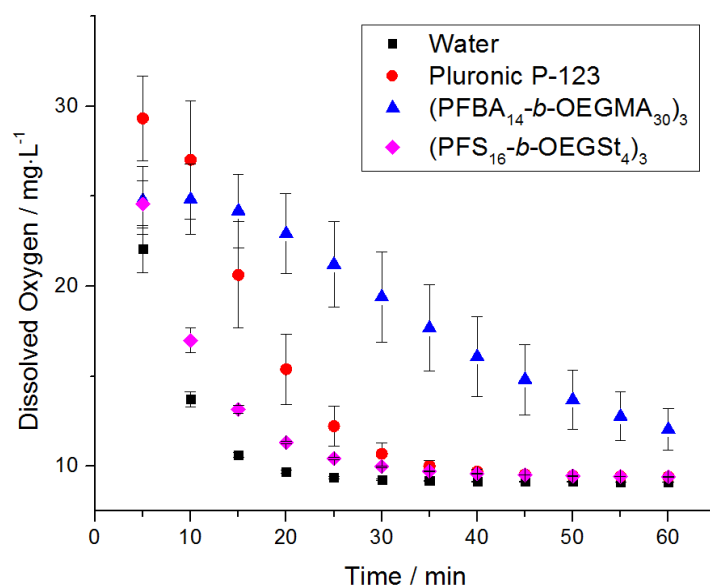
Figure 2.5 The results of dissolved oxygen (DO) measurements.

2.2.4 Experimental Section

2.2.4.1 Materials

Commercial reagents were purchased from Sigma Aldrich or VWR and used without any further purification, unless indicated otherwise. Monomers including styrene,

2,3,4,5,6-pentafluorostyrene, 2,2,3,3,4,4,4-heptafluorobutyl acrylate, and 1H,1H,2H,2H-perfluorodecyl acrylate were purchased from Aldrich and purified over Al_2O_3 (Basic) before use. Poly(ethylene glycol) monomethyl ether (M_n 500) purchased from Aldrich was purified by azeotropic distillation in toluene before use. O-(1-(4-(azidomethyl)phenyl)ethyl)-N-(tert-butyl)-N-(2-methyl-1-phenylpropyl)hydroxylamine was synthesized by a published technique.[43] The synthesis of fluorinated macro-initiators as well as diblock copolymers were adapted from works of Schubert[44] and Boutevin[45], respectively.

2.2.4.2 Synthetic Details of Star Block Copolymers

Tris(((1-(4-(1-((tert-butyl(2-methyl-1-phenylpropyl)amino)oxy) ethyl)benzyl)-1H-1,2,3-triazol-4-yl)methyl)amine
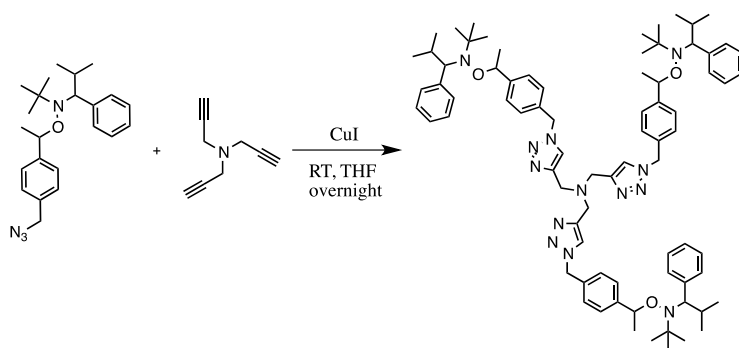
O-(1-(4-(azidomethyl)phenyl)ethyl)-*N*-(*tert*-butyl)-*N*-(2-methyl-1-phenylpropyl) hydroxylamine (1.79 g, 4.7 mmol, 1 eq.) and tripropargylamine (0.2 g, 1.52 mmol, 0.32 eq.) were dissolved in THF (20 mL). Copper iodide (0.09 g, 0.47 mmol, 0.1 eq.) was added and then the reaction mixture was stirred at room temperature under nitrogen. The mixture was analyzed by TLC (hexane/ethyl acetate 19:1) after 16 hours to confirm the

reaction was at completion. QuadraSil® MP (0.5 g) was added and the resulting mixture was stirred for 1 hour to remove copper. The mixture was filtered off, and the filtrate was concentrated under vacuum. The resulting solid residue was then purified by column chromatography, using hexane/ethyl acetate (1:1) as the eluent and giving 1.54 g (78%) of a solid white powder. ^{1}H NMR of diastereomers (400 MHz; CDCl$_3$): δ 7.74 (br s, 3 H), 7.45-7.16 (m, 27 H), 5.50 (d, J = 15.2 Hz, 6 H), 4.93 (dd, J = 6.5, 2.4 Hz, 3 H), 3.74 (br s, 6 H), 3.37 (dd, J = 47.3, 10.7 Hz, 3 H), 2.21-2.36 (m, 3 H), 1.62 (d, J = 6.6 Hz, 3 H), 1.54 (d, J = 6.6 Hz, 3 H), 1.31 (d, J = 6.4 Hz, 3 H), 1.05 (s, 9 H), 0.91 (d, J = 6.3 Hz, 3 H), 0.78 (s, 9 H), 0.55 (d, J = 6.6 Hz, 3 H), 0.22 (t, J = 5.6 Hz, 3 H). ^{13}C NMR (101 MHz; CDCl$_3$): δ 146.4, 145.7, 142.4, 142.1, 133.6, 133.0, 131.0, 130.9, 128.0, 127.9, 127.8, 127.7, 127.5, 127.3, 126.9, 126.9, 126.4, 126.3, 83.1, 82.2, 72.2, 72.1, 60.6, 60.5, 54.1, 54.0, 32.1, 31.8, 28.5, 28.3, 24.8, 23.2, 22.2, 22.0, 21.2, 21.3. MS (ESI+) calculated for [C$_{78}$H$_{106}$N$_{13}$O$_3$]+: 1272.85361, found: 1272.85432.

Poly(2,3,4,5,6-pentafluorostyrene) three-arm star polymer (PFS$_7$)$_3$
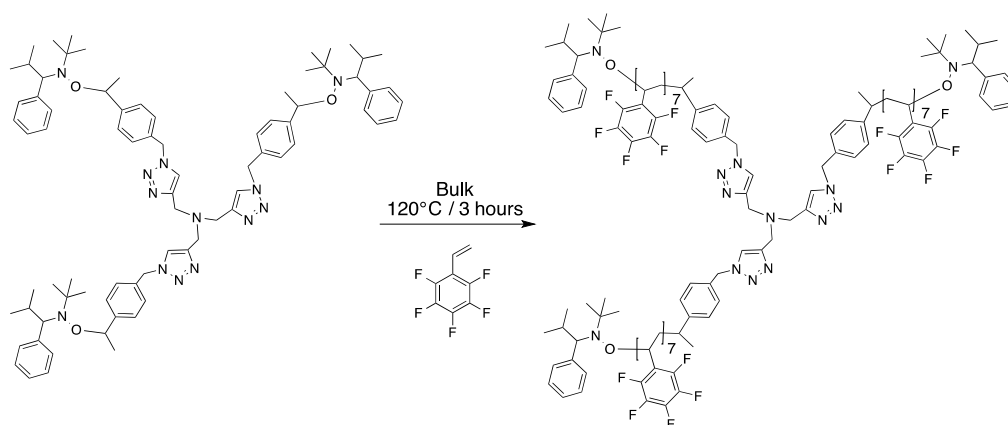
The TBTA-based NMP initiator (0.090 g, 0.070 mmol, 1 eq.) was introduced into a Schlenk tube and dissolved in 2,3,4,5,6-pentafluorostyrene (1.068 mL, 8.440 mmol, 120

eq.). The solution underwent 5 freeze-pump thaw cycles to remove oxygen, then the flask was filled with argon and immersed in an oil bath heated at 120°C for 3 hours. The Schlenk tube was then removed from the oil bath and the polymer was precipitated twice from dichloromethane in cold methanol, collected and dried under vacuum for 24 hours. M_n: 3843 g/mol; M_w: 4260 g/mol (Calibration of linear PS) PDI: 1.10 ^{1}H NMR: (400 MHz, CDCl$_3$) δ (ppm) 7.73 (m, 3 H, CH); 6.70 - 7.50 (m, 27 H, CH); 5.45 (d, 6 H, CH); 3.74 (m, 6 H, CH); 3.27 (m, 3 H, CH$_{NO}$); 1.75-3.00 (m, 96 H, CH); 0.19 – 1.50 (s, 54 H, CH) ^{13}C NMR: (101 MHz, CDCl$_3$) δ (ppm) 146.49, 142.14, 144.04, 139.06, 136.49, 128.3, 114.51, 72.35, 59.44, 32.08, 31.76, 28.46, 28.31, 24.75, 23.18, 22.20, 22.0, 21.20, 21.13 ^{19}F NMR: (377 MHz, CDCl$_3$) δ (ppm) -142.96, -154.00, -161.09.

Poly(2,3,4,5,6-pentafluorostyrene) three-arm star polymer (PFS$_{10}$)$_3$
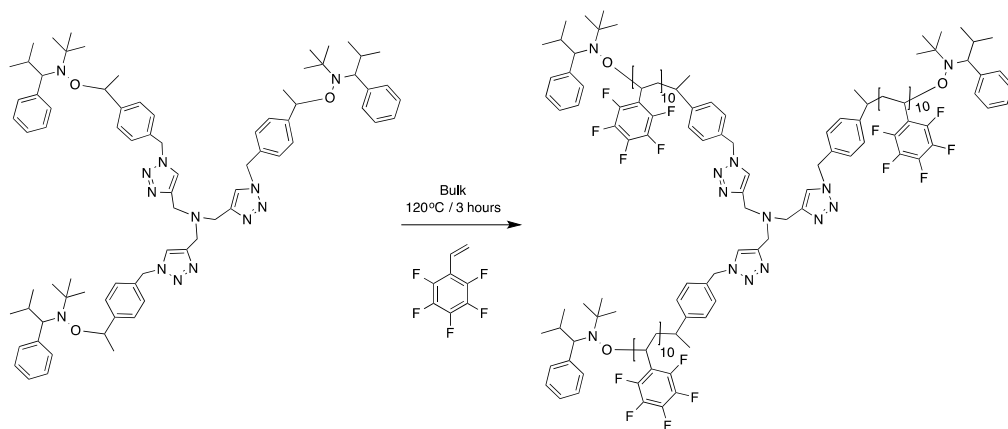
The TBTA-based NMP initiator (0.150 g, 0.117 mmol, 1 eq.) was introduced into a Schlenk tube and dissolved in 2,3,4,5,6-pentafluorostyrene (1.948 mL, 0.014 mol, 120 eq.). The solution underwent 5 freeze-pump thaw cycles to remove oxygen, then the flask was then filled with argon and immersed in an oil bath heated at 120°C for 3 hours. The

polymer was precipitated twice from dichloromethane into cold methanol, then collected and dried for 24 hours under vacuum. M_n: 5550 g/mol; M_w: 6380 g/mol (Calibration of linear PS) PDI: 1.16 ^{1}H NMR: (400 MHz, CDCl$_3$) δ (ppm) 8.30 (m, 3 H, CH); 6.70 - 7.50 (m, 27 H, CH); 5.45 (d, 6 H, CH); 3.74 (m, 6 H, CH); 3.27 (m, 3 H, CH$_{NO}$); 1.75-3.00 (m, 66 H, CH); 0.19 – 1.50 (s, 54 H, CH) ^{13}C NMR: (101 MHz, CDCl$_3$) δ (ppm) 146.49, 142.14, 144.04, 139.06, 136.49, 128.3, 114.51, 72.35, 59.44, 32.08, 31.76, 28.46, 28.31, 24.75, 23.18, 22.20, 22.0, 21.20, 21.13 ^{19}F NMR: (377 MHz, CDCl$_3$) δ (ppm) -142.86, -154.00, -161.12.

Poly(2,3,4,5,6-pentafluorostyrene) three-arm star polymer (PFS$_{16}$)$_3$
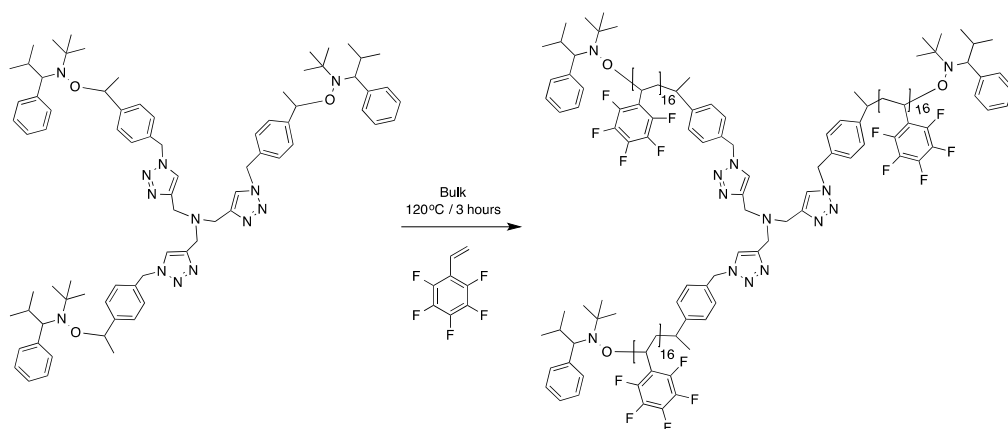
The TBTA-based NMP initiator (0.090 g, 0.07 mmol, 1 eq.) was introduced into a Schlenk tube and dissolved in 2,3,4,5,6-pentafluorostyrene (2.435 mL, 0.017 mol, 250 eq.). The solution underwent 5 freeze-pump thaw cycles to remove oxygen. The flask was then filled with argon and immersed in an oil bath heated at 120°C for 3 hours. The polymer was precipitated twice from dichloromethane into cold methanol, then collected and dried for 24 hours under vacuum. M_n: 7950 g/mol; M_w: 9650 g/mol (Calibration of linear PS) PDI: 1.20 ^{1}H NMR: (400 MHz, CDCl$_3$) δ (ppm) 8.30 (m, 3 H, CH); 6.70 - 7.50

(m, 27 H, CH); 5.45 (d, 6 H, CH); 3.74 (m, 6 H, CH); 3.27 (m, 3 H, CH_{NO}); 1.75-3.00 (m, 152 H, CH); 0.19 – 1.50 (s, 68 H, CH) ^{13}C NMR: (101 MHz, CDCl$_3$) 146.00, 143.85, 140.78, 139.36, 138.06, 136.78, 130.55, 127.70, 127.33, 126.20, 114.22, 77.02, 61.45, 53.98, 46.02, 38.63, 37.17, 32.06, 27.90, 21.16 ^{19}F NMR: (377 MHz, CDCl$_3$) δ (ppm) -142.96, -154.00, -161.09.

4-polyethylene glycol methylstyrene (Mw: 500 g/mol) OEGSt
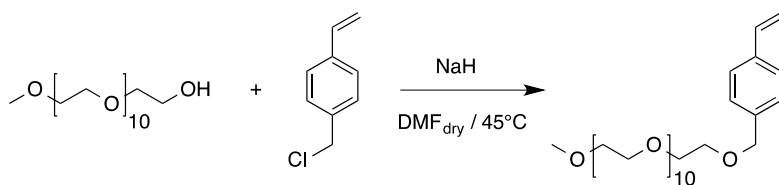
Polyethylene glycol mono-methoxy (11.97 g, 23 mmol, 1.2 eq.) was dried by azeotropic distillation in toluene and introduced into a 500 mL three-necks-flask containing 20 mL of dried DMF. The solution was then heated at 45°C under argon. NaH (6.28 g, 157 mmol, 8 eq.) was added, and the mixture was allowed to stir. After 2 hours, 4 chloro-methyl styrene (2.770 mL, 19 mmol, 1 eq.) purified by passing through an Al_2O_3 column was added dropwise to the reaction mixture. The reaction was run for 24 hours under argon. After the reaction, 20 mL of methanol was added, and the mixture was then extracted in dichloromethane. The organic phases were combined, dried in the presence of MgSO$_4$, filtered and then concentrated using a rotary evaporator. The resulting red-yellowish oil was dried under high vacuum to give 11.5 g (Yield: 79%) of the product. ^{1}H NMR: (400 MHz, CDCl$_3$) δ (ppm) 7.38-7.32 (m, 4 H), 6.71 (m, 1 H, H), 5.77 (d, J=17.3 Hz, 1H); 5.22 (d, J= 8Hz, 1H); 4.56 (s, 2H); 3.45-3.85 (s, 58H) 3.39 (s, 3.6H). ^{13}C NMR:

(101 MHz, CDCl$_3$) δ (ppm) 137.32, 136.15, 128.84, 125.67, 113.24, 72.48, 71.52; 70.09; 69.02, 61.20, 58.55.

Poly(2,3,4,5,6-pentafluorostyrene)-b-poly(oligo ethylene glycol styrene) three-arm star block copolymer (PFS$_7$-b-OEGSt$_3$)$_3$
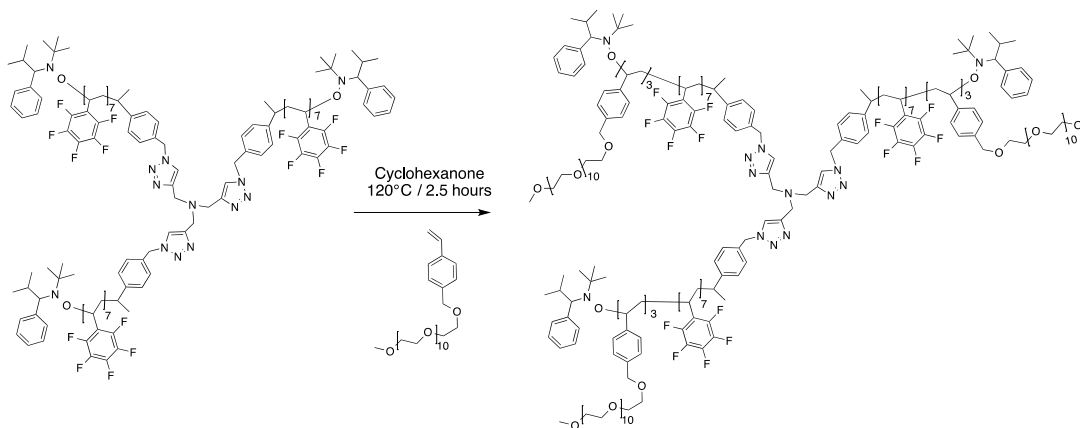
The macro-initiator poly(2,3,4,5,6-pentafluorostyrene) was introduced into a Schlenk tube (0.060 g, 0.013 mmoles, 1 eq.) and dissolved in 3.6 mL of cyclohexanone. 4-polyethylene glycol methyl styrene (0.481 g, 0.780 mmol, 60 eq.) was subsequently added, and the solution underwent 5 freeze-pump-thaws cycles to remove oxygen. The Schlenk tube was filled with argon and introduced into an oil bath heated at 120°C. After 2.5 hours, the Schlenk tube was then transferred to an ice water bath to cool down the reaction mixture, and then the mixture was concentrated using a rotary evaporator. THF was added to the resulting viscous residue, and the solution was dialyzed for two days against water using 1K cut-off dialysis membrane to remove excess of monomer. The dialysis bag was transferred into a beaker with THF for two hours, and the solution was dried to give a yellowish solid residue. M$_n$: 5900 g/mol; M$_w$: 6600 g/mol (Calibration of linear PS) PDI: 1.12; ^{1}H NMR: (400 MHz, CDCl$_3$) δ (ppm) 6.70 - 7.50 (m, 62 H, CH);

5.45 (d, 6 H, CH); 4.54 (s, 16 H); 3.5 -3.75 (s, 375 H, CH_2) 3.37 (s, 23 H, CH_3) 1.5-3.00 (m, 96 H, CH); ^{13}C NMR: (101 MHz, $CDCl_3$) δ (ppm) 146.49, 142.14, 144.04, 139.06, 136.49, 128.32, 114.51, 72.35, 71.02, 70.92, 59.44, 38.26, 32.50, 30.12, 23.11, ^{19}F NMR: (377 MHz, $CDCl_3$) δ (ppm) -142.96, -154.00, -161.09.

Poly(2,3,4,5,6-pentafluorostyrene)-b-poly(oligo ethylene glycol styrene) three-arm star block copolymer (PFS_{10}-b-OEGSt_4)_3
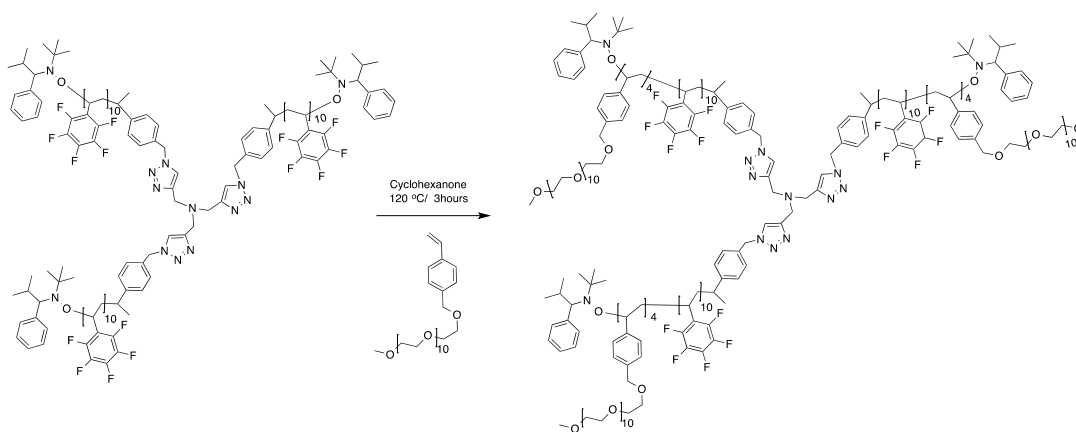
The macro-initiator poly(2,3,4,5,6-pentafluorostyrene) was introduced into a Schlenk tube (0.100 g, 0.014 mmoles, 1 eq.) and dissolved in 2 mL of cyclohexanone. 4-polyethylene glycol methyl styrene (0.594 g, 0.780 mmol, 70 eq.) was subsequently added, and the solution underwent 5 freeze-pump-thaws cycles to remove oxygen. The Schlenk tube was filled with argon and introduced into an oil bath heated at 120°C. After 3 hours, the Schlenk tube was transferred to an ice water bath to stop the polymerization. The solvent was removed on a rotary evaporator to give a viscous residue, which was then diluted in THF. The solution was dialyzed against water for two days using a 1K cut-off dialysis membrane to remove excess of monomer. The dialysis bag was then dialyzed against THF for 2 hours, and the solution was dried to give a yellowish solid

residue. M_n: 11200 g/mol; M_w: 13216 g/mol (Calibration of linear PS) PDI: 1.18; ^{1}H NMR: (400 MHz, CDCl$_3$) δ (ppm) 6.70 - 7.50 (m, 74 H, CH); 5.45 (d, 6 H, CH); 4.54 (s, 20 H); 3.5 -3.75 (s, 554 H, CH$_2$); 3.37 (s, 37 H, CH$_3$); 1.5-3.00 (m, 214 H, CH); 0.5-1.24 (m, 59 H, CH) ^{13}C NMR: (101 MHz, CDCl$_3$) δ (ppm) 146.49, 142.14, 144.04, 139.06, 136.49, 128.32, 114.51, 72.35, 71.02, 70.92, 59.44, 38.26, 32.50, 30.12, 23.11, ^{19}F NMR: (377 MHz, CDCl$_3$) δ (ppm) -142.86, -154.00, -161.12.

Poly(2,3,4,5,6-pentafluorostyrene)-b-poly(oligo ethylene glycol styrene) three-arm star block copolymer (PFS$_{16}$-b-OEGSt$_4$)$_3$
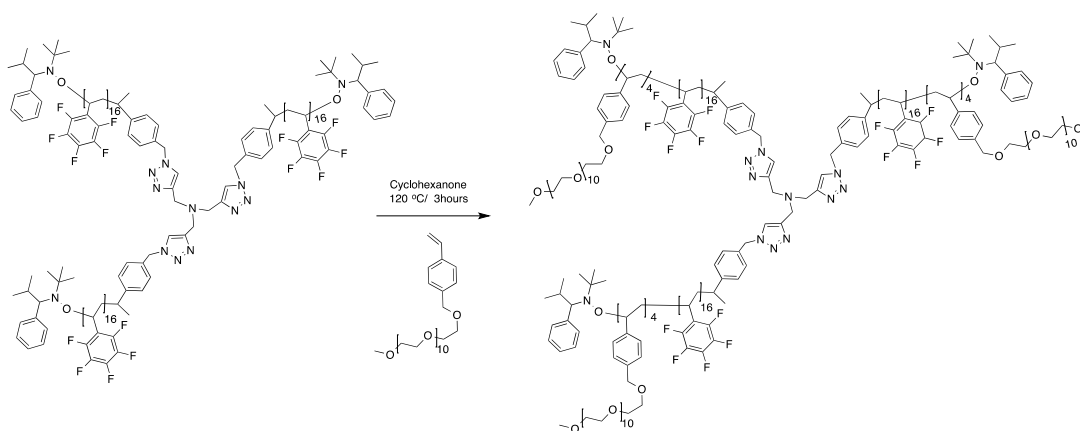
The macro-initiator poly(2,3,4,5,6-pentafluorostyrene) was introduced into a Schlenk tube (0.100 g, 0.009 mmoles, 1 eq.) and dissolved in 3 mL of cyclohexanone. 4-polyethylene glycol methyl styrene (0.572 g, 0.928 mmol, 100 eq.) was subsequently added, and the solution underwent 5 freeze-pump-thaws cycles to remove oxygen. The Schlenk tube was filled with argon and introduced into an oil bath heated at 120°C. After 3 hours, the Schlenk tube was transferred to an ice water bath to stop the polymerization. The solvent was removed using a rotary evaporator to give a viscous residue which was then diluted in THF. The solution was dialyzed against water for two days using 1K cut

off dialysis membrane to remove excess of monomer. The dialysis bag was then dialyzed against THF for 2 hours, and the solution was dried to give a yellowish solid residue. M_n: 12400 g/mol; M_w: 15130 g/mol (Calibration of linear PS) PDI: 1.22; ^{1}H NMR: (400 MHz, CDCl$_3$) δ (ppm) 8.34 (m, 3H, CH); 6.70 - 7.50 (m, 84 H, CH); 5.45 (d, 6 H, CH); 4.54 (s, 20 H); 3.5 -3.75 (s, 508 H, CH$_2$); 3.37 (s, 40 H, CH$_3$); 1.5-3.00 (m, 182 H, CH); 0.5-1.24 (m, 80 H, CH) ^{13}C NMR: (101 MHz, CDCl$_3$) δ (ppm) 146.49, 142.14, 144.04, 139.06, 136.49, 128.32, 114.51, 72.35, 71.02, 70.92, 59.44, 38.26, 32.50, 30.12, 23.11, ^{19}F NMR: (377 MHz, CDCl$_3$) δ (ppm) -142.86, -154.00, -161.12.

Poly(2,2,3,3,4,4,4-heptafluorobutyl acrylate) three-arm star polymer (PFBA$_7$)$_3$
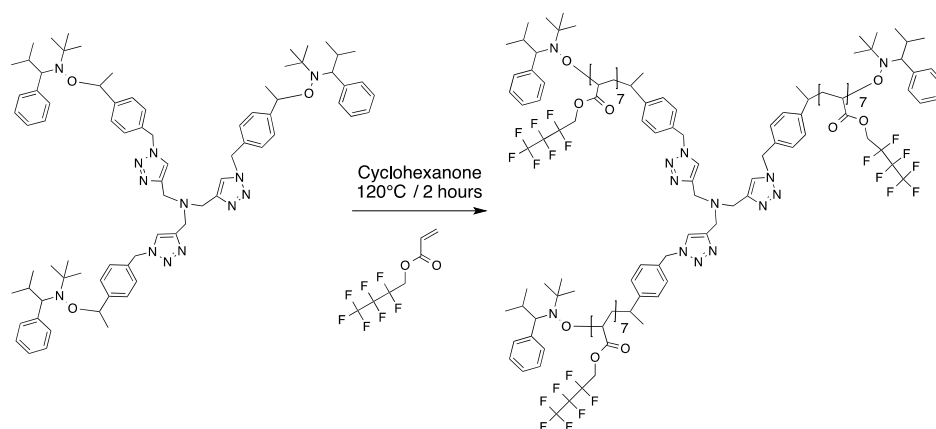
The 2,2,3,3,4,4,4-heptafluorobutyl acrylate monomer (0.700 mL, 3.910 mmol, 100 eq.) was purified through a basic Al$_2$O$_3$ column to remove the inhibitor before use. The monomer was then transferred into a Schlenk tube containing NMP initiator (0.050 g, 0.039 mmoles, 1 eq.). 0.7 mL of cyclohexanone was then added to the mixture. The solution underwent 5 freeze-pump-thaw cycles to remove oxygen, the Shlenk tube was then filled with argon, and placed in an oil bath heated at 120°C. After two hours, the polymerization was stopped by placing the Schlenk tube in an ice water bath.

Cyclohexane was removed on a rotary evaporator, and the polymer was precipitated in hexane, filtered and then dried under vacuum. M_n: 4154 g/mol; M_w: 4710 g/mol (Calibration of linear PS) PDI: 1.13. ^{1}H NMR: (400 MHz, CDCl$_3$) δ (ppm) 7.73 (m, 3 H, CH); 6.70 - 7.50 (m, 27 H, CH); 5.46 (d, 6 H, CH); 4.55 (s, 46 H, CH$_2$) 3.81 (m, 6 H); 3.27 (m, 3 H, CH); 1.50-3.00 (m, 66H, CH); 0.19 – 1.50 (s, 44H, CH) ^{13}C NMR: (101 MHz, CDCl$_3$) δ (ppm) 172.75, 141.29; 132.97, 131.18, 130.57, 128.43; 127.78; 126.72, 121.18-105.85, 82.58, 72.25, 61.56, 59.64, 41.15, 34.47, 28.46, 21.46. ^{19}F NMR: (377 MHz, CDCl$_3$) δ (ppm) -81.45, -121.29, -128.28.

Poly(2,2,3,3,4,4,4-heptafluorobutyl acrylate) three-arm star polymer (PFBA$_{14}$)$_3$
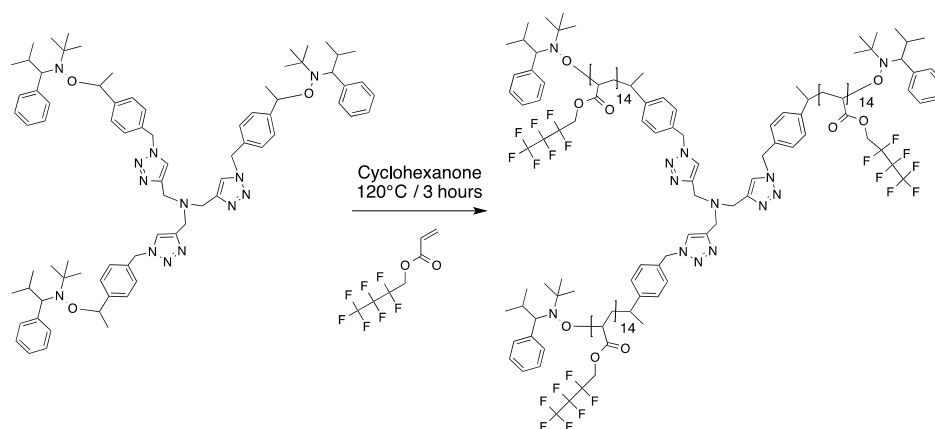
The 2,2,3,3,4,4,4-heptafluorobutyl acrylate monomer (0.700 mL, 3.91 mmol, 100 eq.) was purified through a basic Al$_2$O$_3$ column to remove the inhibitor before use. The monomer was then transferred into a Schlenk tube containing NMP initiator (0.050 g, 0.039 mmoles, 1 eq.). The mixture was dissolved in 0.7 mL of cyclohexanone and then the solution underwent 5 freeze-pump-thaw cycles to remove oxygen. The Schlenk tube was then filled with argon, and then placed in an oil bath heated at 120°C to polymerize. After 3 hours, the solution was concentrated on a rotary evaporator to remove the solvent,

and the polymer was precipitated into hexane, filtered off and then the precipitate was dried under vacuum. M_n: 7782 g/mol; M_w: 9100 g/mol (Calibration of linear PS) PDI: 1.17. ^{1}H NMR: (400 MHz, CDCl3) δ (ppm) 7.73 (m, 3 H, CH); 6.70 - 7.50 (m, 27 H, CH); 5.46 (d, 6 H, CH); 4.55 (s, 78 H, CH2) 3.81 (m, 3 H); 3.27 (m, 3 H, CH); 1.50-3.00 (m, 174H, CH); 0.19 – 1.50 (s, 48H, CH) ^{13}C NMR: (101 MHz, CDCl3) δ (ppm) 172.75, 141.29; 132.97, 131.18, 130.57, 128.43; 127.78; 126.72, 121.18-105.85, 82.58, 72.25, 61.56, 59.64, 41.15, 34.47, 28.46, 21.46. ^{19}F NMR: (377 MHz, CDCl$_3$) δ (ppm) -81.45, -121.29, -128.28.

Poly(2,2,3,3,4,4,4-heptafluorobutyl acrylate) three-arm star polymer (PFBA$_{20}$)$_3$
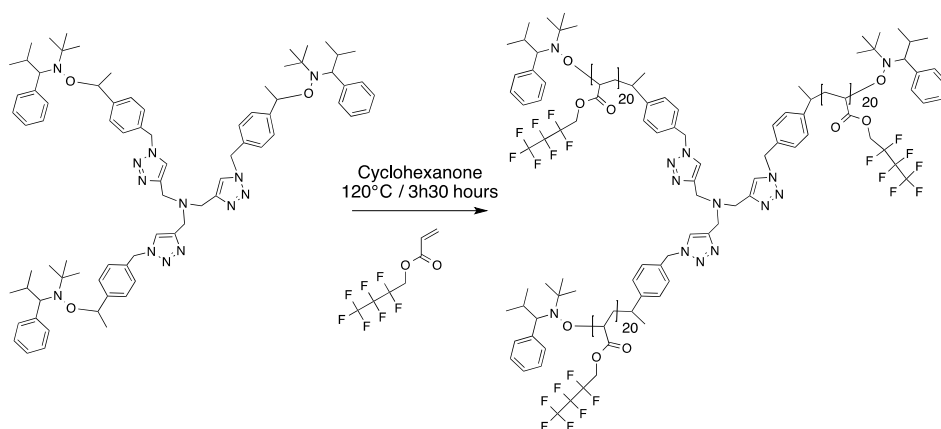
The 2,2,3,3,4,4,4-heptafluorobutyl acrylate (0.700 mL, 3.91 mmol, 200 eq.) was purified through a basic Al$_2$O$_3$ column to remove the inhibitor before use. The monomer was then transferred to a Schlenk tube containing NMP initiator (0.025 g, 0.020 mmoles, 1 eq.). The mixture was dissolved in 0.7 mL of cyclohexanone and the solution underwent 5 freeze-pump-thaw cycles to remove oxygen. The Shlenk tube was then filled with argon, and placed in an oil bath heated at 120°C for 3.5 hours. After polymerization, the solvent was removed on a rotary evaporator and the polymer was precipitated into

hexane, the solvent was filtered off and then the precipitate was dried under vacuum. M_n: 9206 g/mol; M_w: 10126 g/mol (Calibration of linear PS) PDI: 1.11. ^{1}H NMR: (400 MHz, CDCl$_3$) δ (ppm) 7.73 (m, 3 H, CH); 6.70 - 7.50 (m, 27 H, CH); 5.46 (d, 6 H, CH); 4.55 (s, 120 H, CH$_2$) 3.81 (m, 6 H); 3.27 (m, 3 H, CH); 1.50-3.00 (m, 188H, CH); 0.19 – 1.50 (s, 54H, CH) ^{13}C NMR: (101 MHz, CDCl$_3$) δ (ppm) 172.75, 141.29; 132.97, 131.18, 130.57, 128.43; 127.78; 126.72, 121.18-105.85, 82.58, 72.25, 61.56, 59.64, 41.15, 34.47, 28.46, 21.46. ^{19}F NMR: (377 MHz, CDCl$_3$) δ (ppm) -81.45, -121.29, -128.28.

Poly(2,2,3,3,4,4,4-heptafluorobutyl acrylate)-b-poly(oligo ethylene glycol styrene) three-arm star block copolymer (PFBA$_{20}$-b-OEGSt$_4$)$_3$
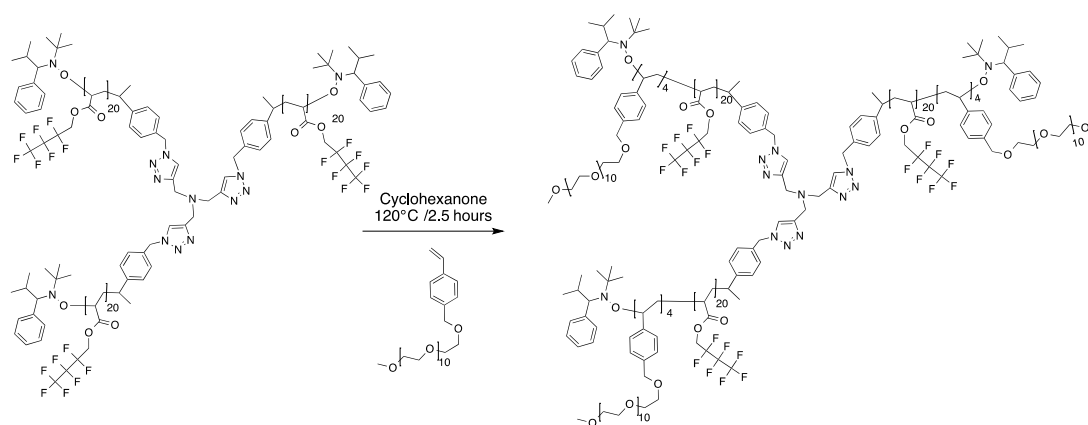
Poly(2,2,3,3,4,4,4-heptafluorobutyl acrylate) macro-initiator (0.100 g, 0.006 mmol, 1 eq.) and 4-polyethylene glycol methylstyrene monomer (0.518 g, 0.840 mmol, 140 eq.) were introduced into a Schlenk tube containing 2 mL of cyclohexanone. The solution underwent 5 freeze-pump thaws cycles, the Schlenk tube was filled with Argon and then introduced into an oil bath heated at 120°C. After 2.5 hours, the Schlenk tube was transferred to an ice water bath to stop the polymerization and the viscous solution was dried using a rotary evaporator to remove cyclohexane. The resulting residues were

dissolved in THF and dialyzed against water for two days using a 1K cut-off dialysis membrane. The dialysis bag was transferred in THF for 2 hours, and the solution was dried to give a yellowish solid residue. M_n: 12800 g/mol; M_w: 16400 g/mol (Calibration of linear PS) PDI: 1.28 ^{1}H NMR: (400 MHz, CDCl$_3$) δ (ppm) 7.73 (m, 3 H, CH); 6.70 - 7.50 (m, 102 H, CH); 5.46 (d, 6 H, CH); 4.55 (s, 120 H, CH$_2$) 3.80-3.45 (m, 776 H, CH); 3.45-3.35 (s, 48 H, CH) 1.00-3.00 (m, 230 H, CH); ^{13}C NMR: (101 MHz, CDCl$_3$) δ (ppm) 172.75, 141.29, 132.97, 131.18; 130.57, 128.43, 127.78, 126.72, 121.18, 105.85, 82.58, 72.25, 72.36, 70.98, 61.56, 59.64, 59.46, 41.15, 34.47, 28.46, 21.46. ^{19}F NMR: (377 MHz, CDCl$_3$) δ (ppm) -81.45, -121.29, 128.28.

Poly(1H,1H,2H,2H-perfluorodecyl acrylate) three-arm star polymer (PFDA$_4$)$_3$
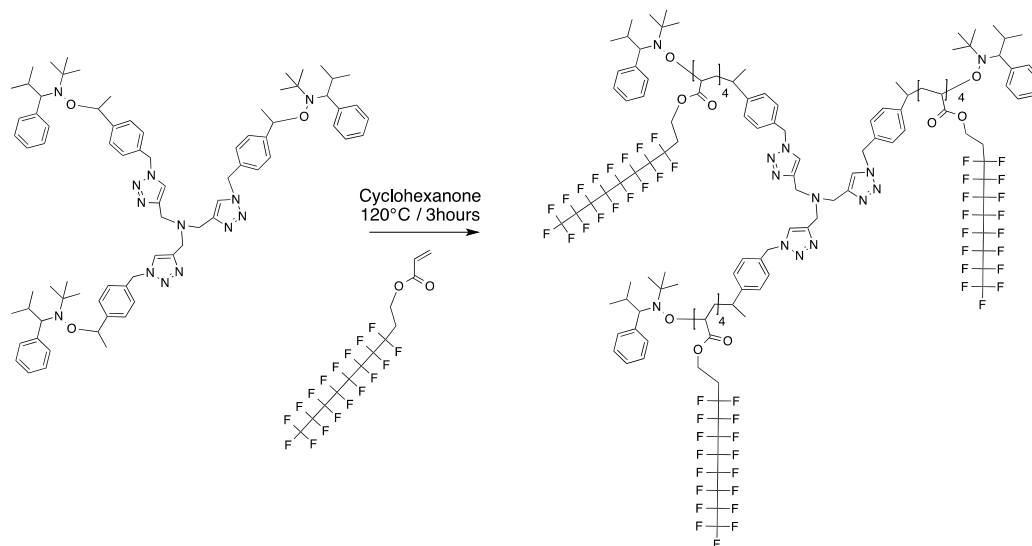
1H,1H,2H,2H perfluorodecyl acrylate monomer (1.230 mL, 3.910 mmol, 100 eq.) was first purified using a basic Al$_2$O$_3$ column, and transferred into a Schlenk tube containing NMP initiator (0.050 g, 0.039 mmol, 1 eq.) and 1.23 mL of cyclohexanone. The solution underwent 5 freeze-pump-thaw cycles. The Schlenk tube was filled with argon and

placed in an oil bath heated at 120°C. After 3 hours of polymerization, the viscous solution was concentrated on a rotary evaporator and the polymer was then precipitated in hexane, the solvent was filtered off and the precipitate was dried under vacuum. M_n: 7125 g/mol; M_w: 7650 g/mol (Calibration of linear PS) PDI: 1.08 ^{1}H NMR: (400 MHz, CDCl$_3$) δ (ppm) 7.96 (m, 1.5 H); 6.70 - 7.50 (m, 34 H, CH); 5.46 (d, 6 H, CH); 4.55 (s, 25 H, CH) 3.81 (m, 5 H, CH); 3.27 (m, 2.5 H, CH); 1.80-2.80 (m, 42 H, CH); 1.3-2.79 (m, 24 H, CH); 0.19 − 1.25 (s, 54 H, CH) ^{13}C NMR: (101 MHz, CDCl$_3$) δ (ppm) 174.77, 147.21, 144.40, 142.00, 133.25, 131.52, 128.43, 127.78, 126.72, 121.18-108.48, 83.12, 72.25, 61.70, 54.94, 41.72, 34.47, 30.78, 28.46, 21.46. ^{19}F NMR: (377 MHz, CDCl$_3$) δ (ppm) **-**80.95, **-**113.93, **-**122.21, **-**123.06, **-**123.79, **-**126.49.

Poly(1H,1H,2H,2H-perfluorodecyl acrylate)-b-poly(oligo ethylene glycol styrene) three-arm star block copolymer (PFDA₄-b-OEGSt₄)₃
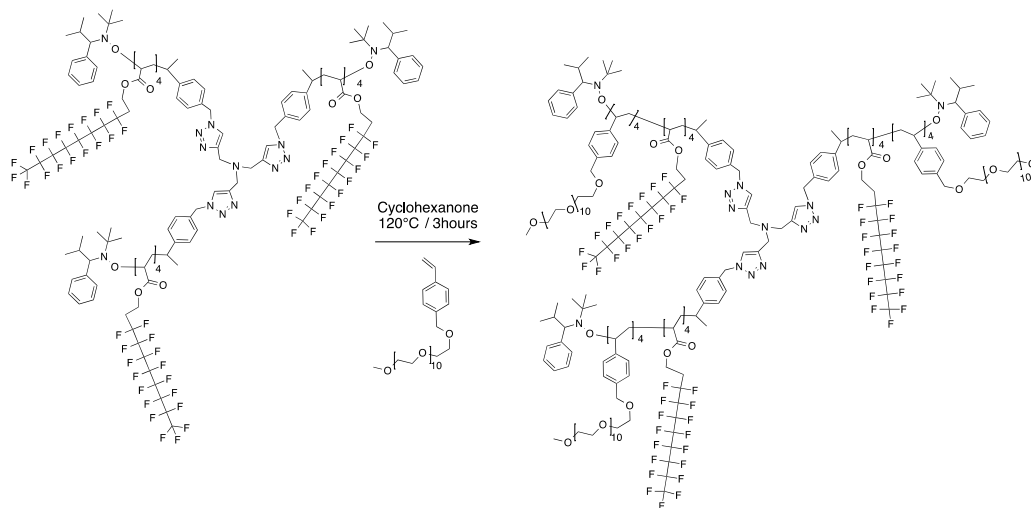
Poly(1*H*,1*H*,2*H*,2*H*-perfluorodecyl acrylate) macro-initiator (0.050 g, 0.06 mmol, 1 eq.) and 4-polyethylene glycol methyl styrene (0.45 g, 0.719 mmol, 110 eq.) were dissolved

in 2 mL of cyclohexanone in a Schlenk tube. The solution underwent 5 freeze-pump thaws cycles, the tube was then filled with argon and introduced in an oil bath heated at 120°C. After 2.5 hours, the Schlenk tube was transferred to an ice water bath to stop the polymerization. The viscous solution was dried on a rotary evaporator to remove cyclohexanone, diluted in THF and subsequently dialyzed against water over 2 days using 1K cut-off dialysis membranes. The dialysis bag was then transferred into a beaker filled with THF for 2 hours, and the solution was dried under vacuum to give a yellowish solid residue. M_n: 11500 g/mol; M_w: 14720 g/mol (Calibration of linear PS) PDI: 1.28 ^{1}H NMR: (400 MHz, CDCl$_3$) δ (ppm) 7.96 (m, 1.5 H, CH); 6.70 - 7.50 (m, 147 H, CH); 5.46 (d, 6 H, CH); 4.55 -4.00 (m, 60 H, CH) 3.50-3.75 (s, 549H, CH); 3.37 (s, 3H, CH); 0.50-2.50 (m, 180H + H$_2$O, CH); ^{13}C NMR: (101 MHz, CDCl$_3$) δ (ppm) 174.77, 147.21, 144.40, 142.00, 133.25, 131.52, 128.43, 127.78, 126.72, 121.18, 108.48, 83.12, 72.25, 71.02, 70.92, 61.70, 54.94, 59.44, 41.72, 34.47, 30.78, 28.46, 21.46 ^{19}F NMR: (377 MHz, CDCl$_3$) δ (ppm) -80.95, -113.93, -122.21, -123.06, -123.79, -126.49.

Poly(2,3,4,5,6-pentafluorostyrene)-b-poly(oligo ethylene glycol methacrylate) three-arm star block copolymers (PFSA$_{16}$-b-OEGSt$_{30}$)$_3$
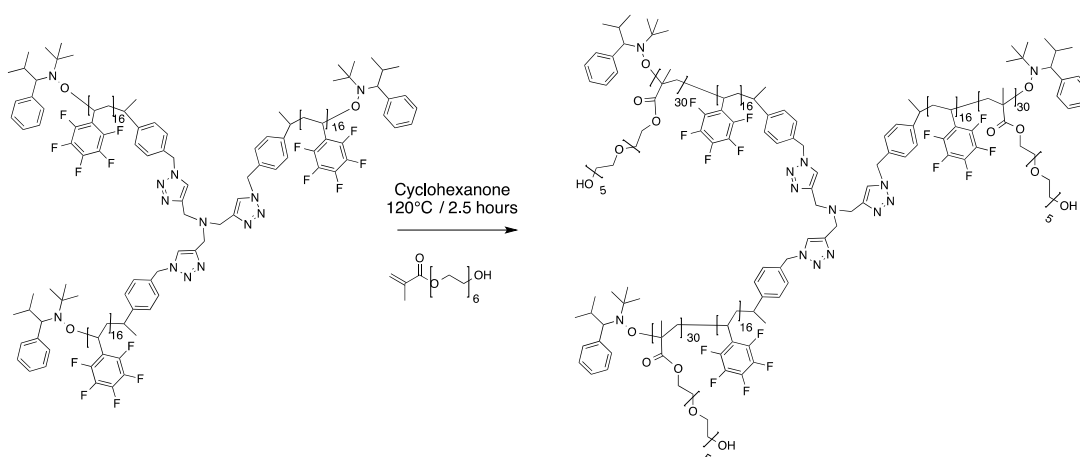
Poly(ethylene glycol) methacrylate was diluted in cyclohexanone (1:1) before purification through a basic Al_2O_3 column. The monomer (0.900 mL, 1.392 mmol, 300 eq.) was then introduced into a Schlenk tube containing poly(2,3,4,5,6-pentafluorostyrene) macroinitiator (0.050 g, 0.004 mmol, 1 eq.) and 0.5 mL of cyclohexanone. The colorless viscous solution underwent 5 freeze-pump thaws cycles and then the Schlenk tube was filled with argon and transferred to an oil bath heated at 120°C. After 2.5 hours of polymerization, the resulting viscous solution was concentrated using a rotary evaporator and further diluted in THF. The solution was dialyzed against water for 2 days using 8K cut-off dialysis membranes to remove any excess of monomer. Afterward, the dialysis bag was transferred to a beaker filled with THF for 2 hours to remove water, and the resulting solution was dried to yield a white solid residue. M_n: 13500 g/mol; M_w: 16470 g/mol (Calibration of linear PS) PDI: 1.22 ^{1}H NMR: (400 MHz, $CDCl_3$) δ (ppm) 7.63 (m, 3 H, CH); 6.70 - 7.50 (m, 25 H, CH); 6.20 and 5.54 (s, 7 H, CH) 5.41 (d, 6 H, CH_2); 4.75 (s, 6 H, CH_2); 4.01 (m, 185 H, CH_2); 3.4-3.8 (s, 2160 H, CH_2); 1.75-3.00 (m, 65 H, $CH_{aliphatic}$); 1.5-2.0 (s, 280 H, CH_3); 0.5 − 1.50 (m, 269 H, CH) ^{13}C NMR: (101 MHz, $CDCl_3$) δ (ppm) 146.49, 141.81, 144.04, 139.06, 136.49, 128.55, 114.68, 32.08, 28.57 ^{19}F NMR: (377 MHz, $CDCl_3$) δ (ppm) -142.86, -154.00, -161.12.

Poly(2,2,3,3,4,4,4-heptafluorobutyl acrylate)-b-poly(oligo ethylene glycol methacrylate) three-arm star block copolymer (PFBA$_7$-b-OEGMA$_{18}$)$_3$
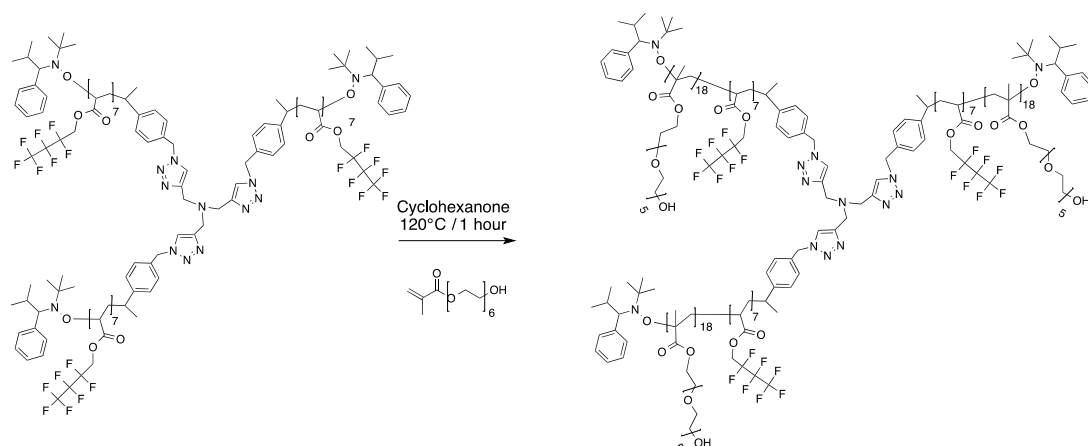
Poly(2,3,3,3,4,4,4 heptafluorobutyl acrylate) macro-initiator was introduced into a Schlenk tube (0.050 g, 0.0025 mmol, 1 eq.) and dissolved in 0.5 mL of cyclohexanone. Poly(ethylene glycol) methacrylate monomer was diluted in cyclohexanone to reach 1:1 volume ratio and further purified using a basic Al_2O_3 column. Poly(ethylene glycol) methacrylate (0.580 mL, 0.75 mmol, 300 eq.) was added to the Schlenk tube and the mixture underwent 5 freeze-pump-thaws cycles to remove oxygen. The Schlenk tube was then filled with argon and placed in an oil bath heated at 120°C. After 1 hour, the viscous solution was dried using a rotary evaporator to remove the solvent and the resulting solid residue was dissolved in THF. The solution was dialyzed against water for two days using 8K cut-off dialysis membranes to remove the excess of monomer. The dialysis bag was then transferred into a beaker filled with THF for 2 hours to remove water, and the solution was dried to yield a white solid residue. M_n: 11230 g/mol; M_w: 13360 g/mol (Calibration of linear PS) PDI: 1.19. ^{1}H NMR: (400 MHz, CDCl$_3$) δ (ppm) 7.63 (m, 3 H, CH); 6.70 - 7.50 (m, 25 H, CH); 6.20 and 5.54 (s, 7 H, CH) 5.41 (m, 6 H, CH); 4.75 (m, 6 H, CH); 4.56 (m, 50 H, CH$_2$); 4.09 (m, 108 H, CH$_2$); 3.4-3.8 (s, 1390 H, CH$_2$); 1.5-3.00 (m, 277 H, CH); 0.5 – 1.50 (m, 220 H, CH); ^{13}C NMR: (101 MHz, CDCl$_3$) δ (ppm)

126.21, 119.70, 73.14, 73.14, 64.35, 62.04, 45.19, 18.76.^{19}F NMR: (377 MHz, CDCl$_3$) δ (ppm) -81.45, -121.29, -128.28.

Poly(2,2,3,3,4,4,4-heptafluorobutyl acrylate)-b-poly(oligo ethylene glycol methacrylate) three-arm star block copolymer (PFBA$_{14}$-b-OEGMA$_{30}$)$_3$
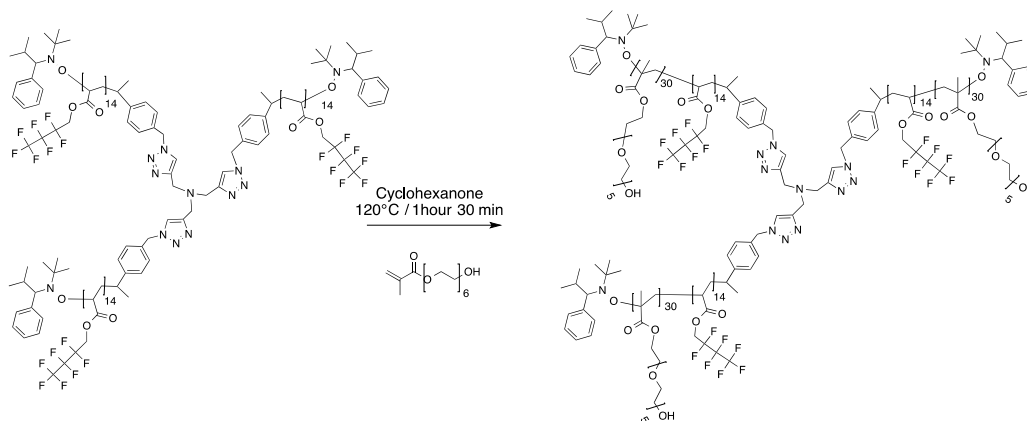
Poly(2,3,3,3,4,4,4 heptafluorobutyl acrylate) macro-initiator was introduced into a Schlenk tube (0.050 g, 0005 mmol, 1 eq.) and dissolved in 0.5 mL of cyclohexanone. Poly(ethylene glycol) methacrylate monomer was diluted in cyclohexanone to reach a 1:1 volume ratio and further purified using a basic Al$_2$O$_3$ column to remove the inhibitor. Poly(ethylene glycol) methacrylate (1.080 mL, 1.637 mmol, 300 eq.) was added to the Schlenk tube and the resulting homogenous solution underwent 5 freeze-pump-thaws cycles to remove oxygen. The Schlenk tube was filled with argon and introduced in an oil bath heated at 120°C. After 1 hour, the Schlenk tube was transferred to a cold water bath to stop the polymerization. The viscous solution was dried on a rotary evaporator to remove the solvent and the resulting solid residue was dissolved in THF. The solution was dialyzed against water for two days using 8K cut-off dialysis membranes to remove the excess of monomer. The dialysis bag was then transferred to a beaker filled with THF

for 2 hours and the solution was dried under vacuum to yield a white solid residue. M_n: 13200 g/mol; M_w: 15970 g/mol (Calibration of linear PS) PDI: 1.21. ^{1}H NMR: (400 MHz, CDCl$_3$) δ (ppm) 7.63 (m, 3 H, CH); 6.70 - 7.50 (m, 34 H, CH); 6.20 and 5.54 (s, 7 H, CH) 5.41 (m, 6 H, CH); 4.75 (m, 6 H, CH); 4.56 (m, 80 H, CH$_2$); 4.09 (m, 178 H, CH$_2$); 3.4-3.8 (s, 2541 H, CH$_2$); 1.5-3.00 (m, 250 H, CH); 0.5 – 1.50 (m, 370 H, CH); ^{13}C NMR: (101 MHz, CDCl$_3$) δ (ppm) 126.21, 119.70, 73.14, 73.14, 64.35, 62.04, 45.19, 18.76.^{19}F NMR: (377 MHz, CDCl$_3$) δ (ppm) -81.45, -121.29, -128.28.

Poly(1H,1H,2H,2H-Perfluorodecyl acrylate)-b-poly(oligo ethylene glycol methacrylate) three-arm star block copolymer (PFDA$_4$-b-OEGMA$_{30}$)$_3$
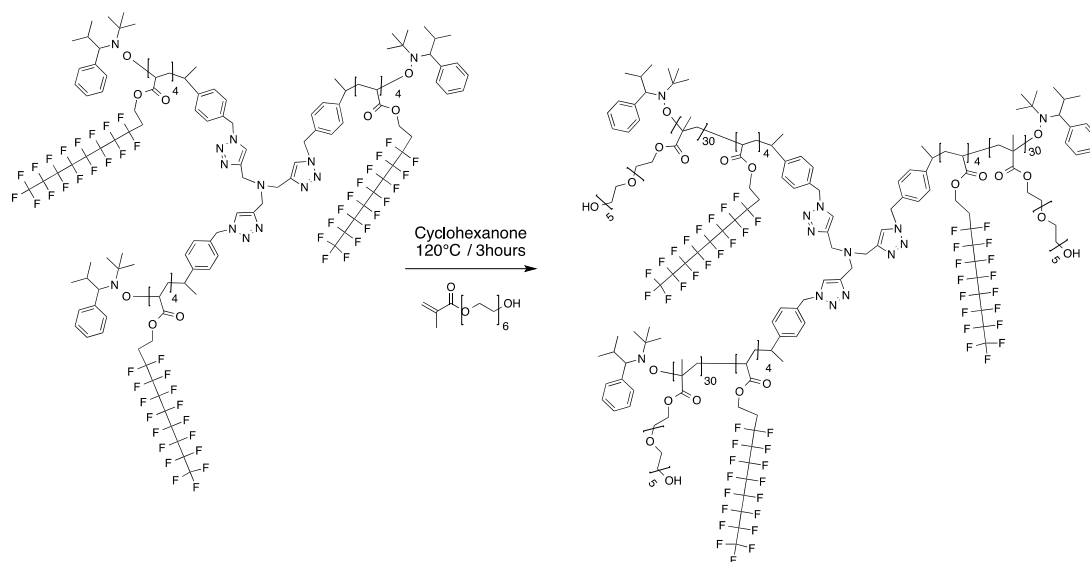
Poly(*1H,1H,2H,2H* perfluorodecyl acrylate) macro-initiator was introduced into a Schlenk tube (0.050 g, 0.006 mmol, 1 eq.) containing 0.5 mL of cyclohexanone. Poly(ethylene glycol) methacrylate monomer was diluted in cyclohexane to reach a 1:1 volume ratio, and further purified using a basic Al$_2$O$_3$ column to remove the inhibitor. Poly(ethylene glycol) methacrylate diluted in cyclohexane (1.280 mL, 1.961 mmol, 300

eq.) was added to the mixture, and the resulting homogenous solution underwent 5 freeze-pump thaws cycles. The Schlenk tube was then transferred to an oil bath heated at 120°C for 3 hours. The resulting viscous solution was concentrated on a rotary evaporator by removing the solvent. The resulting solid residue was then dissolved in THF and dialyzed against water for two days using 8K cut-off dialysis membranes. The dialysis bag was then transferred in THF for 2 hours to remove water, and the solution was dried under vacuum to yield a white solid residue. M_n: 11000 g/mol; M_w: 12320 g/mol (Calibration linear PS) PDI: 1.12 ^{1}H NMR: (400 MHz, CDCl$_3$) δ (ppm) 7.63 (m, 3 H, CH); 6.70 - 7.50 (m, 34 H, CH); 6.20 and 5.54 (s, 6 H, CH) 5.41 (m, 6 H, CH$_2$); 4.74 (m, 6 H, CH$_{2-}$); 4.00-4.56(m, 257 H, CH$_2$); 4.09 (m, 108 H, CH$_2$); 3.4-3.8 (s, 2354 H, CH$_2$); 1.5-3.00 (m, 245 H, CH); 0.5 – 1.50 (m, 346 H, CH) ^{13}C NMR: (101 MHz, CDCl$_3$) δ (ppm) 178.11; 167.69, 136.49, 129.38, 128.55, 126.09, 111.05, 108.18, 72.99, 68.30, 61.95, 53.92, 45.14, 29.55, 16.92 ^{19}F NMR: (377 MHz, CDCl$_3$) δ (ppm) **-80.95, -113.93, -122.21, -123.06, -123.79, -126.49.**

2.2.4.3 Dynamic Light Scattering

Micelles of (PFS$_7$-*b*-OEGSt$_3$)$_3$, (PFS$_{16}$-*b*-OEGSt$_4$)$_3$ and (PFDA$_4$-*b*-OEGSt$_4$)$_3$ star block copolymers were prepared by dissolving 3 mg of polymer in 1.5 mL of DMF, then 0.75 mL of water (deionized water) were added dropwise to induce micellization, and another volume (0.75 mL) of water was added in one shot. The DMF-water solution was then dialyzed overnight against water using an 8K cut-off membrane to give a micellar solution of 1 g/L concentration. The solution was then filtrated using 1 μm glass fiber membrane prior to analysis.

Vesicles from (PFBA$_{20}$-*b*-OEGSt$_4$)$_3$ star block copolymers were prepared by dissolving 10 mg of polymer in 1.5 mL of DMF, then 1.5 mL of deionized water was added using a syringe pump at 0.5 mL/ hour rate.

The DMF-water solution was then dialyzed overnight against water using an 8K cut-off membrane to give a 1 g/L concentration of the micellar solution. The solution was then filtrated using 1µm glass fiber membrane prior to analysis.

Micelles from (PFS$_{16}$-*b*-OEGMa$_{30}$)$_3$, (PFBA$_7$-*b*-OEGMa$_{18}$)$_3$ and (PFDA$_4$-*b*-OEGMa$_{30}$)$_3$ star block copolymer samples were prepared by vigorously stirring the star polymers in water for 5 days to reach 1 g/L concentration, then filtered over 1 µm glass fiber membrane prior to analysis.

2.2.4.4 Atomic Force Microscopy

Table 2.4 summarizes the sizes corresponding to the height and the diameters measured by AFM height and phase images for each of the star block copolymers. The phase images offer the advantage to precisely determine the diameter of the fluorinated core. The diameter of (PFS$_7$-*b*-OEGSt$_3$)$_3$, (PFS$_{10}$-*b*-OEGSt$_4$)$_3$ and (PFS$_{16}$-*b*-OEGSt$_4$)$_3$ star block copolymers obtained by AFM were found to be smaller than those obtained by DLS. In solution, micelles can easily interact through hydrogen bonding of the OEGSt corona chains leading to micellar aggregates. However, since micelles were spin-coated onto a silicon wafer prior AFM analysis, well-defined and isolated micelles were observed. Nevertheless, the measured height were found to be very small than diameter, meaning that the micelles are flattened due to low surface tension of the fluorinated core.

Two populations of different sizes were observed for the $(\text{PFBA}_{20}\text{-}b\text{-OEGSt}_4)_3$ and $(\text{PFDA}_4\text{-}b\text{-OEGMA}_{30})_3$ star block copolymers. $(\text{PFBA}_{20}\text{-}b\text{-OEGSt}_4)_3$, gave larger aggregates with the 30 nm height corresponding to multilayer vesicles, while aggregates of the 4 nm height were considered as bilayers vesicles, this was confirmed by cryo-TEM images. For the $(\text{PFDA}_4\text{-}b\text{-OEGMA}_{30})_3$ star block copolymer, the larger population was attributed to micellar aggregates.

Larger aggregates were observed for OEGMa containing star polymers. DLS analysis revealed a larger population with a hydrodynamic diameter ranging from 180 to 240 nm. By increasing the number of the OEGMA repeating units, larger micelles are formed. Larger aggregates might result from a larger overlap between corona chains through hydrogen bonding. AFM analysis revealed isolated micelles with a radius ranging from 35 to 44 nm. The height determined by AFM height image was found to be shorter (12-18 nm) due to the flattening of fluorinated micelles onto the silicon wafer. In this case of $(\text{PFDA}_4\text{-}b\text{-OEGM}_{30})_3$, 2 types of aggregates were observed for the same reason as the $(\text{PFDA}_4\text{-}b\text{-OEGSt}_4)_3$ star polymer.

Table 2.4 Height, diameter and core diameter of aggregates determined by AFM

Entry	Polymer	Diameter[a]	Height[b]	Core diameter[c]
1	$(\text{PFS}_7\text{-}b\text{-OEGSt}_3)_3$	76 ± 10	6 ± 2	54 ± 2
2	$(\text{PFS}_{10}\text{-}b\text{-OEGSt}_4)_3$	44 ± 6	8 ± 1	24 ± 2
3	$(\text{PFS}_{16}\text{-}b\text{-OEGSt}_4)_3$	46 ± 4	12 ± 1	24 ± 4
4[d]	$(\text{PFBA}_{20}\text{-}b\text{-OEGSt}_4)_3$	100 ± 14	30 ± 4	-
		120 ± 24	4 ± 1	
5	$(\text{PFDA}_4\text{-}b\text{-OEGSt}_4)_3$	74 ± 6	32 ± 3	54 ± 6
6	$(\text{PFS}_{16}\text{-}b\text{-OEGMA}_{30})_3$	70 ± 8	9 ± 2	46 ± 6
7	$(\text{PFBA}_7\text{-}b\text{-OEGMA}_{18})_3$	70 ± 8	13 ± 3	48 ± 2
8	$(\text{PFBA}_{14}\text{-}b\text{-OEGMA}_{30})_3$	88 ± 4	18 ± 2	-

9[e]	$(PFDA_4\text{-}b\text{-}OEGMA_{30})_3$	74 ± 10	12 ± 2	-
		50 ± 4	4 ± 1	

[a] Diameter of micelles determined from the height AFM images. [b] Height of micelles determined from the height AFM images. [c] Core of micelles determined from the phase AFM images. [d] Two populations of vesicles of different numbers of layers. [e] Two populations of micelles and micellar aggregates.

2.2.4.5 Transmission electron microscopy

Cryo-TEM images of $(PFS_7\text{-}b\text{-}OEGSt_3)_3$ and $(PFS_{10}\text{-}b\text{-}OEGSt_4)_3$ star block copolymer revealed spherical micelles of 20 ± 2 nm and 24 ± 4 nm diameter, respectively. TEM image of $(PFS_{16}\text{-}b\text{-}OEGSt_4)_3$ sample stained with OsO_4 vapors revealed micelles of 42 ± 4 nm corresponding to diameter of the micelle in agreement with AFM data collected. Cryo-TEM image of $(PFDA_4\text{-}b\text{-}OEGSt_4)_3$ revealed spherical micelles of 20 ± 2 nm of diameter. Interestingly, $(PFBA_{20}\text{-}b\text{-}OEGSt_4)_3$ sample revealed bilayer vesicles with a diameter ranging from 120 - 350 nm. The thickness of each layer was estimated to be 9 ± 1 nm. Multilayer vesicles of 350 nm of diameter were also observed. Addition of $CuSO_4$ led to vesicles containing Cu(II)-TBTA complex exhibiting higher contrast compared to the initial vesicles. Finally, (Cryo)-TEM images of micelles prepared from $(PFBA_7\text{-}b\text{-}OEGMa_{18})_3$, $(PFBA_{14}\text{-}b\text{-}OEGMa_{30})_3$, $(PFS_{16}\text{-}b\text{-}OEGMa_{30})_3$ and $(PFDA_4\text{-}b\text{-}OEGMa_{30})_3$ show spherical micelles with a diameter of 44 nm ± 8; 52 nm ± 6; 58 nm ± 10 and 24 nm ± 4 nm, respectively.

2.2.4.6 Catalysis
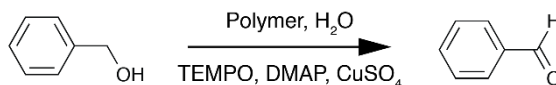
Entries 1 and 3 through 8: 4-Dimethylaminopyridine (6 mg, 0.05 mmol), the polymer (2 mg), 0.8 mL of a TEMPO stock solution (2 mM), and 4 mL of deionized water were

introduced in a 20 mL vial. The solution was then sonicated using a Branson digital sonifier (65% power, 4 min, 5 sec pulse on, 5 sec pulse off). During sonication the vial was placed in an ice bath. After sonication, benzyl alcohol (100 µL, 1 mmol) and 0.2 mL of $CuSO_4$ (0.4 mM) in H_2O were added. The reaction mixture was stirred at room temperature under atmospheric conditions (a balloon of air was used in this case). The conversion and selectivity were monitored by GC-MS and ^{1}H NMR (**Table 2.5**).

Entries 2 and 9 through 12: A $(PFBA_{14}\text{-}b\text{-}OEGMA_{30})_3$ micellar solution of 28 g/L concentration was prepared by dissolving the star polymer (170 mg, 2 µmol) in 3 mL of DMF, then 3 mL of water were added dropewise. The solution was then dialyzed against water overnight using 8K cutoff dialysis membranes. 4-dimethylaminopyridine (6 mg, 0.05 mmol), 0.5 mL of star block copolymer micellar solution and 0.2 mL of TEMPO (2.77 mM) were introduced in 3 mL and stirred at RT under air (balloon). Benzyl alcohol (10 µL, 0.1 mmol) and 0.2 mL of $CuSO_4$ (2.22 mM) in H_2O were added. The reaction mixture was stirred at room temperature under air (a balloon full of air was used in this case). The conversion and selectivity were monitored by ^{1}H NMR (**Figure 2.6**). After the reaction, 0.05 mL of reaction mixture was added to 0.6 mL of $CDCl_3$. The organic phase was transferred in NMR tube for ^{1}H NMR analysis.

Table 2.5 Catalytic results for an oxidation of alcohol into aldehyde using star block copolymers micelles.

Entry	Block Copolymer	Time [h]	TEMPO [mol %]	DMAP [mol %]	$CuSO_4$ [mol %]	Polymer cc *wt* %	Conv. [%]
1	Blank	36	1	5	0.2	-	<1
2	Blank	44	2.5	50	2	-	5
3	$(PFS_{10}\text{-}b\text{-}OEGSt_4)_3$	36	1	5	0.2	0.033	6

4	(PFBA$_{20}$-b-OEGSt$_4$)$_3$	36	1	5	0.2	0.033	28
5	(PFS$_{16}$-b-OEMa$_{30}$)$_3$	36	1	5	0.2	0.033	5
6	(PFBA$_7$-b-OEGMa$_{18}$)$_3$	36	1	5	0.2	0.033	25
7	(PFDA$_4$-b-OEGMa$_{30}$)$_3$	36	1	5	0.2	0.033	6
8	(PFBA$_{14}$-b-OEGMa$_{30}$)$_3$	36	1	5	0.2	0.033	22
9	(PFBA$_{14}$-b-OEGMA$_{30}$)$_3$	37	2.5	25	4	3.11	46
10	(PFBA$_{14}$-b-OEGMA$_{30}$)$_3$	31	2.5	25	2	1.555	53
11	(PFBA$_{14}$-b-OEGMA$_{30}$)$_3$	21	5	25	2	1.272	61
12	(PFBA$_{14}$-b-OEGMA$_{30}$)$_3$	44	2.5	50	2	1.555	90
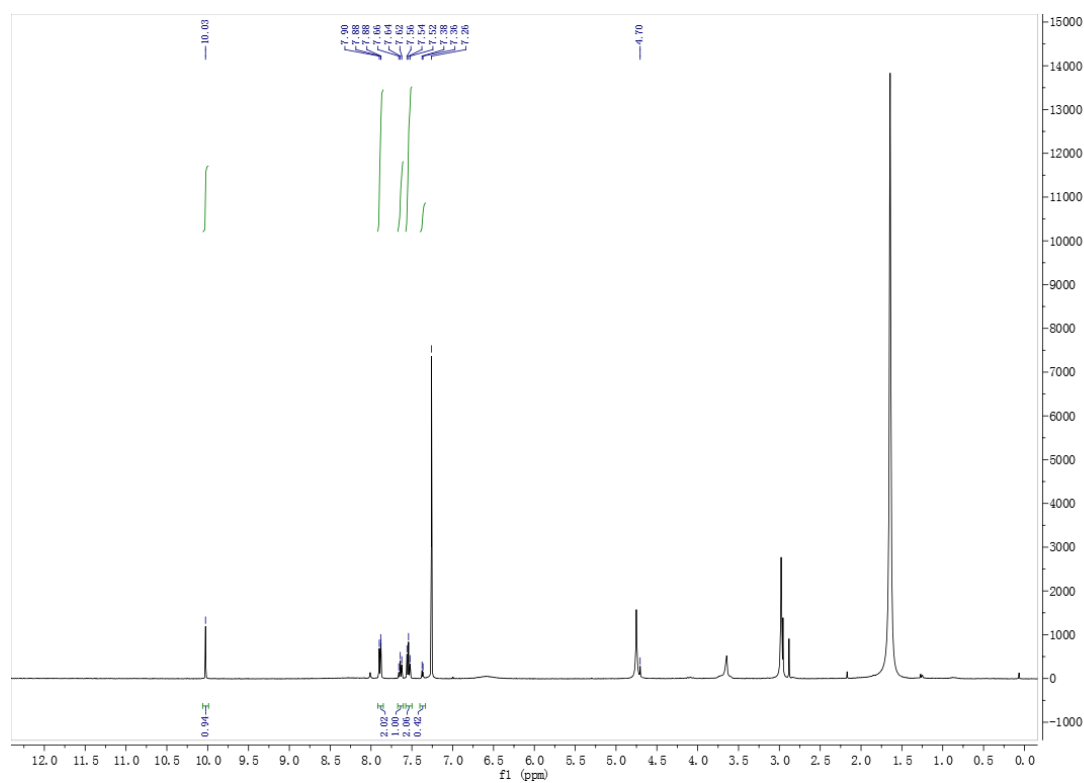
Figure 2.6 ^{1}H NMR spectrum of the product at 90% conversion after 44 hours. (**Table 2.5**, entry 12)

2.2.5 Conclusions

In conclusion, we prepared a library of well-defined star block-copolymers from a trifunctional nitroxide initiator based on the TBTA motif. In water, the copolymers self-assemble into micelles or vesicles, depending on the specific polymer composition. Copolymers containing PFBA monomer show evidence of molecular oxygen pre-concentration in the fluorinated cores of their micellar aggregates. In combination with DMAP and TEMPO "cofactors" and in the presence of $CuSO_4$, these copolymers act as competent catalysts for oxidation of alcohols to aldehydes in water.

2.3 Nanoreactors Self-assembled from Functional Surfactant[46]

In **Section 2.2**, a catalytic system based on oxygen pre-concentrating block-copolymer micelles has been described.[29] To improve upon the state of the art, here we describe another enzyme-inspired catalytic system based on a rationally designed tri-functional surfactant. The resulting micelles feature metal-binding sites, stable free radical moieties, as well as fluorous pockets which attract and pre-concentrate molecular oxygen. In the presence of Cu ions, the micelles effect chemoselective aerobic alcohol oxidation under ambient conditions in water.
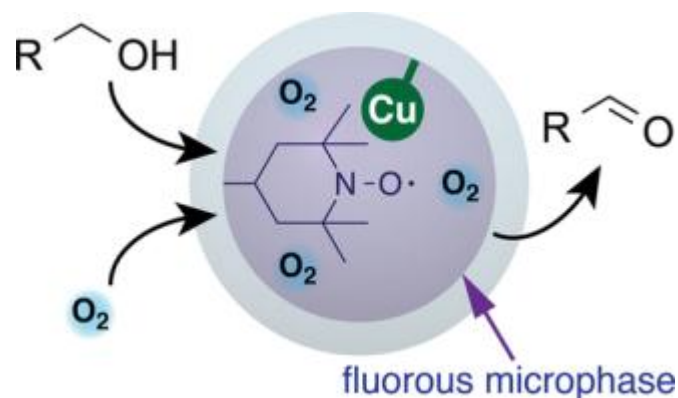
Figure 2.7 The proposed design for self-assembled fluorous nanoreactors.

2.3.1 Design and Synthesis of Multi-Functional Surfactant

We have aimed to design a functional surfactant architecture which covalently incorporating both TEMPO moieties and Cu-binding sites, and envisioned that a more efficient catalyst could result if a high local concentration of O_2 was created in the vicinity of the metal and free radical sites. Since perfluorocarbons and their aqueous dispersions are capable of dissolving significant amounts of molecular oxygen,[35, 36] we chose a fluorous hydrophobic "tail" as another desirable structural feature. As an added benefit, an "everything-phobic" perfluorocarbon moiety is expected to prevent the accumulation of the starting materials/products within the micelles, thus improving the accessibility of the active sites and preventing undesirable over-oxidation. Previously, the fluorous tagging strategy[47] has been used in Cu/TEMPO alcohol oxidations in organic solvents,[48] as well as in biphasic ClO⁻/TEMPO alcohol oxidations.[49] The structure of **1**, the surfactant we chose to explore, is shown in **Figure 2.8**. It was readily prepared in three steps, starting with commercially available amino-TEMPO (**Scheme 2.4**). We also

synthesized compounds **5·K** and **6**, each featuring only two of **1**'s three functional groups

(**Figure 2.8**).
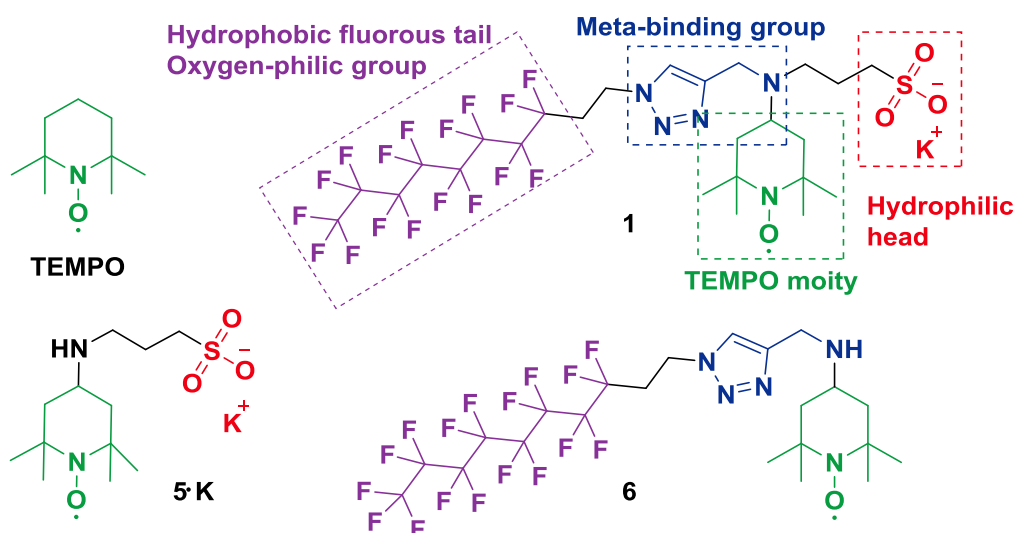
Figure 2.8 Functional surfactant incorporating a TEMPO moity, metal-binding group,

hydrophilic head and hydrophobic fluorous tail (oxygen-philic group).
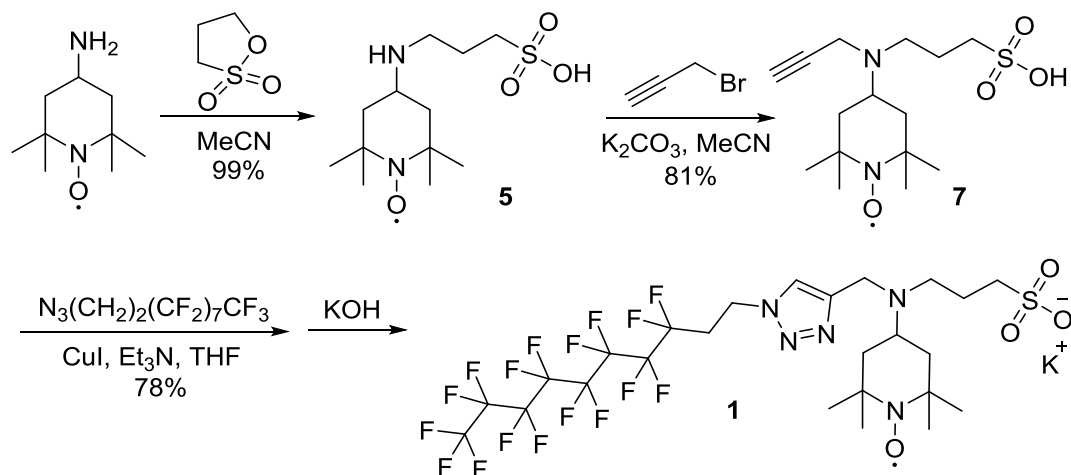
Scheme 2.4 The synthesis of functional surfactant **1**.
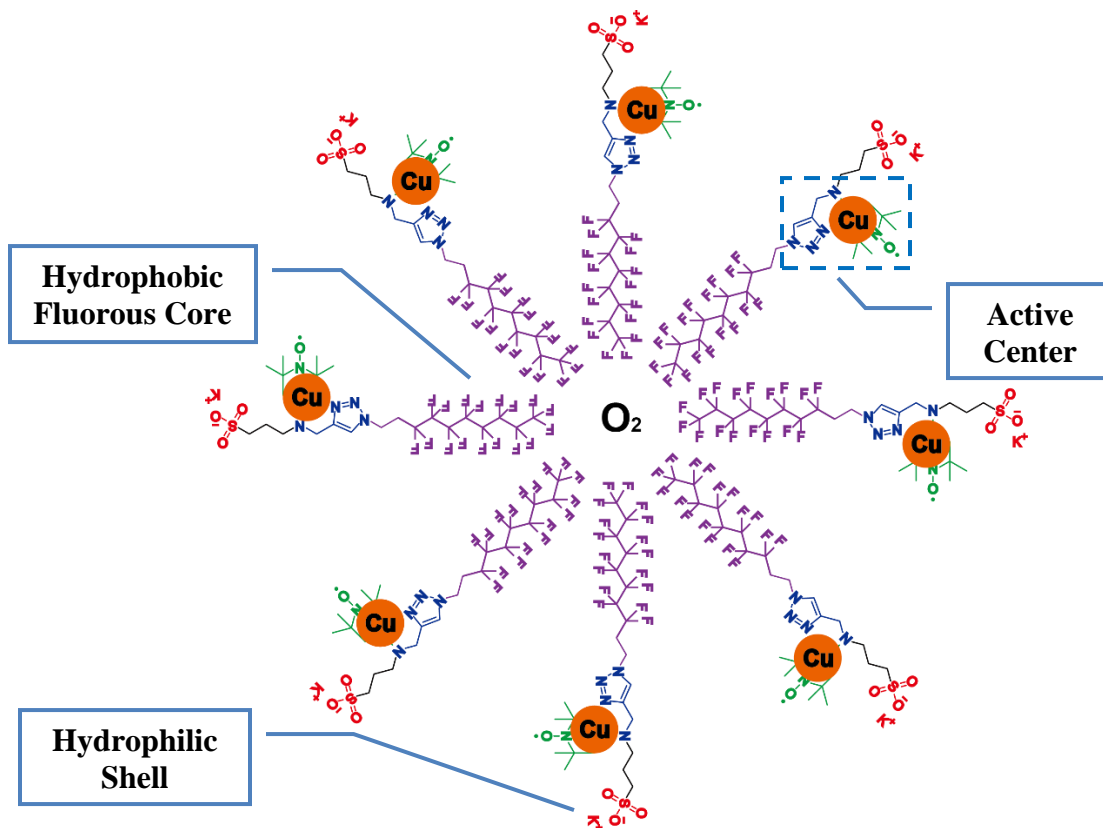
Figure 2.9 Enzyme like catalytic system self-assembled from functional surfactant **1** in water.

2.3.2 Evaluation of Catalytic Activity

To establish the baseline for Cu/TEMPO reactivity in aqueous and micellar media, we initiated our study by performing a range of model aerobic oxidation reactions in the presence of common surfactants. The conditions were selected to be similar to well-established organic solvent protocols.[23] Data for selected reactions is summarized in **Table 2.6** (see **Section 2.3.6.1** and **2.3.6.2** for the full set of experiments). The nature of the base and polydentate ligand added (if any) has a profound effect on the outcome of the reactions in organic solvents.[24, 50, 51] We found that the same holds true for water and

micellar media. The nature and amount of surfactant present had an equally significant impact on reactivity. Generally, we found the catalytic system is less well-behaved in water than in organic solvents.

Table 2.6 Aerobic oxidations of benzyl alcohol catalyzed by a variety of Cu/TEMPO/amphiphile systems.[a]
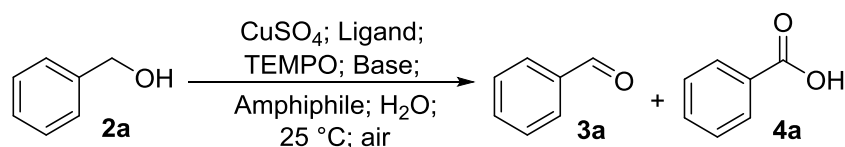
Entry	Surfactant, [mM]	TEMPO derivative, [mol %]	Base, [mol %][d]	Ligand[b,d]	$CuSO_4$, [mol %]	O_2 Source	3a, [%][c]	4a, [%][c]
1	-	TEMPO/5%	DMAP/20%	-	2	O_2	48±4	-
2	SDS/100	TEMPO/5%	DMAP/20%	-	2	O_2	83±4	10 ±3
3	SDS/100	TEMPO/5%	DMAP/10%	bpy	5	air	3 ±0.5	-
4	SDS/100	TEMPO/5%	DMAP/50%	bpy	5	air	100	-
5	SDS/20	TEMPO/5%	DMAP/50%	bpy	5	air	57 ±1.5	-
6	TX-100/100	TEMPO/5%	DMAP/50%	bpy	5	air	92 ±1	-
7	CTAB/100	TEMPO/5%	DMAP/50%	bpy	5	air	40 ±1	-
8	SDS/100	TEMPO/5%	NMI/50%	bpy	5	air	5.5 ±1	-
9	SDS/100	TEMPO/5%	DABCO/50%	bpy	5	air	5.5 ±1	-
10	SDS/100	TEMPO/5%	KOH/50%	bpy	5	air	31 ±7	12 ±3
11	SDS/100	TEMPO/5%	DIPEA/50%	bpy	5	air	35 ±2	9 ±1
12	SDS/100	TEMPO/5%	DBU/50%	bpy	5	air	62 ±4	19 ±1
13	-	5 K/5%	DMAP/20%	-	2	O_2	26 ±1	-
14	-	6/5%	DMAP/20%	-	2	O_2	39 ±4	-
15	1/5	1/5%	DMAP/20%	-	2	air	93	-
16	1/5	1/5%	DMAP/20%	-	2	O_2	98 ±2	-

a Reaction conditions: 0.5 mmol of BnOH in 5 ml of water, 25 °C, magnetic stirring, 1 hour. b Ligand:Cu ratio has been set to 1 for all ligands. c Determined by 1H NMR. Each result is an average from three independent experiments. d DMAP, 4-dimethylaminopyridine; NMI, N-methylimidazole; DABCO, 1,4-diazabicyclo[2.2.2]octane; DBU, 1,8-diazabicyclo[5.4.0]undec-7-ene; DIPEA, N,N-diisopropylethylamine; bpy, 2,2'-bipyridine.

While TEMPO is moderately soluble in water/benzyl alcohol mixtures, the aerobic oxidation of the alcohol is relatively slow in the absence of surfactants (**Table 2.6**, Entry 1, and **Figure 2.16**, SI), and does not proceed to completion. In the presence of sodium dodecyl sulfate (SDS), the rate improves markedly at the cost of a significant amount of overoxidation (**Table 2.6**, Entry 2). The overoxidation can be prevented by introducing 2,2'-bipyridine (bpy) (**Table 2.6**, Entry 4; see **Figure 2.15** for additional ligands). However, this necessitates the addition of 50 mol % of DMAP base (**Table 2.6**, Entries 3 and 4, and **Figure 2.12**). DMAP was found to be an optimal base/co-catalyst, with other bases we tried resulting in low conversion, poor selectivity, or both (**Table 2.6**, Entries 8-12, and **Figure 2.14**).

It is important to note that a high concentration of SDS (100 mM, 12 times higher than the critical micellization concentration, CMC) is necessary for the $CuSO_4$/TEMPO/bpy system to function effectively (**Table 2.6**, Entries 4 and 5, and **Table 2.8**, Entries 19-22, and **Figure 2.17**). Anionic SDS and the neutral Triton X-100 surfactants outperform the cationic cetyltrimethylammonium bromide (CTAB), even though the latter features a much lower CMC than SDS. This does suggest that surfactants may play a role in catalysis beyond simple solubilization of hydrophobic TEMPO or bpy/Cu.

Next, we examined the catalytic activity of compounds **5** and **6**. The hydrophobic, poorly-soluble **6** was less active than parent TEMPO (**Table 2.6**, Entry 14). The readily-soluble **5** K (potassium salt of **5**) was even less active: only 26% yield was realized after an hour, and the reaction did not proceed to completion. We attribute this loss of activity to the poor accessibility of the hydrophobic benzyl alcohol substrate by the highly

hydrophilic catalyst. While the reaction mixture appears homogeneous, its phase behavior is known to be complex, with up to three distinct phases coexisting.[52] With **5**·K and Cu^{2+} confined to different phases, we expect the reactivity will be impacted.
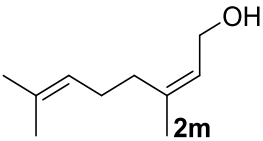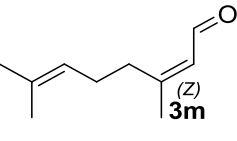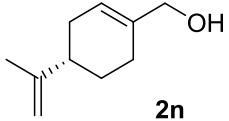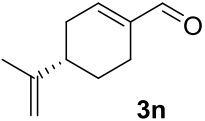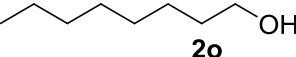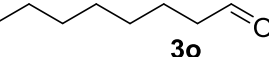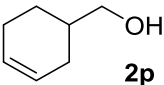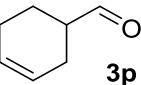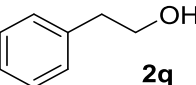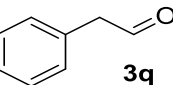
To our delight, we found that functional surfactant **1** was an efficient and selective catalyst for alcohol oxidations. The oxidation of benzyl alcohol proceeded to completion in the presence of 5 mol % of **1**, and significantly lower loadings of DMAP (20 mol %) and CuSO$_4$ (2 mol %) than were necessary for reactions in SDS micellar media (**Table 2.6**, Entry 16). No additional ligand was necessary to avoid over-oxidation. The oxidations proceeded well with both air and pure O$_2$ (**Table 2.6**, Entries 15, 16). Even lower amounts of CuSO$_4$, down to 0.2 mol %, could be used to effect the oxidation reactions, at the cost of slower reaction rates (**Table 2.9**). We found the parent TEMPO/CuSO$_4$ system in water loses its catalytic competency completely with low Cu loadings.

2.3.3 Catalytic Scope

Under the optimized conditions, **1** effectively catalyzes oxidations of a wide range of primary alcohols to their corresponding aldehydes (**Table 2.7**). The aldehyde products could be readily isolated in all cases by extracting the aqueous mixture with ethyl ether, followed by a filtration through a pad of silica gel. While the oxidations proceed nearly just as well with air, we performed the experiments using pure O$_2$ due to easier handling/better reproducibility achievable with our experimental setup.

Table 2.7 Scope of alcohol oxidations catalyzed by **1** in water.[a]

$$R \diagdown OH \xrightarrow[\text{H}_2\text{O; 25 °C; O}_2 \text{ balloon}]{\substack{\text{CuSO}_4\text{, 2 mol \%;} \\ \mathbf{1}\text{, 5 mol \%; DMAP, 20 mol \%;}}} R \diagdown O$$

2a-q → **3a-q**
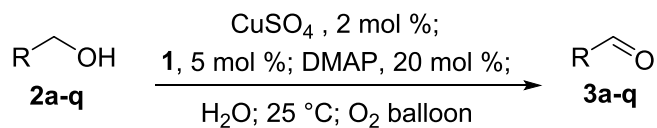
entry	Substrates	Products	Time/h	Yield/%[b]
1	2a	3a	1	94
2	2b	3b	1	98
3	2c	3c	1.5	99
4	2d	3d	2	99
5	2e	3e	24	51[c]
6	2f	3f	1	96
7	2g	3g	24	40[c]
8	2h	3h	24	78[c]
9	2i	3i	3	98
10	2j	3j	1	98
11	2k	3k	24	80[c]
12	2l	3l	20	92 (E : Z = 3 : 2)

13	**2m** (OH)	**3m** (Z) (O)	10	94 (E : Z = 10 : 9)[c]
14	**2n** (OH)	**3n** (O)	24	89
15	**2o** (OH)	**3o** (O)	24	2[c]
16	**2p** (OH)	**3p** (O)	24	0[c]
17	**2q** (OH)	**3q** (O)	24	0[c]

(a) Reaction conditions: 0.5 mmol of the alcohol, 5 mol % **1**, 2 mol % $CuSO_4$, 20 mol % DMAP, 5 ml of H_2O, 25 °C, in O_2 atmosphere. (b) Isolated yield; no carboxylic acid byproduct was detected in any of the reactions. (c) Determined by ^{1}H NMR.

Benzylic and heteroaromatic alcohols were somewhat more reactive (**Table 2.7**, Entries 1-9) than allylic substrates (**Table 2.7**, Entries 11-14). Most benzylic alcohols could be completely oxidized within 1–3 h, while 20-24 h was required for allylic substrates. The transformations of **2e**, **2g** and **2h** were more sluggish, possibly due to the competing coordination of the phenol, amine and furyl groups with copper (**Table 2.7**, Entries 5, 7, and 8). Consequently, only middling conversions were achieved in 24 h. It is worth mentioning that the sulfur-containing **2i** could be readily oxidized (**Table 2.7**, Entry 9). Cinnamyl alcohol was found to be extraordinarily reactive, with the reaction complete in less than an hour. For geraniol and nerol, isomerization was observed (**Table 2.7**, Entries 12 and 13).

Substrates lacking unsaturation a bond away from the OH group could not be oxidized (**Table 2.7**, Entries 15-17). While benzylic and allylic alcohols are known to be the more

active substrates in the established organic solvent protocols, they can be oxidized in acetonitrile. We attribute the difference in reactivity to a change in copper speciation between acetonitrile and water/micellar media.

2.3.4 Dissolved Oxygen Capacity
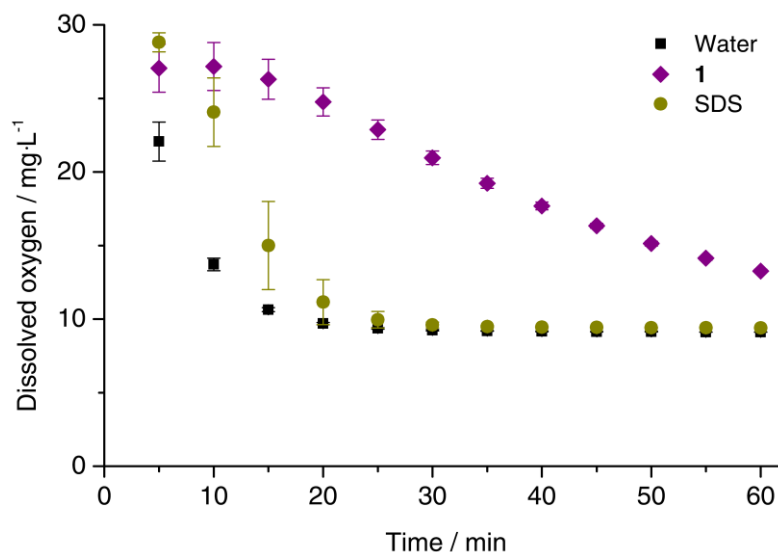
Figure 2.10 Kinetics of O_2 release from O_2-oversaturated solutions. Deionized water, black markers; 14 mM SDS, green markers; 5 mM **1**, purple markers.

To test our oxygen pre-concentration hypothesis, we examined the solubility of oxygen in the aqueous solutions of **1** and SDS, as well as the kinetics of O_2 release from oxygen-oversaturated solutions. Deionized water, as well as solutions of SDS and **1** were stirred vigorously in vials filled with pure O_2. The vials were opened to air, and the evolution of dissolved oxygen (DO) concentration was followed using an Inlab 605 immersion probe (Mettler Toledo) (**Figure 2.10**). We found that O_2-oversaturated solutions of SDS and **1** retain similar amounts of O_2 (~28 mg L^{-1}), measurably more than pure water. However,

for both pure water and SDS solution, the DO concentration dropped to its air-saturated value of ~9 mg L^{-1} within 20 minutes. As SDS solutions foam, the slightly slower O_2 release (and larger error of DO determination) can be attributed to gas retention within foam bubbles. In contrast, DO concentration in a dilute 5 mM solution of **1** is ~25 mg L^{-1} 20 minutes after venting the headspace oxygen. That oxygen must reside in the aggregates of **1** in the vicinity of TEMPO and Cu catalytic sites.

2.3.5 Further Insights
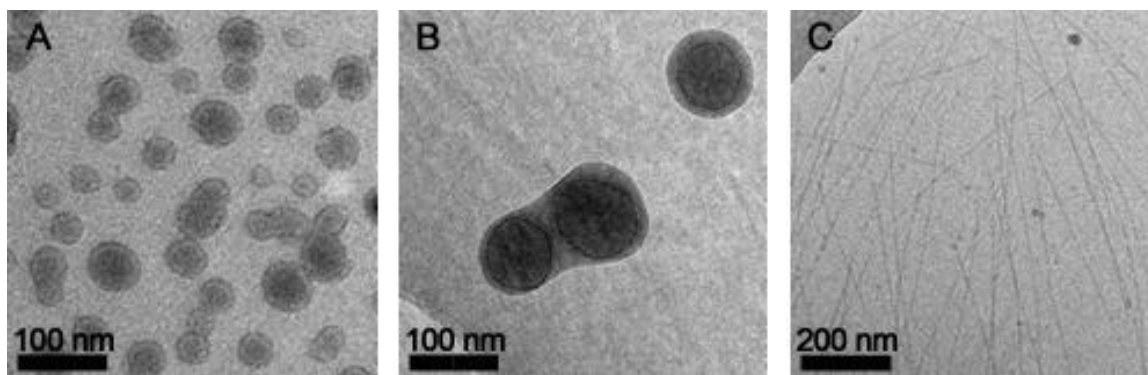
Figure 2.11 Cryo-TEM images of the aqueous solutions of **1**. (A) **1** spiked with KCN. (B) **1**, with added DMAP and $CuSO_4$. (C) **1**, with added DMAP, $CuSO_4$, and benzyl alcohol.

We gained further insight into the structure of our catalytic system using cryogenic transmission electron microscopy (cryo-TEM) images of the aggregates of **1** (**Figure 2.11**). In 5 mM aqueous solutions of **1** (spiked with KCN to scavenge any residual Cu ions), vesicular structures with an average diameter of 42.4 ± 9.1 nm were observed. After the addition of 20 mM DMAP and 2 mM $CuSO_4$, the vesicles changed to more complex, electron-dense aggregates ($d = 118.8 ± 33.2$ nm) . Interestingly, the reaction

mixture with BnOH (100 mM) exhibited a completely different morphology: high-aspect-ratio cylindrical micelles ($d = 8.2 \pm 0.5$ nm) were observed. Besides the impact of BnOH and the aldehyde product, this structural rearrangement might be ascribed to the change in the coordination preference of Cu, which is expected to exist mostly in its reduced Cu^{I} state upon addition of the alcohol. Furthermore, reduced TEMPO-H form of **1** could be detected in the reactions by LC-MS. This compound is more polar than **1** and likely has different self-assembly priorities.

2.3.6 Experimental Section

2.3.6.1 Alcohol Oxidation with Cu/TEMPO in the Presence of Common Amphiphiles

General Notes

Stock solutions were prepared as indicated: DMAP in MeCN (0.2 M); bpy in MeCN (0.025 M); TEMPO in H_2O (0.0125 M); KOH in H_2O (0.25 M); $CuSO_4$ in H_2O (0.025 M). The MeCN stock solutions were combined as necessary, and the organic solvent was removed in vacuum. Water was added, followed by sonication. Finally, aqueous stock solutions, benzyl alcohol, and $CuSO_4$ were added to start the reaction. The reactions were analyzed using NMR.

Table 2.8 The study of aerobic oxidation of BnOH with Cu/TEMPO in the presence of common amphiphiles.[a]
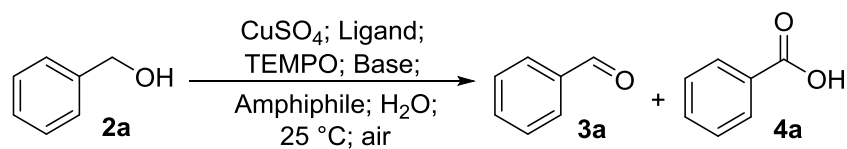
Entry	Ligand, [5 mol %]	Base, [mol %]	Amphiphile, [mM]	3a, [%][b]	4a, [%][b]
1	bpy	-	SDS, (100)	3.6 ±0.9	-
2	bpy	DMAP, (5)	SDS, (100)	3.0 ±0.4	-
3	bpy	DMAP, (10)	SDS, (100)	2.5 ±0.4	-
4	bpy	DMAP, (20)	SDS, (100)	1.5 ±0.7	-
5	bpy	DMAP, (30)	SDS, (100)	28.3 ±6.1	1.5 ±0.9
6	bpy	DMAP, (40)	SDS, (100)	83.7 ±3.1	7.6 ±3.2
7	bpy	DMAP, (50)	SDS, (100)	100 ±0	-
8	bpy	DMAP, (80)	SDS, (100)	53.7 ±4.1	-
9	bpy	DMAP, (100)	SDS, (100)	37.1 ±1.4	-
10	bpy	NMI, (50)	SDS, (100)	5.4 ±0.7	-
11	bpy	DABCO, (50)	SDS, (100)	5.4 ±1.1	-
12	bpy	KOH, (50)	SDS, (100)	30.7 ±6.9	11.8 ±3.0
13	bpy	KOH, (100)	SDS, (100)	78.2 ±3.8	21.8 ±3.8
14	bpy	DIPEA, (50)	SDS, (100)	35.3 ±2.3	9.3 ±0.8
15	bpy	DBU, (50)	SDS, (100)	61.8 ±3.7	19.2 ±1.3
16	bpy	DMAP, (50)	-	30.3 ±1.7	-
17	bpy	DMAP, (50)	Triton X-100, (100)	91.6 ±0.9	-
18	bpy	DMAP, (50)	CTAB, (100)	40.2 ±1.0	-
19	bpy	DMAP, (50)	SDS, (10)	48.6 ±6.0	-
20	bpy	DMAP, (50)	SDS, (20)	57.3 ±1.4	-
21	bpy	DMAP, (50)	SDS, (50)	92.2 ±0.9	-
22	bpy	DMAP, (50)	SDS, (200)	93.8 ±2.5	-
23	-	DMAP, (50)	SDS, (100)	69.9 ±3.5	-
24	(BimH)₃	DMAP, (50)	SDS, (100)	58.6 ±4.6	-
25	TBTA	DMAP, (50)	SDS, (100)	35.4 ±1.5	-

(a) Reaction conditions: 0.5 mmol of BnOH in 5 ml of water, 25 °C, magnetic stirring, 1 hour. (b) Determined by ^{1}H NMR. Each result is an average from three independent experiments.

Variation in the amount of DMAP

Stock solutions of bpy (0.025 mmol, 0.05 eq.) and DMAP (varying amounts: 0.025 mmol, 0.05 eq.; 0.05 mmol, 0.1 eq.; 0.1 mmol, 0.2 eq.; 0.15 mmol, 0.3 eq.; 0.2 mmol, 0.4 eq.; 0.25 mmol, 0.5 eq.; 0.4 mmol, 0.8 eq.; 0.5 mmol, 1 eq.) were added to 20 mL vials containing SDS (0.5 mmol, 1 eq.). The solvent was evaporated and the residue was dried under vacuum. 2 mL of the TEMPO stock solution (0.025 mmol, 0.05 eq.) and 2 mL of water were then added to each vial. The solutions were sonicated using a Branson digital sonifier (microtip, 65% power, 4 min, 5 sec pulse on, 5 sec pulse off) in an ice bath. After sonication, 1 mL of the $CuSO_4$ stock solution (0.025 mmol, 0.05 eq.) was added to each vial while stirring, followed by the addition of BnOH (0.5 mmol, 1 eq.). The mixtures were directly exposed to air and stirred at 25 ℃ for 1 h. The conversion and selectivity were monitored by ^{1}H NMR. Blank runs without the addition of DMAP were also performed. All reactions were performed 3 times in parallel.
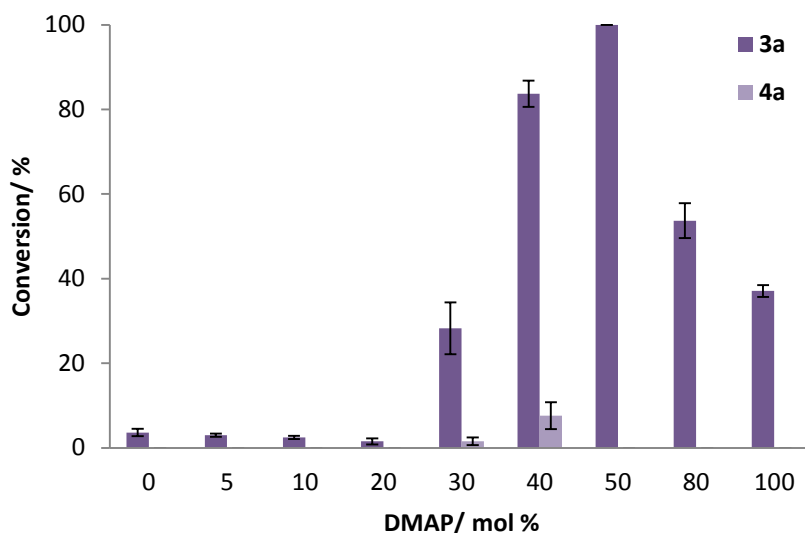
Figure 2.12 The effect of variations in the amount of DMAP. Conditions: 0.5 mmol of BnOH; 5 mol % CuSO$_4$; 5 mol % bpy; 5 mol % TEMPO; 0.1 M SDS; DMAP (0-100 mol %); 5 mL of H$_2$O; Air; 25 ℃; 1 h. Each reaction was run 3 times in parallel.

Variation in the amount of KOH

To 20 mL vials were added SDS (0.5 mmol, 1 eq.) and stock solution of bpy (0.025 mmol, 0.05 eq.). The solvent was evaporated and the residue was dried under vacuum. Different amounts of KOH (0.25 mmol, 0.5 eq.; 0.5 mmol, 1 eq.) and 2 mL of the TEMPO stock solution (0.025 mmol, 0.05 eq.) were added to each vial. The amount of water was then brought up to a total of 4 mL. The solutions were sonicated using a Branson digital sonifier (microtip, 65% power, 4 min, 5 sec pulse on, 5 sec pulse off) in an ice bath. After sonication, 1 mL of the CuSO$_4$ stock solution (0.025 mmol, 0.05 eq.) was added to each vial while stirring, followed by the addition of BnOH (0.5 mmol, 1 eq.). The mixtures were directly exposed to air and stirred at 25 ℃ for 1 h. The

conversion and selectivity were monitored by ^{1}H NMR. All reactions were performed 3 times in parallel.

Figure 2.13 The effect of variations in the amount of KOH. Conditions: 0.5 mmol of BnOH; 5 mol % CuSO$_4$; 5 mol % bpy; 5 mol % TEMPO; 0.1 M SDS (100 mol %); KOH (0-100 mol %); 5 mL of H$_2$O; Air; 25 ℃; 1 h. Each reaction was run 3 times in parallel.

Base screening

To 20 mL vials were added SDS (0.5 mmol, 1 eq.) and stock solution of bpy (0.025 mmol, 0.05 eq.). Then different bases (0.25 mmol, 0.5 eq.), i.e. NMI, DABCO, DIPEA or DBU were each added to the respective vials. The solvent was evaporated and the residue was dried under vacuum. 2 mL of the TEMPO stock solution (0.025 mmol, 0.05 eq.) and 2 mL of water were then added to each vial. The solutions were sonicated using a Branson digital sonifier (microtip, 65% power, 4 min, 5 sec pulse on, 5 sec pulse off) in an ice bath. After sonication, 1 mL of the CuSO$_4$ stock solution (0.025 mmol, 0.05 eq.)

was added to each vial while stirring, followed by the addition of BnOH (0.5 mmol, 1 eq.). The mixtures were directly exposed to air and stirred at 25 ℃ for 1 h. The conversion and selectivity were monitored by ^{1}H NMR. Blank runs without the addition of base were also performed. All reactions were performed 3 times in parallel.
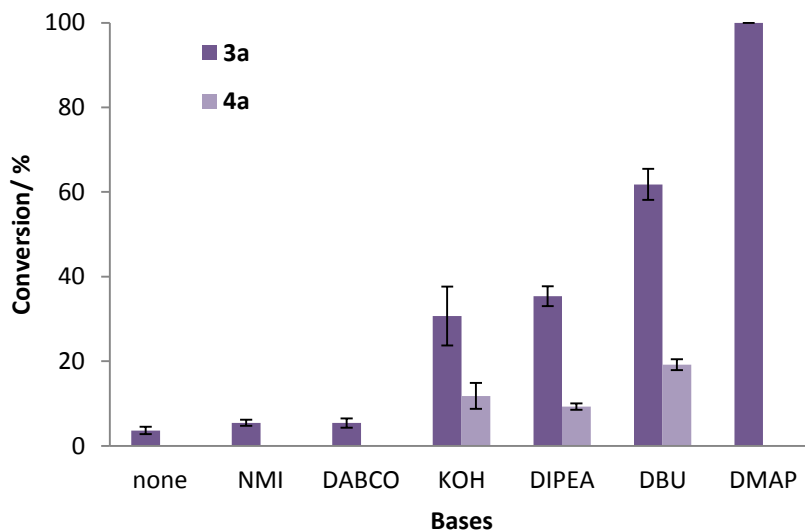
Figure 2.14 Screening the bases. Conditions: 0.5 mmol of BnOH; 5 mol % CuSO$_4$; 5 mol % bpy; 5 mol % TEMPO; 0.1 M SDS (100 mol %); 50 mol % bases; 5 mL of H$_2$O; Air; 25 ℃; 1 h. Each reaction was run 3 times in parallel.

Ligand screening

To 20 mL vials were added SDS (0.5 mmol, 1 eq.) and the DMAP stock solution (0.25 mmol, 0.5 eq.). Then different ligands (0.025 mmol, 0.05 eq.), i.e. TBTA and (BimH)$_3$ were each added to the respective vials. The solvent was evaporated and the residue was dried under vacuum. 2 mL of the TEMPO stock solution (0.025 mmol, 0.05 eq.) and 2 mL of water were then added to each vial. The solutions were sonicated using a Branson

digital sonifier (microtip, 65% power, 4 min, 5 sec pulse on, 5 sec pulse off) in an ice

bath. After sonication, 1 mL of the $CuSO_4$ stock solution (0.025 mmol, 0.05 eq.) was

added to each vial while stirring, followed by the addition of BnOH (0.5 mmol, 1 eq.).

The mixtures were directly exposed to air and stirred at 25 ℃ for 1 h. The conversion and

selectivity were monitored by ^{1}H NMR. Blank runs without the addition of ligand were

also performed. All reactions were performed 3 times in parallel.
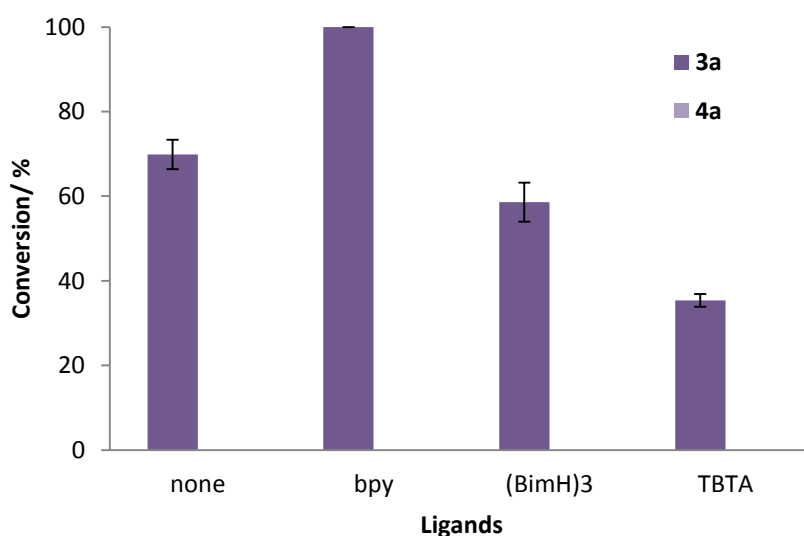
Figure 2.15 Screening the ligands. Conditions: 0.5 mmol of BnOH; 5 mol % $CuSO_4$; 5

mol % ligands; 5 mol % TEMPO; 0.1 M SDS (100 mol %); 50 mol % DMAP; 5 mL of

H_2O; Air; 25 ℃; 1 h. Each reaction was run 3 times in parallel. No acid byproduct was

observed.

Surfactant screening

The bpy (0.025 mmol, 0.05 eq.) and DMAP (0.25 mmol, 0.5 eq.) stock solutions were

added to 20 mL vials. Then different surfactants (0.5 mmol, 1 eq.), i.e. Triton X-100 or

CTAB were added respectively. The solvent was evaporated and the residue was dried under vacuum. 2 mL of the TEMPO stock solution (0.025 mmol, 0.05 eq.) and 2 mL of water were then added to each vial. The solutions were sonicated using a Branson digital sonifier (microtip, 65% power, 4 min, 5 sec pulse on, 5 sec pulse off) in an ice bath. After sonication, 1 mL of the $CuSO_4$ stock solution (0.025 mmol, 0.05 eq.) was added to each vial while stirring, followed by the addition of BnOH (0.5 mmol, 1 eq.). The mixtures were directly exposed to air and stirred at 25 ℃ for 1 h. The conversion and selectivity were monitored by ^{1}H NMR. Blank runs without the addition of surfactant were also performed. All reactions were performed 3 times in parallel.
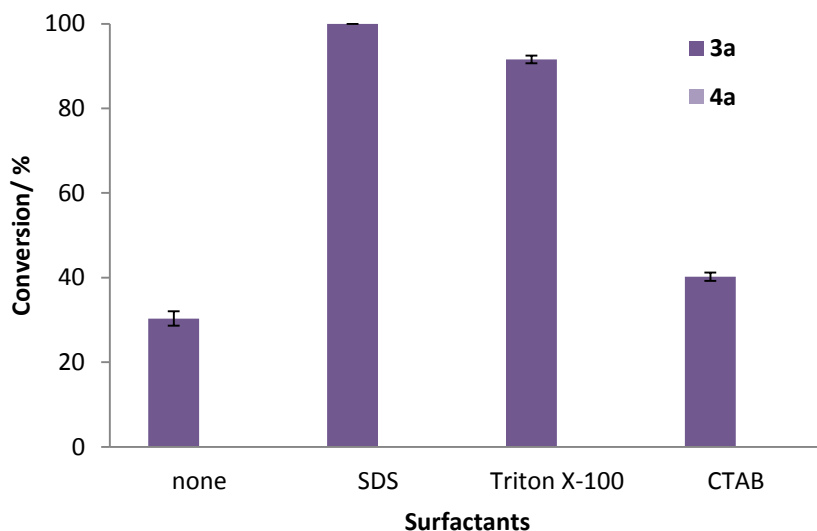
Figure 2.16 Screening the surfactants. Conditions: 0.5 mmol of BnOH; 5 mol % $CuSO_4$; 5 mol % bpy; 5 mol % TEMPO; 0.1 M of surfactants (100 mol %); 50 mol % DMAP; 5 mL of H_2O; Air; 25 ℃; 1 h. Each reaction was run 3 times in parallel. No acid byproduct was observed.

Variation in the amount of SDS

The bpy (0.025 mmol, 0.05 eq.) and DMAP (0.25 mmol, 0.5 eq.) stock solutions were added to 20 mL vials. Then different amount of SDS (0.05 mmol, 0.1 eq.; 0.1 mmol, 0.2 eq.; 0.25 mmol, 0.5 eq; 0.5 mmol, 1 eq.; 1 mmol, 2 eq.) was added respectively. The solvent was evaporated and the residue was dried under vacuum. 2 mL of the TEMPO stock solution (0.025 mmol, 0.05 eq.) and 2 mL of water were then added to each vial. The solutions were sonicated using a Branson digital sonifier (microtip, 65% power, 4 min, 5 sec pulse on, 5 sec pulse off) in an ice bath. After sonication, 1 mL of the $CuSO_4$ stock solution (0.025 mmol, 0.05 eq.) was added to each vial while stirring, followed by the addition of BnOH (0.5 mmol, 1 eq.). The mixtures were directly exposed to air and stirred at 25 ℃ for 1 h. The conversion and selectivity were monitored by ^{1}H NMR. All reactions were performed 3 times in parallel.
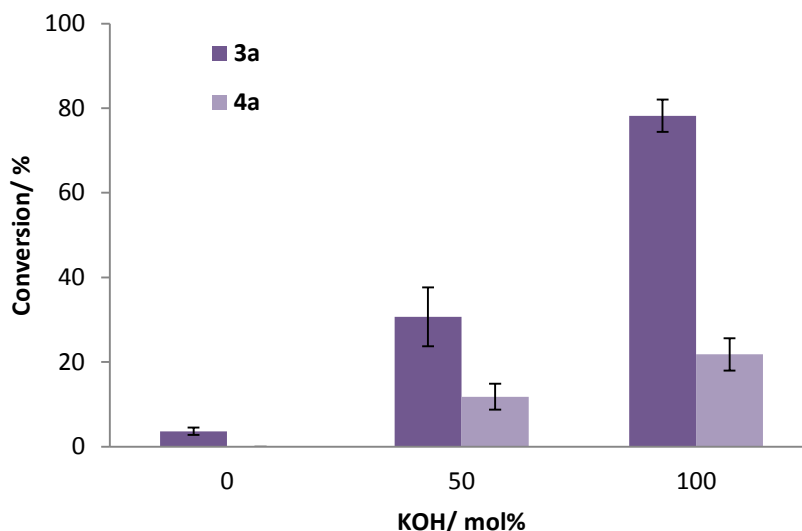

Figure 2.17 Variation in the amount of SDS. Conditions: 0.5 mmol of BnOH; 5 mol % $CuSO_4$; 5 mol % bpy; 5 mol % TEMPO; 0-0.2 M SDS (0 – 200 mol %); 50 mol %

DMAP; 5 mL of H_2O; Air; 25 ℃; 1 h. Each reaction was run 3 times in parallel. No acid

byproduct was observed.

Determination of conversion and selectivity by ^{1}H NMR

25 μL of the reaction mixture was added to 0.6 mL of $CDCl_3$. After vigorous shaking,

the organic phase was separated and transferred to a NMR tube via syringe for ^{1}H NMR

analysis. The conversion and selectivity of the reaction could then be calculated based on

integrations of the characteristic peaks of benzyl alcohol, benzaldehyde and benzoic acid

(**Figure 2.18**).
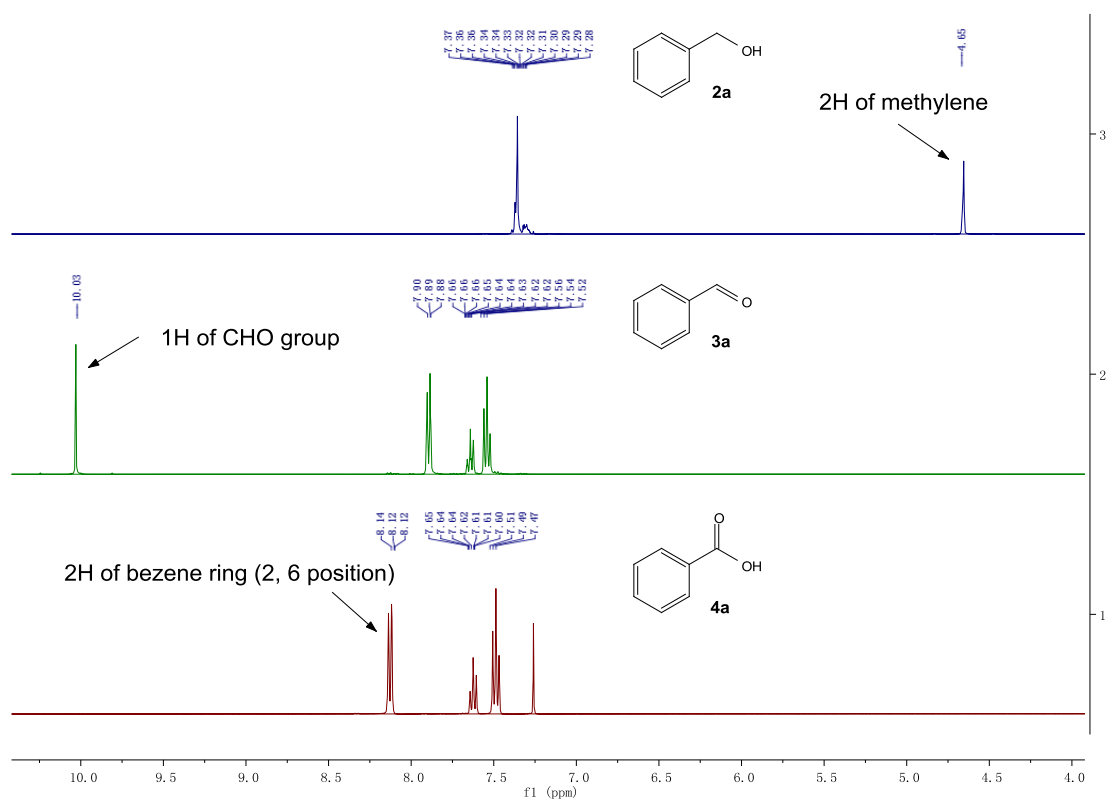
Figure 2.18 ^{1}H NMR spectra of benzyl alcohol, benzaldehyde, and benzoic acid.

2.3.6.2 Alcohol Oxidation with TEMPO Derivatives

General notes

Stock solutions were prepared as such: **1** in H_2O (0.025 M), DMAP in H_2O (0.25 M), $CuSO_4$ in H_2O (0.025 M) and KOH in H_2O (0.025 M). Unless otherwise noted, all the reactions were stirred at 25 °C for 1 h.

General procedure for the oxidation catalyzed by Cu/TEMPO derivatives

To a 20 mL vial, 0.025 mmol of the TEMPO derivative was added (sulfonate derivatives were converted to potassium salts prior to use by adding 1 mL of the 0.025 M KOH stock solution). Then, the DMAP stock solution (0.25 M) and water were added as indicated in Table S3. The solution was then sonicated using a Branson digital sonifier (microtip, 65% power, 4 min, 5 sec pulse on, 5 sec pulse off) in an ice bath. After sonication, $CuSO_4$ was added as inidicated, followed by the addition of 0.5 mmol of BnOH. The mixtures were stirred for 1 h while exposed to air or with an oxygen balloon (Table S3). The conversion and selectivity were determined by ^1H NMR.

Table 2.9 The oxidation of benzyl alcohol catalyzed by $CuSO_4$ and TEMPO derivatives.[a]
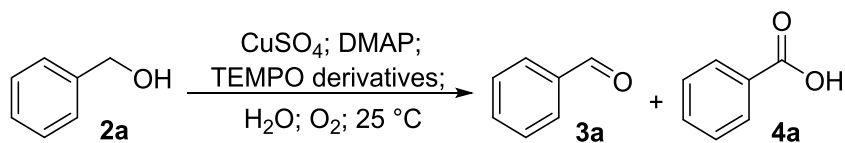
Entry	Catalyst, [5 mol %]	$CuSO_4$, [mol %]	DMAP, [mol %]	O_2 Source	3a, [%][b]	4a, [%][b]

1	**1**	1	20	air	60	-
2	**1**	2.5	20	air	86	-
3	**1**	2.5	10	air	48	-
4	**1**	2	20	air	93	-
5	**1**	2	10	O_2	56	-
6	**1**	0.2	20	O_2	55	-
7	**1**	0.4	20	O_2	71	-
8	**1**	2	20	O_2	98 ± 2	-
9	TEMPO	2	20	O_2	48 ± 4	-
10[c]	TEMPO	2	20	O_2	83 ± 4	10 ± 3
11	**5 K**	2	20	O_2	26 ± 1	-
12	**6**	2	20	O_2	39 ± 4	-

(a) Reaction conditions: 0.5 mmol of BnOH in 5 ml of water, 25 °C, magnetic stirring, 1 hour. (b) Determined by ^{1}H NMR. Results are averages from three independent experiments. (c) In the presence of 100 mM SDS.

General procedure for the catalysis scope study

To a 20 mL vial, 1 mL stock solution of the **1** (0.025 mmol, 0.05 eq.) was added, followed by the addition of 0.4 mL of the DMAP stock solution (0.1 mmol, 0.2 eq.) and 3.2 mL of water. The solution was then sonicated using a Branson digital sonifier (microtip, 65% power, 4 min, 5 sec pulse on, 5 sec pulse off) with an ice bath. After sonication, 0.4 mL stock solution of $CuSO_4$ (0.01 mmol, 0.02 eq.) was added to each vial, followed by the addition of the alcohol substrates (0.5 mmol, 1 eq.) and an oxygen balloon was used as the oxygen source. The conversion and selectivity were monitored via TLC, ^{1}H NMR and GC-MS.

General procedure for product isolation

Once the reaction was completed, the reaction mixture was extracted by ethyl ether (5 mL × 4) in the reaction vial. The organic layers were transferred by syringe, combined and dried with anhydrous $MgSO_4$, then filtered through a pad of silica gel and washed

with ethyl ether until no product could be detected from the eluent by TLC. Ethyl ether was then removed by a rotary evaporator and the product was dried under vacuum.

2.3.6.3 Cryo-TEM

General procedure

Cryo-TEM samples were vitrified by ultra-rapid freezing. Typically, the sample was deposited on a Quantifoil grids (Quantifoil Inc., Jena, Germany), and plunge-frozen in liquid ethane. Grids were imaged at liquid nitrogen temperatures using a Titan Krios (FEI Company, OR) operating at 300 kV and equipped with a $2k \times 2k$ CCD placed at the end of Gatan energy filter. Each 2D projection image was acquired with electron doses of ~ 200 electrons/Å^2.

Cryo-TEM image of 1 in water

To 0.2 mL of the **1** stock solution (0.025 M), 1 mg of KCN (a salt complex dosed with trace amounts of copper) and 0.8 mL of H_2O were added. The mixture was then sonicated using a Branson digital sonifier (microtip, 65% power, 4 min, 5 sec pulse on, 5 sec pulse off) with an ice bath to keep the mixture cool. After sonication, the sample was filtered through a 0.45 μm PTFE membrane.

Cryo-TEM image of 1 with DMAP and copper in water

To 0.2 mL of the **1** stock solution (0.025 M), 80 μL of the DMAP stock solution (0.25 M), 80 μL of the $CuSO_4$ stock solution (0.025 M) and 0.64 mL of H_2O were added. The mixture was then sonicated using a Branson digital sonifier (microtip, 65% power, 4 min,

5 sec pulse on, 5 sec pulse off) with an ice bath. After sonication, the sample was filtered through a 0.45 μm PTFE membrane.

Cryo-TEM image of reaction mixture

To 0.2 mL of the **1** stock solution (0.025 M), 80 μL of the DMAP stock solution (0.25 M), 80 μL of the CuSO$_4$ stock solution (0.025 M), 0.64 mL of H$_2$O and 10 μL of BnOH were added. The mixture was then sonicated using a Branson digital sonifier (microtip, 65% power, 4 min, 5 sec pulse on, 5 sec pulse off) with an ice bath. After sonication, the sample was filtered through a 0.45 μm PTFE membrane and protected under an Ar atmosphere.

2.3.6.4 Measuring Dissolved Oxygen

5 mL of blank sample (deionized water) and micellar solutions of **1** (0.4 wt%, 5 mM) and SDS (0.4 wt%, 14 mM) were each prepared in 20 mL vials respectively. The samples were sonicated using a Branson digital sonifier (microtip, 65% power, 4 min, 5 sec pulse on, 5 sec pulse off) with an ice bath. After sonication, the solutions were stirred (300 rpm) at 25 °C. The samples were then flushed with a flow of oxygen for 1 min, capped and vigorously shaken. The caps were removed and the DO was measured using a Mettler Toledo SG6 SevenGo Pro with an Inlab 605 dissolved oxygen probe and recorded every 5 min. For each sample, the measurement was repeated 3 times in parallel.

2.3.6.5 Organic Synthetic Details

General notes

Flash chromatography was performed using Merck Kieselgel 60 (230-400 mesh) silica. Reactions requiring anhydrous conditions were performed under argon using standard Schlenk line techniques. Prior to use, THF was purified by refluxing over sodium in the presence of benzophenone until a persistent blue color appeared and then the solvent was collected via distillation.

10-Azido-1,1,1,2,2,3,3,4,4,5,5,6,6,7,7,8,8-heptadecafluorodecane.
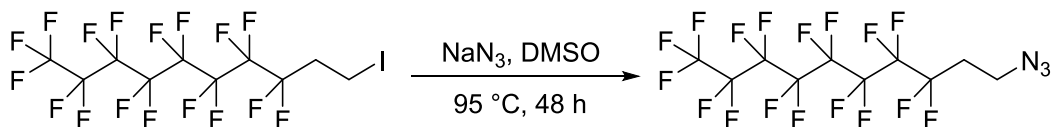
1,1,1,2,2,3,3,4,4,5,5,6,6,7,7,8,8-Heptadecafluoro-10-iododecane (3.0 g, 5.2 mmol) was dissolved in DMSO (16 mL), and then sodium azide (0.51 g, 7.8 mmol) was added to the solution. The resulting mixture was heated to 95 °C for 48 h. The solution was allowed to cool down to the room temperature and a white precipitate formed. The resulting mixture was transferred into in a separatory funnel and diluted with water (100 mL). The mixture was extracted 4 times with diethyl ether (30 mL). Ether phases were combined, washed with water, dried with $MgSO_4$, and evaporated in vacuum to yield crude azide. The crude azide was dissolved in 2 mL of pentane and filtered through a pad of silica. The sorbent was washed with 100 mL of pentane, and the solvent evaporated in vacuum to get 1.98 g of a colorless liquid, which became colorless crystals during storage at +4 °C under nitrogen. Yield, 80%. ^{1}H NMR (400 MHz, $CDCl_3$) δ 3.62 (t, $J = 7.2$ Hz, 2H), 2.47 − 2.31 (m, 2H). ^{13}C NMR (101 MHz, $CDCl_3$): 43.5, 31.0 (t, $J = 22.0$ Hz). ^{19}F NMR (377 MHz, $CDCl_3$) δ -80.84, -114.00, -121.72, -121.96, -122.77, -123.53, -126.18.

N-propargyl-4-amino-TEMPO.
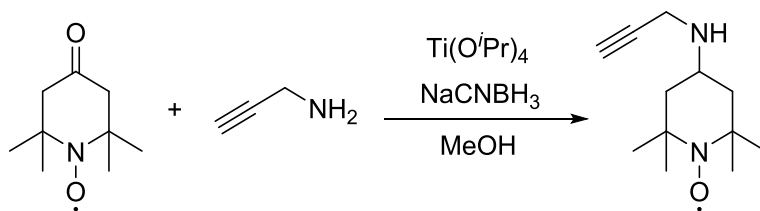
Ti(O*i*Pr)$_4$ (1.6 g, 5.63 mmol) was added to 4-oxo-TEMPO (0.8 g, 4.7 mmol) and the mixture was stirred for 20 min. Propargylamine (0.52 g, 9.4 mmol) was then added portion wise and the resulting reaction mixture was stirred for another 1.5 h. The mixture was diluted with methanol (5 mL) prior to the addition of NaBH$_3$CN (0.3 g, 4.7 mmol). The solution was stirred for another 24 h. The reaction was stopped upon the addition of water (20 mL), and the inorganic precipitate that formed was removed via filtration and rinsed with ethanol (25 mL). The resulting mixture was concentrated *in vacuo* prior to the addition of ethyl acetate (10 mL). The layers were separated and the aqueous layer was extracted with ethyl acetate (10 mL $\times$ 3). The combined organic layers were washed with brine (10 mL $\times$ 3) and dried over MgSO$_4$. Purification by column chromatography with ethyl acetate as the eluent gave 0.56 g of an orange powdered product (57% yield). MS (ESI) *m/z*: [M + H]$^+$: 210.2; IR (neat, cm^{-1}): 3295, 3235, 2982, 2930, 1603, 1456, 1362, 1340, 1175, 1113, 1086; HRMS (ESI) calculated for [C$_{12}$H$_{22}$N$_2$O]$^+$: 210.1732, found: 210.1720.

4-((3-sulfopropyl)amino)-TEMPO (5) and its potassium salt (5 K).
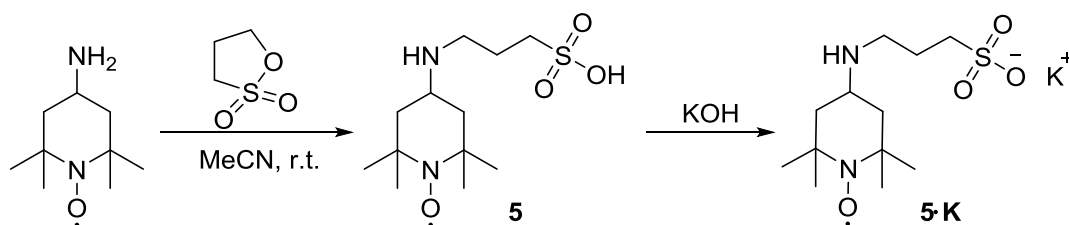
4-Amino TEMPO (1.71 g, 10 mmol) was dissolved in MeCN (50 mL), and then 1,3-Propane sultone (1.23 mg, 10 mmol) was added to the solution. The mixture was stirred at room temperature overnight and becoming cloudy. The mixture was filtered and was washed with MeCN (5 mL × 3) to give 2.89 g of **5** as an organge solid (99% yield). MS (ESI) *m/z*: $[M - H]^-$: 292.1; IR (neat, cm^{-1}): 3446, 3398, 3091, 2983, 2946, 2880, 1563, 1467, 1245, 1204, 1160, 1034; HRMS (ESI) calculated for $[C_{12}H_{24}N_2O_4S]^-$: 292.1457, found: 292.1455. The potassium salt **5·K** was obtained by mixing **5** with 1 eq. of KOH in water and used as an aqueous solution.

4-(propargyl(3-sulfopropyl)amino)-TEMPO. (S3)
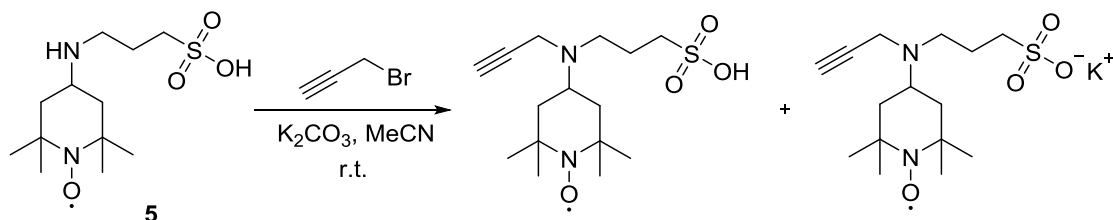
5 (0.73 g, 2.5 mmol) and K$_2$CO$_3$ (0.69 g, 5 mmol) were suspended in MeCN (30 mL). Propargyl bromide (80% in toluene, 1.49 g, 10 mmol) was added to the solution and then the mixture was stirred at room temperature overnight. The next day, the solvent was removed by distillation under reduced pressure and dissolved again in 20 mL EtOAc/MeOH (10:1). The insoluble solid was filtered off and washed with the

EtOAc/MeOH solvent mixture. Then the filtrate was evaporated and the crude product purified via silica-gel chromatography using MeOH/EtOAc (10%–20%) as eluent to give a mixture of **S3** and **S3·K** (0.73:1 molar ratio; estimated using ICP-OES) as an orange solid (0.67 g). MS (ESI) m/z: [M − H]$^-$: 330.1; IR (neat, cm^{-1}): 3419, 3246, 2975, 2936, 1599, 1462, 1363, 1170, 1038; HRMS (ESI) calculated for [C$_{15}$H$_{26}$N$_2$O$_4$S]$^-$: 330.1613, found: 330.1615. ICP-OES: S, 8.37; K 5.88.

Potassium 4-(((1-(3,3,4,4,5,5,6,6,7,7,8,8,9,9,10,10,10-heptadecafluorodecyl)-1H-1,2,3-triazol-4-yl)methyl)(3-sulfopropyl)amino)-TEMPO. (1)
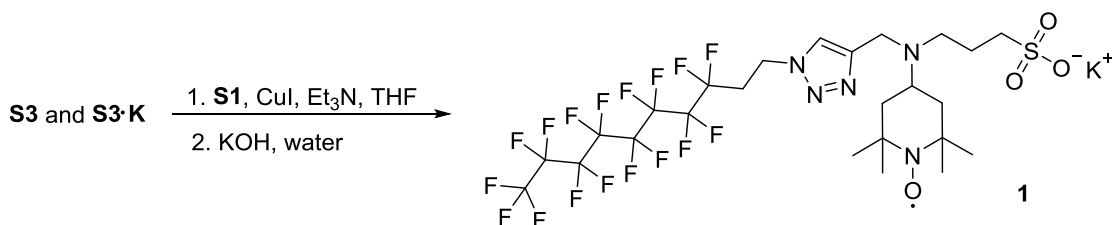
A mixture of **S3** and **S3·K** (molar ratio 0.73 : 1, 331 mg), **S1** (510 mg, 1.05 mmol) and 20 ml of THF were added to a 100 mL schlenk flask. Then CuI (19 mg, 0.1 mmol) and 0.1 mL triethylamine were added under an argon atmosphere. The mixture was left to stir at room temperature overnight, and then the solvent was removed via rotary evaporation. The crude product was purified by silica-gel chromatography, using MeOH/EtOAc (10%–20%) as the eluent. The resulting orange crystals (640 mg) were determined to be a mixture of potassium salt **1** and its corresponding acid. 513 mg of the mixture was dissolved in 10 mL of water in a 25 mL volumetric flask and then a 1 M solution of KOH was added to adjust pH to 7.5. The volume was adjusted to 25 mL, and this was then used as a stock solution of **1** in water (25 mM) for future catalytic experiments. MS (ESI) m/z:

[M − H]⁻: 819.2; IR (neat, cm⁻¹): 3438, 2982, 1466, 1368, 1198, 1144, 1115, 1035;

HRMS (ESI) calculated for $[C_{25}H_{30}F_{17}N_5O_4S]^-$: 819.1747, found: 819.1726.

4-(((1-(3,3,4,4,5,5,6,6,7,7,8,8,9,9,10,10,10-heptadecafluorodecyl)-1H-1,2,3-triazol-4-yl)methyl)amino) -TEMPO. (6)
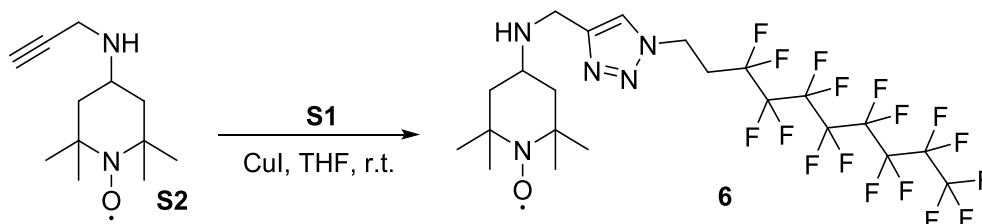
To a 50 mL schlenk flask, **S2** (50 mg, 0.239 mmol), **S1** (117 mg, 0.24 mmol) and 10 ml of THF were added. Then 5 mg of CuI and 0.2 mL of triethylamine were added under an argon atmosphere. After stirring at room temperature overnight, 50 mg of QuadraSil™ MP was added to remove the copper salt. The mixture was then filtered, and the solvent removed via rotary evaporation. The crude product was washed by pentane (5 mL × 3) to give 142 mg of **6** as orange solid (85% yield). MS (ESI) *m/z*: [M + H]⁺: 699.1; IR (neat, cm⁻¹): 2977, 2932, 1465, 1374, 1335, 1198, 1145, 1114, 1049, 1030; HRMS (ESI) calculated for $[C_{22}H_{26}F_{17}N_5O]^+$: 699.1866, found: 699.1833.

2.3.6.6 NMR Data

Benzaldehyde[23] (3a)
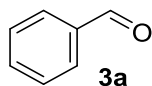
Colorless oil. ^{1}H NMR (400 MHz, CDCl$_3$) δ 10.03 (s, 1H), 7.92 – 7.86 (m, 1H), 7.67 – 7.60 (m, 1H), 7.54 (t, *J* = 7.5 Hz, 1H). ^{13}C NMR (126 MHz, CDCl$_3$) δ 192.5, 136.4, 134.6, 129.8, 129.1.

4-Fluorobenzaldehyde[53] (3b)
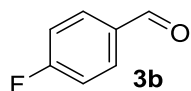
Colorless oil. ^{1}H NMR (400 MHz, CDCl$_3$) δ 9.97 (s, 1H), 7.95 – 7.87 (m, 2H), 7.26 – 7.18 (m, 2H). ^{13}C NMR (101 MHz, CDCl$_3$) δ 190.6 (s), 166.6 (d, *J* = 256.7 Hz), 133.1 (d, *J* = 2.6 Hz), 132.3 (d, *J* = 9.7 Hz), 116.5 (d, *J* = 22.3 Hz).

4-Methoxybenzaldehyde[23] (3c)
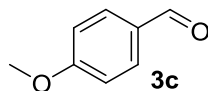
Slightly yellow oil. ^{1}H NMR (400 MHz, CDCl$_3$) δ 9.84 (s, 1H), 7.80 (d, *J* = 8.8 Hz, 2H), 6.97 (d, *J* = 8.7 Hz, 2H), 3.85 (s, 3H). ^{13}C NMR (101 MHz, CDCl$_3$) δ 190.8, 164.6, 132.0, 130.0, 114.3, 55.6.

4-Isopropylbenzaldehyde[54] (3d)
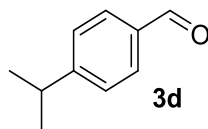
Yellow oil. ^{1}H NMR (400 MHz, CDCl$_3$) δ 9.94 (s, 1H), 7.79 (d, J = 8.2 Hz, 2H), 7.36 (d, J = 8.1 Hz, 2H), 2.96 (dt, J = 13.8, 6.9 Hz, 1H), 1.26 (d, J = 6.9 Hz, 6H). ^{13}C NMR (101 MHz, CDCl$_3$) δ 191.9, 156.2, 134.6, 130.0, 127.1, 34.5, 23.6.

4-Chlorobenzaldehyde[54] (3f)
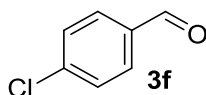
White solid. ^{1}H NMR (500 MHz, CDCl$_3$) δ 9.98 (s, 1H), 7.83 (d, J = 7.9 Hz, 2H), 7.51 (d, J = 8.0 Hz, 2H). ^{13}C NMR (126 MHz, CDCl$_3$) δ 190.9, 140.9, 134.7, 130.9, 129.5.

2-Thiophenecarboxaldehyde[23] (3i)
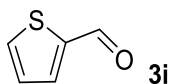
Yellow oil. ^{1}H NMR (500 MHz, CDCl$_3$) δ 9.93 (s, 1H), 7.80 – 7.73 (m, 2H), 7.21 – 7.20 (m, 1H). ^{13}C NMR (126 MHz, CDCl$_3$) δ 183.1, 144.0, 136.5, 135.2, 128.4.

Cinnamaldehyde[23] (3j)
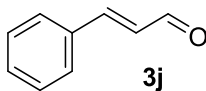
Yellow oil. ^{1}H NMR (600 MHz, CDCl$_3$) δ 9.69 (d, J = 7.7 Hz, 1H), 7.57 – 7.52 (m, 2H), 7.46 (d, J = 16.0 Hz, 1H), 7.44 – 7.39 (m, 3H), 6.70 (dd, J = 15.9, 7.7 Hz, 1H). ^{13}C NMR (151 MHz, CDCl$_3$) δ 193.7, 152.8, 134.0, 131.3, 129.1, 128.6, 128.5.

Mixture of Geranial[23] (3l) and Neral[55] (3m) (3 : 2)
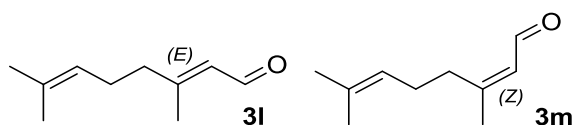
Yellow oil. Geranial : Neral = 3 : 2. ^{1}H NMR (500 MHz, CDCl$_3$) δ 9.95 (d, *J* = 8.1 Hz, 0.6H), 9.85 (d, *J* = 8.3 Hz, 0.4H), 5.84 (d, *J* = 8.0 Hz, 1H), 5.09 – 4.99 (m, 1H), 2.55 (t, *J* = 7.5 Hz, 0.8H), 2.24 – 2.11 (m, 5H), 1.95 (d, *J* = 1.1 Hz, 1.2H), 1.64 (s, 3H), 1.59 – 1.52 (m, 3H). ^{13}C NMR (126 MHz, CDCl$_3$) δ 191.4, 190.9, 164.0, 164.0, 133.7, 132.9, 128.6, 127.4, 122.6, 122.3, 40.6, 32.6, 27.0, 25.71, 25.67, 25.1, 17.7, 17.6.

(S)-(−)-perillaldehyde[56] *(3n)*
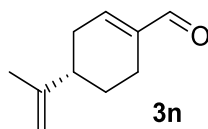
Colorless oil. ^{1}H NMR (500 MHz, CDCl$_3$) δ 9.44 (s, 1H), 6.84 (s, 1H), 4.78 (s, 1H), 4.74 (s, 1H), 2.54 – 2.40 (m, 2H), 2.31 – 2.20 (m, 2H), 2.18 – 2.06 (m, 1H), 1.97 – 1.87 (m, 1H), 1.77 (s, 3H), 1.51 – 1.39 (m, 1H). ^{13}C NMR (126 MHz, CDCl$_3$) δ 194.0, 150.8, 148.4, 141.3, 109.6, 40.7, 31.8, 26.4, 21.6, 20.8.

2.3.7 Conclusions

In conclusion, we explored the reactivity of the Cu/TEMPO catalytic system for oxidation of alcohols to aldehydes in aqueous micellar media. While this chemistry could be coerced into water with the help of SDS, the optimal reaction conditions were found impractical. To address this problem, we synthesized an enzyme-inspired, trifunctional surfactant **1** which is catalytically competent at practical, millimolar concentrations.

Unlike TEMPO, **1** does not require additional Cu ligands, or a high loading of base. Solutions of **1** show evidence for O_2 pre-concentration within the fluorous cores of the micelles. Investigations of functional soft materials capable of sequestering O_2 and other gases for reactions in liquid phase are under way in our laboratories.

Chapter 3.

Efficient and Stable Molecular Water Oxidation Catalysts: A Hydrophobic Approach

3.1 Introduction

Development of an easy means of photo/electrocatalytic water splitting is one of the main barriers to establishing a solar hydrogen economy.[57, 58] Of the two half-reactions involved in splitting water into O_2 and H_2, the water oxidation reaction (WOR) presents the most challenge due to its mechanistic complexity.[59-61] A practical WOR catalyst must be highly active, yet inexpensive and indefinitely stable under harsh oxidative conditions.

A number of catalytic systems for water oxidation have been devised, incorporating either platinum group[62-69] or base metals.[67, 70-78] Due to cost considerations, the latter are more suitable for practical applications. Heterogeneous catalysts based on metal-oxide phases are stable and readily accessible.[67, 71, 79-81] However, characterization, mechanistic studies, and rational tuning of properties remain a challenge for these inorganic phases. In contrast, molecular metal-complex catalysts can be tailored using the full arsenal of organic chemistry. Mechanistic understanding, essential for the rational design of catalysts, is easier to achieve for these systems.[78, 82-87] To date, application of molecular

catalysts for WOR has been restricted by their synthetic complexity and limited stability under WOR conditions.[88-90] Decomposition of molecular species sometimes yields catalytically active oxide phases,[79, 80, 90-92] which may complicate the identification of the operational catalyst.[90, 91]

Recently, we reported on water electrooxidation catalyzed by hydrophobic, insoluble perfluorinated cobalt phthalocyanine (CoFPc) physisorbed on fluorine-doped tin oxide (FTO).[93] This molecular catalyst is exceptionally active. Importantly, the stability of "fluorine-armored" CoFPc is vastly superior to that of previously described hydrophobic molecular catalysts,[94, 95] and is comparable to particulate cobalt phosphate system (CoPi).[71] However, the inflexible and inert nature of the FPc ligand precluded an in-depth exploration of structure-activity relationships or improvement of the catalytic activity.

3.2 An Efficient and Stable Hydrophobic Molecular Cobalt Catalyst for Water Electrooxidation at Neutral pH

In this work, we describe a library approach to molecular catalysts for WOR based on the cobalt complex of tris(2-benzimidazolylmethyl)amine, **(BimH)$_3$**.[96-98] This parent structure was chosen due to its diverse coordination chemistry and ease of derivatization.[98] A range of catalysts differing in their electronic properties, surface affinity, and steric bulk was screened. Hydrophobicity was identified as the key variable in mediating the catalytic competence of **Co-(BimR)$_3$** complexes. The change in this parameter correlates both with the conformational mobility of the ligand core and the structural changes in the local solvent environment around the catalytic metal site. The

optimal ligand identified in this study is extremely hydrophobic due to its three semifluorinated side chains. The corresponding Co complex catalyzes water electrooxidation efficiently, with an onset potential comparable to that for CoPi, but with a higher turnover frequency (TOF) and in the absence of soluble Co salts. As an added benefit, the hydrophobic catalyst can be immobilized on the electrode through physisorption, and remains stable over prolonged electrolysis at a high potential of 1.9 V vs RHE. This makes the catalyst potentially suitable for application in practical devices.
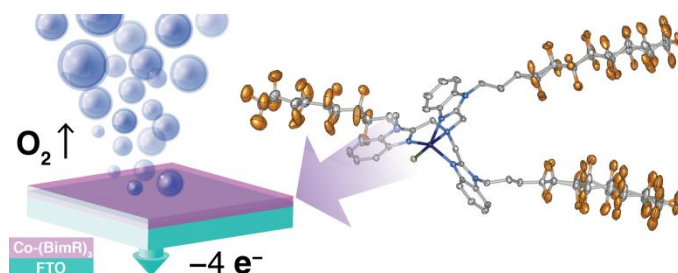
Figure 3.1 Immobilization of catalysts on electrode for electrocatalytic water oxidation.

3.2.1 The Synthesis of the Library of Catalysts

The parent **(BimH)₃** and its phenyl-substituted variants **(BimH/R)₃** (**Figure 3.2 A**) were synthesized by direct condensation of nitrilotriacetic acid or nitrilotriacetyl chloride with 1,2-phenylenediamines (**Scheme 3.1**, in **Section 3.2.3.1**). The N-alkylated derivatives **(BimR)₃** were obtained through deprotonation of **(BimH)₃** with *t*-BuOK followed by alkylation (**Scheme 3.2**, in **Section 3.2.3.1**). The unsymmetrical derivatives were obtained via reductive amination reactions between **H(BimH)₂** and suitable benzimidazole-2-carbaldehydes (**Scheme 3.3**, in **Section 3.2.3.1**). The corresponding

cobalt complexes were readily synthesized by reacting the ligands with anhydrous $CoCl_2$ in refluxing THF.
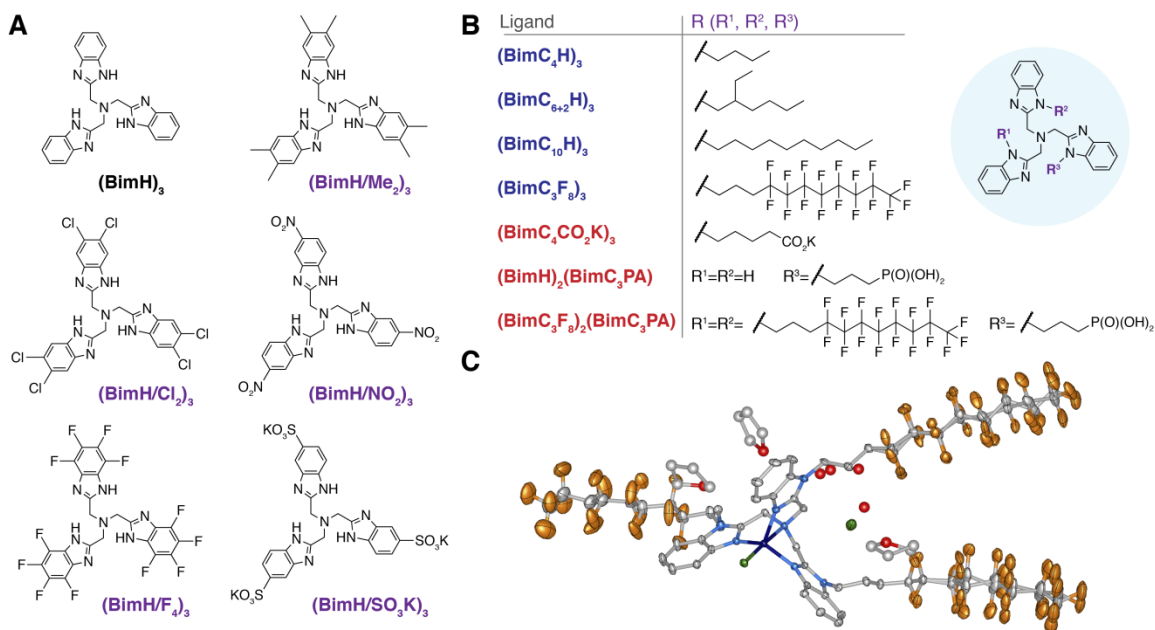
Figure 3.2 Library of the tris-benzimidazole Co complexes. (A) **(BimH)$_3$** and its phenyl-substituted variants **(BimH/R)$_3$**. (B) *N*-alkylated variants **(BimR)$_3$**. Substituents: **C$_n$R** = chain of *n* methylene groups terminated with R; **F$_8$** = $(CF_2)_7CF_3$; **PA** = $P(O)(OH)_2$. (C) Single-crystal X-ray structure of **Co-(BimC$_3$F$_8$)$_3$**. Displacement ellipsoids drawn at the 30% probability level. Two disordered fluorous chains are modeled in two positions. Hydrogen atoms are omitted for clarity.

3.2.2 The Performance of Electrocatalytic Water Oxidation

With the library of the complexes in hand, we proceeded to screen the members for electrocatalytic activity. To prepare the working electrodes for electrochemistry experiments, drops of Co complex solutions of known concentrations were spread on

small slides of FTO-coated glass and dried.[93] The resulting electrodes had loadings of 0.5 nmol·cm^{-2}. Most of the experiments were performed in a 10 mL electrochemical cell with 1 cm^2 working electrodes. Thus, the highest bulk solution concentration of Co ions that could be reached in our experiments in the case of quantitative decomposition of the molecular complexes is 50 nM. Such a low concentration of soluble Co is ordinarily insufficient to generate catalytically meaningful heterogeneous CoO_x.[84]

All the cyclic voltammetry (CV) and controlled potential electrolysis (CPE) experiments were conducted at rt in 0.1 M potassium phosphate buffer at pH 7. A three-electrode cell with the modified FTO slide as a working electrode, a spiral Pt counter electrode, and an Ag/AgCl reference was used. CPE traces were recorded at 1.9 V vs. RHE. The onset potentials and TOFs of the catalysts were determined as described previously.[93] It is important to note that none of the ligands were electroactive or electrocatalytic on their own in the absence of Co.
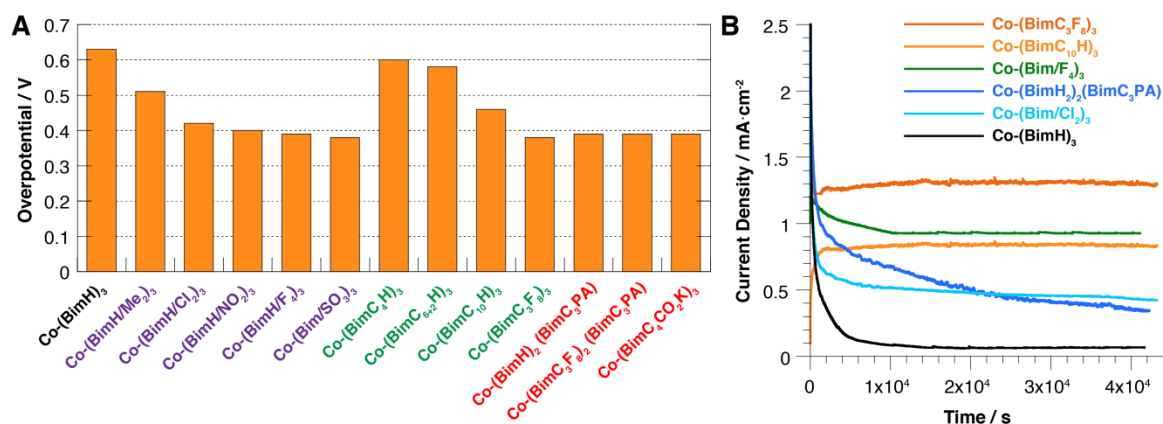
Figure 3.3 (A) WOR overpotentials for a range of benzimidazole Co complexes. Purple: phenyl-functionalized complexes; green: imidazole-alkylated complexes; red:

complexes with covalent linkers. (B) CPE traces at 1.91 V vs RHE for selected cobalt complexes. Trace colors denote the mode of deactivation.

The parent **Co-(BimH)₃** complex did catalyze WOR. The required overpotential of 0.63 V (**Figure 3.3 A**) was higher than that for CoFPc under the same conditions (0.48 V). At the same time, the stability of **Co-(BimH)₃** was poor. During CPE, the catalytic current density dropped to a negligible level rapidly and monotonously in ~1 h, indicating a chemical change or desorption of the complex from the electrode (**Figure 3.3 B**, black trace). Importantly, we did not observe any rise in current density could be indicative of the gradual formation of a catalytic CoO_x particulate phase.

All the substituted variations of **Co-(BimH)₃** were found to be more active than the parent complex. Among the phenyl-substituted derivatives (**Figure 3.3 A**, purple labels), there was a correlation of the lower overpotential for WOR with the electron-withdrawing ability of the substituents. The lowest overpotential in this series, 0.39 V, was attained by **Co-(Bim/F₄)₃** and **Co-(Bim/SO₃K)₃**. A similar dramatic improvement in the WOR overpotential was observed for the complexes bearing pendant carboxylate or phosphonate groups that can form covalent bonds with metal-oxide surfaces, such as FTO.[99] All three of the complexes in this series, **Co-(BimC₄CO₂K)₃**, **Co-(BimH)₂(BimC₂PA)** and **Co-(BimC₃F₈)₂(BimC₂PA)** exhibited the same 0.39 V overpotential for WOR as the most active phenyl-substituted catalysts (**Figure 3.3 A**, red labels).

The trend observed for the imidazole-alkylated ligand series (**Figure 3.3 A**, green labels) strongly favored the more hydrophobic and sterically bulky complexes. Thus, the

WOR overpotential dropped from 0.5 V for **Co-(BimC$_4$H)$_3$** to 0.39 V for **Co-(BimC$_3$F$_8$)$_3$**. These observations strongly suggested that the nature of interaction between the electrocatalyst and the supporting electrode could be just as important as the electronic properties of the operational catalytic site. We would further like to note that the overpotential of 0.39 V for WOR is comparable to that attained for the best heterogeneous cobalt catalysts,[70, 71] and unprecedented for a molecular Co-based catalyst.

Following the initial CV screening, we explored the stability of the complexes in prolonged CPE (1.91 V vs RHE). While most substituted variants proved to be more resilient than the parent **Co-(BimH)$_3$**, gradual deactivation was observed for most of the catalysts in the library (**Figure 3.12**, **Figure 3.13** and **Figure 3.14**, in **Section 3.2.3.3**). The character of deactivation was distinct for various catalysts. For most of the complexes, the decrease in the catalytic current density was steady and uniform, approaching zero on the timescale of 24 h (**Figure 3.3 B**, blue traces). This occurred for the covalently-linked complexes **Co-(BimC$_4$CO$_2$K)$_3$**, **Co-(BimH)$_2$(BimC$_2$PA)** and **Co-(BimC$_3$F$_8$)$_2$(BimC$_2$PA)**, as well as for **Co-(Bim/Me$_2$)$_3$**, **Co-(Bim/Cl$_2$)$_3$**, and **Co-(Bim/SO$_3$K)$_3$**. For several members of the library, most notably, the electron-deprived **Co-(Bim/F$_4$)$_3$** and **Co-(Bim/NO$_2$)$_3$**, the observed current density decreased on the timescale of 1-3 hours, settling into a steady state (**Figure 3.3 B**, green trace). We did not observe an increase in current density over time for any for the complexes.

Gratifyingly, two of the complexes in the library, the hydrophobic **Co-(BimC$_{10}$H)$_3$** and **Co-(BimC$_3$F$_8$)$_3$**, exhibited remarkable stability in the CPE experiment (**Figure 3.3 B**, orange traces). For both of these catalysts, there was no measurable change in catalytic

current density even after 12+ hours of CPE. **Co-(BimC$_{6+2}$H)$_3$** was also stable on the same timescale. However, the catalytic current density and the apparent turnover frequency (TOF) for this catalyst were low. As the extremely hydrophobic **Co-(BimC$_3$F$_8$)$_3$** was the most promising member of the library, we chose it for an in-depth investigation of its catalytic properties and stability.

Since we could not immediately exclude the possibility of the degradation of the complex or some other chemical change happening on the electrode,[90, 91] several experiments were performed to assess the possible role of heterogeneous CoO_x phases or free Co ions in the observed catalytic activity. No characteristic black/brown cobalt phosphate particulate film was observed on the electrode after 12 hours of CPE at 1.91 V vs RHE. A clearly visible heterogeneous film forms on the electrode surface immediately after few CV scans in the same buffer solution containing 0.5 mM $Co(NO_3)_2$. Furthermore, CVs of the **Co-(BimC$_3$F$_8$)$_3$**@FTO electrodes before and after CPE were identical (**Figure 3.17**, in **Section 3.2.3.3**). No free Co could be detected by inductively coupled plasma optical emission spectrometry (ICP-OES) in the electrolyte after 12 h of CPE. After this experiment, CV was collected for a blank FTO electrode using the same electrolyte solution. No redox or catalytic activity was observed, indicating that there was no appreciable amount of free Co^{2+} released from **Co-(BimC$_3$F$_8$)$_3$**@FTO.

To further control for the release of free Co in the solution, CVs of **Co-(BimC$_3$F$_8$)$_3$**@FTO were obtained in the presence of disodium salt of ethylenediamine tetraacetic acid (Na$_2$EDTA), a potent scavenging agent for Co^{2+} ions.[84] The experiment was unaffected by the presence of Na$_2$EDTA (**Figure 3.18**, in **Section 3.2.3.3**). In

contrast, Na_2EDTA completely suppressed all the WOR activity in a control experiment with a plain FTO electrode in the presence of 1 mM $Co(NO_3)_2$.

We interrogated the behavior of **Co-(BimC$_3$F$_8$)$_3$** and other imidazole-alkylated variants over a broad range of pH values (**Figure 3.9**, **Figure 3.10** and **Figure 3.11**, in **Section 3.2.3.3**). It is readily apparent that WOR overpotentials for all the complexes decrease monotonically with increasing pH (**Figure 3.9**, in **Section 3.2.3.3**). For **Co-(BimC$_3$F$_8$)$_3$**, we found a slope of -63 mV/pH between pH 1 and 13 (**Figure 3.10**, in **Section 3.2.3.3**). This value is close to the theoretical -59 mV/pH predicted by the Nernst equation for a proton-coupled electron transfer (PCET) process. Remarkably, **Co-(BimC$_3$F$_8$)$_3$**@FTO still shows detectable WOR catalytic activity down to pH = 1 (**Figure 3.11 A**, in **Section 3.2.3.3**). Quasi-reversible redox couples at potentials lower than the catalytic wave are readily discernible for all the complexes down to pH 3 (**Figure 3.11**, in **Section 3.2.3.3**). These waves are also pH-dependent (-95 mV/pH for **Co-(BimC$_3$F$_8$)$_3$**), consistent with reversible oxidation of the $Co(II)$-OH_2 form to $Co(III)$-OH via PCET (**Figure 3.10**, in **Section 3.2.3.3**). These data strongly indicate that decomposition of the catalysts to CoO_x is not likely, as such cobalt oxide phases are quite unstable in acidic solutions.[100]

Finally, a **Co-(BimC$_3$F$_8$)$_3$**@FTO electrode that was used in a prolonged CPE experiment was washed extensively with methanol. The UV-Vis spectra of the **Co-(BimC$_3$F$_8$)$_3$** solutions washed from the electrode before and after prolonged CPE were identical (**Figure 3.20 A**, in **Section 3.2.3.4**), and ESI-MS spectrum did not indicate formation of any new molecular species (**Figure 3.19**, in **Section 3.2.3.4**).[84, 100] The washed electrode did not show any WOR catalytic activity and behaved identically to a

pristine FTO electrode, indicating that the acting catalyst is soluble in organic solvents. The electrode was then extracted with aqua regia. No Co was detected in this wash by ICP-OES. These observations strongly indicate that the **Co-(BimC$_3$F$_8$)$_3$** catalyst retained its molecular nature under the conditions used in our electrochemical experiments, and that the observed catalytic current is not related to the decomposition of the complex, or the deposition of a heterogeneous CoO$_x$ phase.

O$_2$ evolution during CPE with **Co-(BimC$_3$F$_8$)$_3$@FTO** was monitored by online GC. The peak current density was ~1.4 mA cm^{-2}, and O$_2$ production was 12.6-μmol per h, corresponding to ~78000 turnovers after 12 h, and a TOF of ~ 1.83 s^{-1}. The TOF has been calculated with the assumption every Co atom is accessible and catalytically active. This value compares favorably to other Co molecular catalysts for WOR (though exact benchmarking is difficult due to variation in screening conditions). Importantly, this TOF is approximately three orders of magnitude higher than could be expected from a typical CoO$_x$-type inorganic phase.[101] The Faradaic efficiency for oxygen production was close to 100%, indicating exclusive 4e$^-$ oxidation of water (**Figure 3.15**, in **Section 3.2.3.3**). No CO$_2$ production was detected.

A single-crystal X-ray structure of **Co-(BimC$_3$F$_8$)$_3$** was obtained (**Figure 3.2 C** and **Section 3.2.3.5**). The coordination sphere of Co comprizes the tripodal heterocyclic ligand, a chloride ligand, three free THF molecules, two disordered water molecules, and a chloride counterion. The fluorous side chains are disordered, and packed into discrete layers owing to their low polarizability and incompatibility with ordinary organic moieties (**Figure 3.21**, in **Section 3.2.3.5**). The Co(II) ion has a bipyramidal coordination

geometry, with the **(Bim)₃** motif locked in a fan-like conformation. The three benzimidazole nitrogens take the base plane positions, the remaining axial positions being occupied by the amine nitrogen and a chloride. The tetradentate mode of coordination, and the geometric parameters of the Co(II)-**(Bim)₃** moiety, especially the Co-N distances, are identical with **Co-(BimH)₃**.[97] Thus, the electronic properties of the metal centers are largely the same between **Co-(BimC₃F₈)₃** and the parent complex. This could be expected, as the fluorous side chains are separated from the metal site by multiple bonds.

The catalytic competence of surface-immobilized electrocatalysts is determined by a multitude of factors, including (but not limited to) the electronic and steric properties of the operational metal site, the nature of the interaction between the catalyst and the electrode surface,[84] and aggregation state/accessibility of the catalytic sites. The examination of single crystal structures of **Co-(Bim)₃** complexes suggests that they are spatially compact, conformationally rigid, and not intrinsically prone to stacking or aggregation. This is corroborated by their high solubility in practical organic solvents. Thus, it is reasonable to assume the operational catalysts in our experiments are single-site, monomeric species. Examination of the overpotentials for the phenyl-substituted variants of **Co-(Bim)₃** reveals a clear preference for electron-withdrawing substituents, which is consistent with the trend previously observed for phthalocyanines.[93]

The trend observed for the imidazole-alkylated **Co-(BimR)₃** variants is more subtle. While the coordination spheres and electronic properties of Co in these complexes are largely identical, it is readily apparent that bulkier/longer side chains have a dramatic and

salutary effect on both the WOR overpotential and the oxidative stability of the complexes. As all the structural variations in the **Co-(BimR)$_3$** series are introduced far away from the metal site, any variations in catalytic competence of the complexes would be due to differences in their steric encumbrance, conformational mobility, and nature of their interaction with the surface. The latter is ultimately the most important factor. Complexes with high surface affinity will necessarily be less conformationally mobile. The impact of any steric factors on the reactivity will also be amplified in tightly-tethered complexes, as the reacting site is locked by the surface and no longer has the freedom to twist and accommodate any incoming reactant species.

To gain insight into the nature of the interaction of the complexes with oxide surfaces, we obtained water contact angles for their thin films spread on oxidized Si (**Figure 3.4** and **Table 3.1**, in **Section 3.2.3.2**). The contact angle for **Co-(BimC$_3$F$_8$)$_3$**-coated substrate was 109 ° (**Figure 3.4 C**), much higher than that for **Co-(BimH)$_3$** (21 °, **Figure 3.4 A**), simple alkylated variants (57 °-64 °), or any of the phenyl-substituted variants (46 °-69 °). In comparison, the water contact angle for the pristine FTO slides is a moderately hydrophobic 38 °.
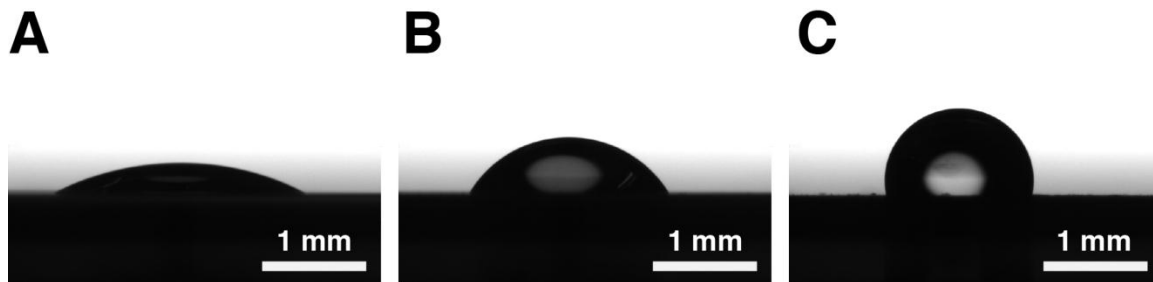
Figure 3.4 Water contact angles for Co complex films deposited on a Si wafer. (A) **Co-(BimH)$_3$**, 21 °; (B) **Co-(BimC$_{10}$H)$_3$**, 64 °; and (C) **Co-(BimC$_3$F$_8$)$_3$**, 109 °.

The lowest WOR overpotentials in the **Co-(BimR)₃** series (~0.39 V) are demonstrated by the most-hydrophobic **Co-(BimC₃F₈)₃**, as well as carboxylate- and phosphonate-linked **Co-(BimC₄CO₂K)₃**, **Co-(BimH)₂(BimC₂PA)** and **Co-(BimC₃F₈)₂(BimC₂PA)**. In contrast, the overpotentials for **Co-(BimC₆₊₂H)₃** and **Co-(BimC₄H)₃** are only marginally improved in comparison with the parent **Co-(BimH)₃**.

All the phosphonate- and carboxylate-linked complexes do eventually degrade in the course of prolonged CPE. However, the hydrophobic **Co-(BimC₁₀H)₃**, **Co-(BimC₆₊₂H)₃**, and **Co-(BimC₃F₈)₃** hang on to the surface through their sheer hydrophobicity, and appear oxidatively stable. The TOF for **Co-(BimC₆₊₂H)₃** variant is low, but the other two long-chain, hydrophobic catalysts are both resilient and active.

The WOR catalytic cycle involves multiple Co oxidation states, each having a distinct coordination geometry preference for the metal site.[86, 89] Any rearrangement in the coordination sphere of cobalt in **Co-(BimH/R)₃** would also involve the movement and conformational rearrangement of the side chains (if any). This process necessarily involves a partial desorption of the complex from the supporting surface, and possibly a partial dissociation of the ligand from the metal. Such a desorption process would be extremely challenging for the extremely hydrophobic fluorous side chains of **Co-(BimC₃F₈)₃**. The reorganization will be less arduous for **Co-(BimC₄H)₃**, and trivial for any of the phenyl-substituted variants. Ligands prone to dissociation and desorption will be subject to oxidation by the metal sites in their high oxidative state.[102] These considerations readily explain why **Co-(BimC₃F₈)₃** is the most performant catalyst in our series. It has by far the strongest affinity to the surface, as water is extremely prejudiced

against its fluorinated side chains (we postulate that the magnitude of this hydrophobic effect is higher than that of two or three oxide-phosphonate bonds). It never desorbs and the ligand pincers are locked firmly in place, which explains its oxidative stability. Furthermore, the catalytically relevant high oxidative state of the catalyst likely features a coordination environment that is very similar structurally to its ground state, which will facilitate the turnover.

3.2.3 Experimental Section

3.2.3.1 Synthesis of Catalysts

General notes

Flash chromatography was performed using Merck Kieselgel 60 (230-400 mesh) silica. Reactions requiring anhydrous conditions were performed under argon using standard Schlenk line techniques. Prior to use, THF was purified by refluxing over sodium in the presence of benzophenone until a persistent blue color appeared and then the solvent was collected via distillation. **(BimC$_4$CO$_2$K)$_3$** is commercially available and was purchased from Sigma-Aldrich.
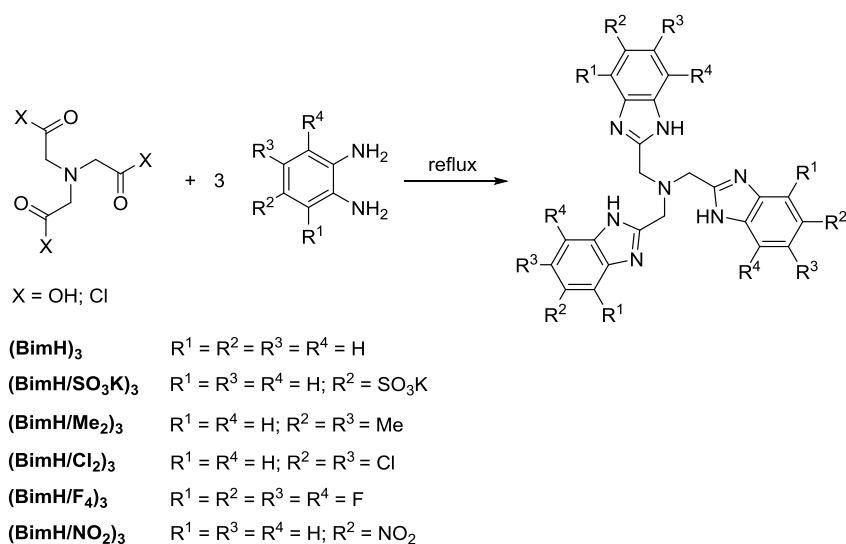
Scheme 3.1 Synthesis of **(BimH/R)₃**.

Tris(((1H-benzo[d]imidazol-2-yl)methyl)amine, (BimH)₃
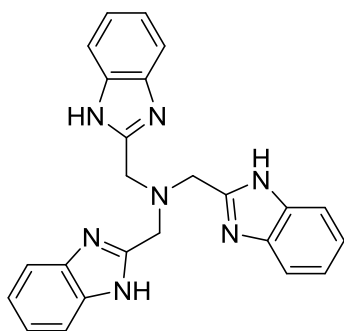
Prepared following a previously reported procedure.[103]

White solid. ^{1}H NMR (700 MHz, DMSO-d_6) δ 12.44 (s, 3H), 7.63 − 7.50 (m, 6H), 7.21 − 7.13 (m, 6H), 4.14 (s, 6H). ^{13}C NMR (176 MHz, DMSO-d_6) δ 152.14, 143.19, 134.17, 121.97, 121.14, 118.54, 111.24, 51.43. MS (ESI) *m/z*: [M + H]$^{+}$: 408.2.

Potassium   2,2',2''-(nitrilotris(methylene))tris(1H-benzo[d]imidazole-5-sulfonate), (BimH/SO₃K)₃
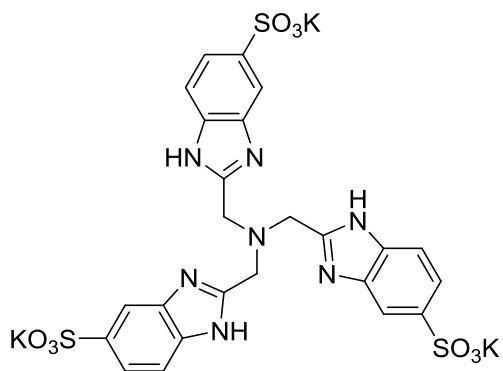
Prepared following a previously reported procedure.[104]

^{1}H NMR (700 MHz, D$_2$O) δ 7.88 (br, 3H), 7.48 (br, 3H), 7.24 (br, 3H), 3.95 (br, 6H).

^{13}C NMR (176 MHz, D$_2$O) δ 154.10, 138.66, 136.82, 119.99, 114.35, 112.73, 52.96.

Tris((5,6-dimethyl-1H-benzo[d]imidazol-2-yl)methyl)amine, (BimH/Me$_2$)$_3$
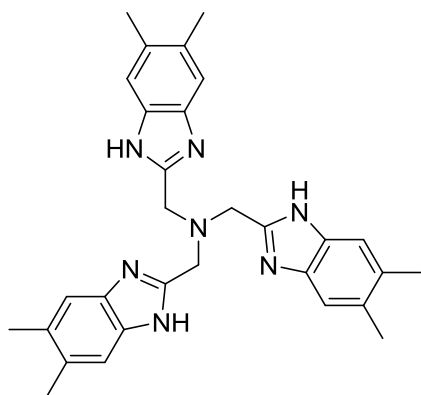
In a 100-mL flask, trinitriloacetic acid (63.67 mg, 0.3 mmol), 4,5-dimethyl-1,2-phenylenediamine (136.8 mg, 1 mmol) and 30 mL of ethylene glycol were added and the mixture was heated at 200 ^{o}C under inert atmosphere for 12 h. After cooling, the product was precipitated in 100 mL of ice-cooled water. The solid was filtered, washed with 50 mL of cool water and further purified by silica column using 3% methanol in DCM as an eluent to afford the product as a white powder. ^{1}H NMR (400 MHz, THF-d_8) δ 7.33 (s,

6H), 3.91 (s, 6H), 2.33 (s, 18H). ^{13}C NMR (101 MHz, THF-d_8) δ 151.81, 138.51, 131.22, 115.95, 52.07, 20.44. MS (ESI) *m/z*: [M + H]$^+$: 492.3.

Tris((5,6-dichloro-1H-benzo[d]imidazol-2-yl)methyl)amine, (BimH/Cl₂)₃
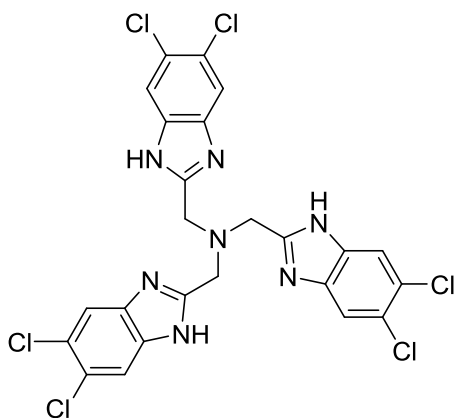
To a solution of 4,5-dichloro-1,2-phenylenediamine (88 mg, 0.5 mmol in 5 mL of anhydrous dioxane), 2,2,2-nitriloacetyl chloride (41 mg, 0.167 mmol in 7 mL of anhydrous dioxane) was added dropwise and the mixture was refluxed under a nitrogen atmosphere for 7 h. The solvent was then removed under reduced pressure and the residue was taken up in 4 N HCl (20 mL) and reflux for 6 h. After cooling, the acidic solution was basified with concentrated NH$_3$. The precipitate was filtered and washed with 50 mL of cool water. The product was purified by silica column using 3% methanol in DCM as eluent. ^{1}H NMR (400 MHz, THF-d_8) δ 7.73 (s, 6H), 4.13 (s, 6H). ^{13}C NMR (101 MHz, THF) δ 155.81, 126.36, 123.27, 117.06, 52.62. HRMS (ESI) calculated for [C$_{24}$H$_{16}$N$_7$Cl$_6$ + H]$^+$: 611.95983, found: 611.95911.

Tris((5-nitro-1H-benzo[d]imidazol-2-yl)methyl)amine, (BimH/NO₂)₃
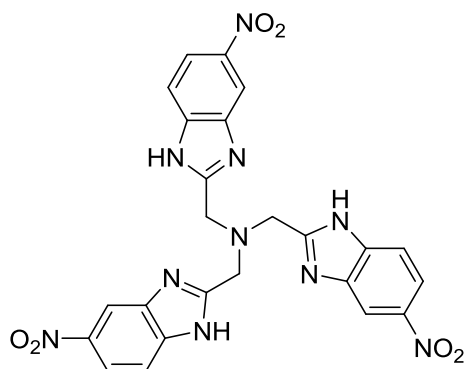
Prepared analogously to **(BimH/Cl₂)₃** through the reaction of 4-nitro-1,2-phenylenediamine with 2,2,2-nitriloacetyl chloride. The product was purified by silica column using 3% methanol in DCM as an eluent. ^{1}H NMR (400 MHz, DMSO-d_6) δ 8.36 (s, 3H), 8.04 (d, J = 8.7 Hz, 3H), 7.68 (d, J = 8.9 Hz, 3H), 4.28 (s, 6H). ^{13}C NMR (101 MHz, DMSO-d_6) δ 151.59, 136.19, 134.43, 132.07, 108.77, 105.90, 103.62, 45.10. HRMS (ESI) calculated for $[C_{24}H_{19}N_{10}O_6 + H]^+$: 543.14890, found: 543.14786.

Tris((4,5,6,7-tetrafluoro-1H-benzo[d]imidazol-2-yl)methyl)amine, (Bim/F₄)₃
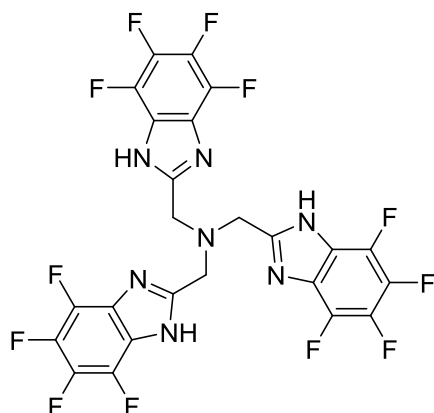
Prepared analogously to **(BimH/Cl₂)₃** through the reaction of 3,4,5,6-tetrafluoro-1,2-phenylenediamine with 2,2,2-nitriloacetyl chloride. ^{1}H NMR (400 MHz, Methanol-d_4) δ 4.02 (s, 6H). ^{13}C NMR (101 MHz, Methanol-d_4) δ 158.69 , 139.10 − 137.86 (m), 136.51

– 135.27 (m), 126.83 , 54.01 . ^{19}F NMR (377 MHz, Methanol-d_4) δ -159.65, -170.96.

HRMS (ESI) calculated for $[C_{24}H_9F_{12}N_7 + H]^+$: 624.08006, found: 624.08042.
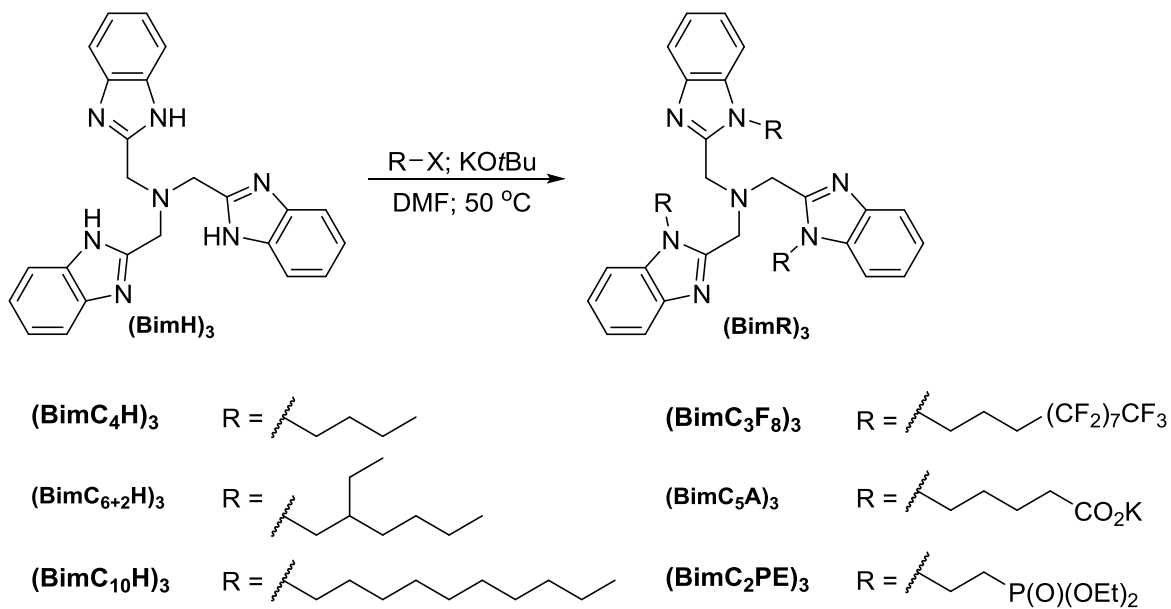
Scheme 3.2 Synthesis of **(BimR)$_3$**.

Tris((1-decyl-1H-benzo[d]imidazol-2-yl)methyl)amine, (BimC$_{10}$H)$_3$
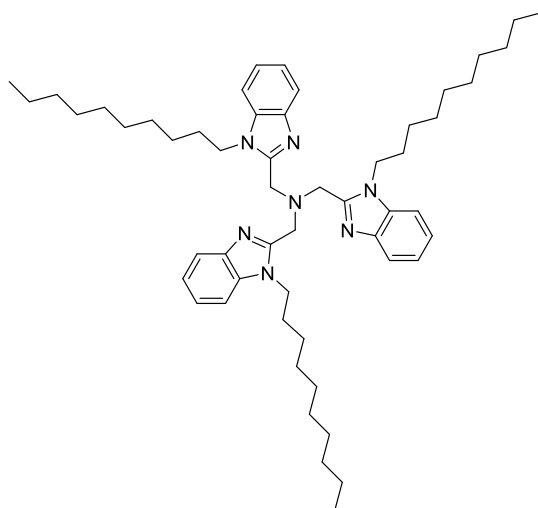
To a 100 mL schlenk flask protected with argon, **(BimH)₃** (1.08 g, 2.64 mmol), *t*BuOK (0.98 g, 8.7 mmol) and 25 mL of dry DMF were added and the resulting mixture was stirred at 50 °C for 15 min followed by the addition of 1-bromodecane (1.81 g, 8.2 mmol). The mixture was stirred overnight. After cooling, the mixture was transferred to a separatory funnel containing 50 mL of H_2O and 50 mL of DCM. The aqueous layer was extracted twice more with DCM (50 mL) and the combined organic phase was washed with water (50 mL × 2) and then dried over $MgSO_4$. The solvent was then evaporated under reduced pressure and the crude product was purified by silica-gel chromatography using 2.5% MeOH in DCM as an eluent. ^{1}H NMR (700 MHz, DMSO-d_6) δ 7.64 (d, *J* = 7.7 Hz, 3H), 7.42 (d, *J* = 7.9 Hz, 3H), 7.24 – 7.14 (m, *J* = 14.8, 7.2 Hz, 6H), 4.14 (s, 6H), 3.56 (t, *J* = 7.2 Hz, 6H), 1.29 – 1.11 (m, 24H), 1.10 – 1.01 (m, 12H), 0.91 – 0.82 (m, 9H), 0.81 – 0.74 (m, 6H), 0.47 – 0.39 (m, 6H). ^{13}C NMR (176 MHz, DMSO-d_6) δ 150.60, 142.05, 135.03, 122.39, 121.56, 119.00, 110.20, 49.25, 42.72, 31.27, 29.23, 28.84, 28.66, 28.64, 28.63, 25.64, 22.10, 13.97. HRMS (ESI) calculated for $[C_{54}H_{81}N_7 + H]^+$: 828.66262, found: 828.66100.

Tris((1-(2-ethylhexyl)-1H-benzo[d]imidazol-2-yl)methyl)amine, (BimC₆₊₂H)₃
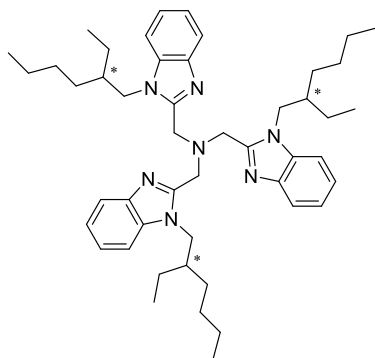
Prepared analogously to **(BimC₁₀H)₃** by alkylating **(BimH)₃** with 3-(bromomethyl)heptane. Mixtures of isomers. ^{1}H NMR (700 MHz, DMSO-d_6) δ 7.63 (d, J = 7.6 Hz, 3H), 7.36 (d, J = 4.9 Hz, 3H), 7.25 – 7.18 (m, 6H), 4.18 – 3.97 (m, 6H), 3.47 – 3.23 (m, 6H), 1.51 – 1.42 (m, 3H), 1.00 – 0.62 (m, 21H), 0.54 – 0.20 (m, 21H). ^{13}C NMR (176 MHz, DMSO-d_6) δ 151.11, 142.19, 135.16, 122.81, 121.95, 119.35, 110.71, 49.57, 47.19, 38.18, 29.56, 29.52, 29.48, 28.15, 28.05, 27.97, 23.14, 23.08, 23.04, 22.44, 22.41, 22.39, 13.91, 13.89, 13.86, 10.79, 10.76, 10.72. HRMS (ESI) calculated for [$C_{48}H_{69}N_7$ + H]$^+$: 744.56872, found: 744.56801.

Tris((1-butyl-1H-benzo[d]imidazol-2-yl)methyl)amine, (BimC₄H)₃
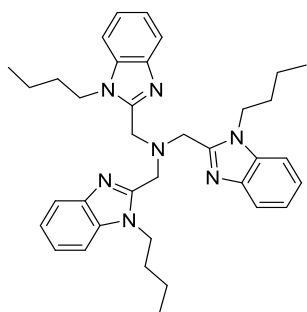
Prepared analogously to **(BimC₁₀H)₃** by alkylating **(BimH)₃** with 1-bromobutane. ^{1}H NMR (700 MHz, DMSO-d_6) δ 7.64 (d, J = 7.7 Hz, 3H), 7.45 (d, J = 7.9 Hz, 3H), 7.24 – 7.18 (m, 6H), 4.13 (s, 6H), 3.53 (t, J = 7.5 Hz, 6H), 1.06 – 1.01 (m, 6H), 0.50 – 0.39 (m, 15H). ^{13}C NMR (176 MHz, DMSO-d_6) δ 150.62, 142.06, 135.10, 122.50, 121.66, 119.03, 110.32, 49.23, 42.47, 31.39, 18.93, 13.53. MS (ESI) m/z: [M + H]$^+$: 576.2.

Tris((1-(4,4,5,5,6,6,7,7,8,8,9,9,10,10,11,11,11-heptadecafluoroundecyl)-1H-benzo[d]imidazol-2-yl)methyl)amine, (BimC₃F₈)₃
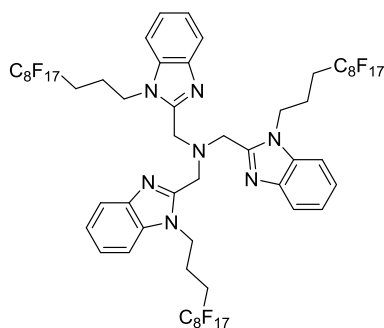
Prepared analogously to **(BimC$_{10}$H)$_3$** by alkylating **(BimH)$_3$** with 1*H*,1*H*,2*H*,2*H*,3*H*,3*H*-perfluoroundecyl iodide. Purified by recrystallization from a mixed solvent of ethyl acetate and hexane. ^{1}H NMR (700 MHz, Acetone-*d$_6$*) δ 7.71 (d, *J* = 7.6 Hz, 3H), 7.51 (d, *J* = 7.9 Hz, 3H), 7.29 − 7.22 (m, 6H), 4.38 (s, 6H), 3.95 (t, *J* = 7.2 Hz, 6H), 1.82 − 1.69 (m, 12H). ^{13}C NMR (176 MHz, Acetone-*d$_6$*) δ 152.11, 143.57, 136.14, 123.73, 122.92, 120.35, 110.76, 50.39, 42.80, 28.10 (t, *J* = 22.1 Hz), 21.45. ^{19}F NMR (377 MHz, Acetone-*d$_6$*) δ -81.70, -114.58, -122.38, -122.51, -123.33, -123.62, -126.79. MS (ESI) *m/z*: [M + H]$^+$: 1787.9; HRMS (ESI) calculated for [C$_{57}$H$_{36}$F$_{51}$N$_7$ + H]$^+$: 1788.22906, found: 1788.22392. The single crystal X-ray structure of **(BimC$_3$F$_8$)$_3$** was also obtained.
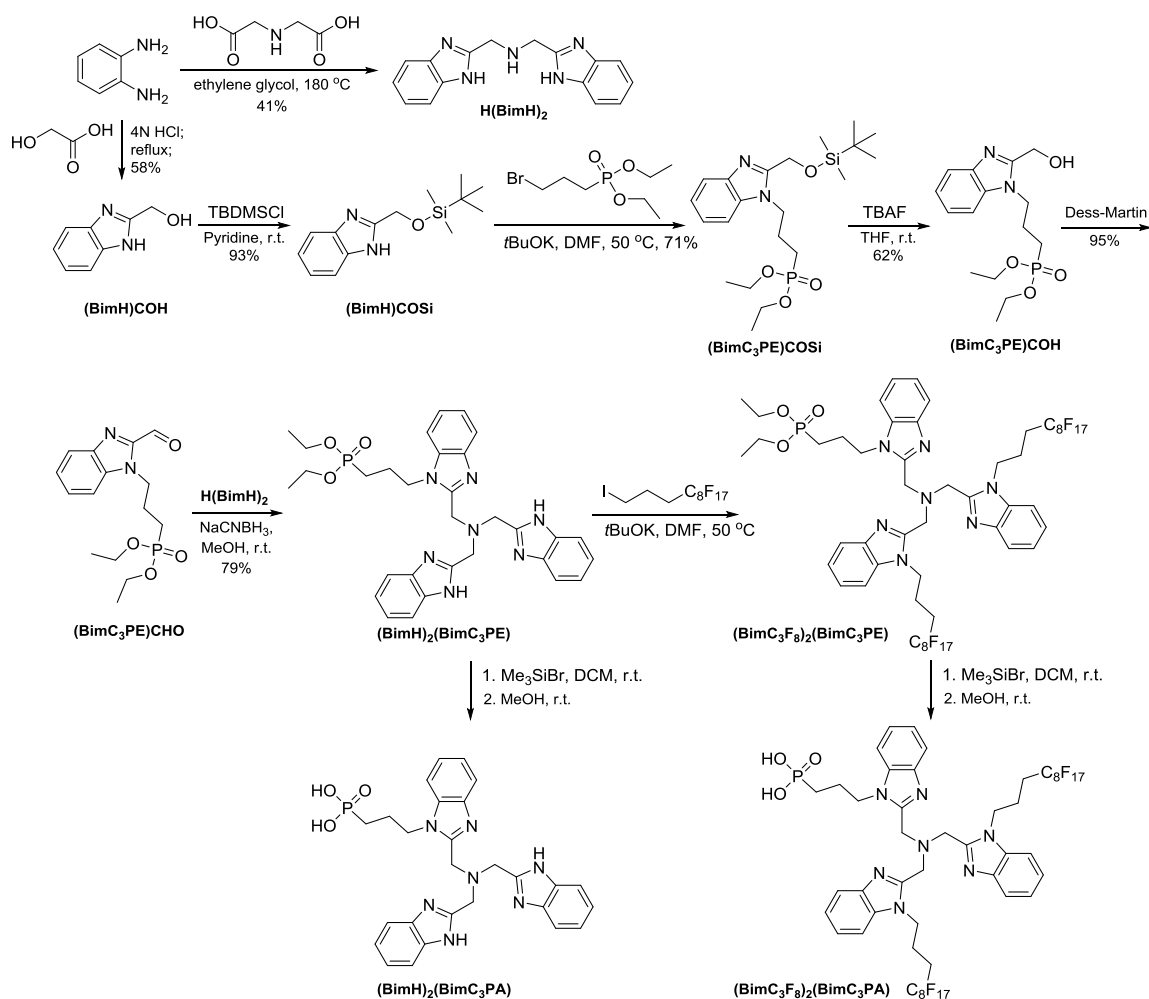
Scheme 3.3 Synthesis of **(BimR^1)$_2$(BimR^2)**.

(1H-benzo[d]imidazol-2-yl)methanol, (BimH)COH
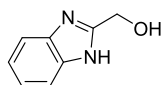
Prepared following a previously reported procedure.[105] White solid. ^{1}H NMR (400 MHz, Methanol-d$_4$) δ 7.56 − 7.50 (m, 2H), 7.24 − 7.18 (m, 2H), 4.83 (s, 2H). ^{13}C NMR (126 MHz, Methanol-d$_4$) δ 156.18, 123.41, 58.93. MS (ESI) m/z: [M + H]$^+$: 149.1.

2-(((Tert-butyldimethylsilyl)oxy)methyl)-1H-benzo[d]imidazole, (BimH)COSi
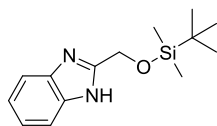
Prepared following a previously reported procedure.[106] White solid. ^{1}H NMR (500 MHz, Acetone-d$_6$) δ 7.62 – 7.43 (m, 2H), 7.16 (d, J = 6.4 Hz, 2H), 4.98 (s, 2H), 0.93 (s, 9H), 0.15 (s, 6H). ^{13}C NMR (126 MHz, Acetone-d$_6$) δ 122.85, 122.12, 119.74, 111.95, 60.74, 26.19, 18.90, -5.32. MS (ESI) m/z: [M + H]$^+$: 263.1.

Diethyl (3-(2-(((tert-butyldimethylsilyl)oxy)methyl)-1H-benzo[d]imidazol-1-yl)propyl)phosphonate, (BimC$_3$PE)COSi
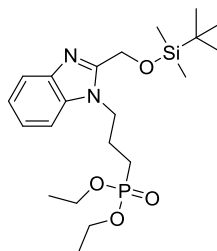
To a 100 mL schlenk flask protected with argon, **(BimH)COSi** (0.95 g, 3.45 mmol), *t*BuOK (0.46 g, 4.14 mmol) and 40 mL of dry DMF were added and the resulting mixture was stirred at 50 ^{o}C for 15 min followed by addition of diethyl (3-bromopropyl)phosphonate (1.07 g, 4.14 mmol). The mixture was stirred overnight. After cooling, the mixture was ransferred to a separatory funnel containing 100 mL of H$_2$O and 70 mL of DCM. The aqueous layer was extracted twice more with DCM (50 mL) and the combined organic phase was washed with water (70 mL $\times$2), and then dried over MgSO$_4$. The solvent was then evaporated under reduced pressure and the crude product was

purified by silica-gel chromatography using a mixed solvent of ethyl acetate and petroleum ether (3:4) as an eluent. White solid. Yield: 71%. ^{1}H NMR (400 MHz, Chloroform-*d*) δ 7.77 – 7.72 (m, 1H), 7.44 – 7.40 (m, 1H), 7.31 – 7.22 (m, 2H), 4.97 (s, 2H), 4.38 (t, *J* = 7.5 Hz, 2H), 4.15 – 4.01 (m, 4H), 2.26 – 2.11 (m, 2H), 1.84 – 1.71 (m, 2H), 1.30 (t, *J* = 7.1 Hz, 6H), 0.90 (s, 9H), 0.11 (s, 6H). ^{13}C NMR (101 MHz, Chloroform-*d*) δ 152.29 , 142.35 , 135.63 , 123.10 , 122.26 , 120.24 , 109.79 , 61.88 (d, *J* = 6.6 Hz), 59.66 , 44.24 (d, *J* = 16.9 Hz), 26.00 , 23.32 (d, *J* = 143.2 Hz), 23.20 (d, *J* = 4.9 Hz), 18.45 , 16.62 (d, *J* = 5.9 Hz), -5.22 . ^{31}P NMR (162 MHz, Chloroform-*d*) δ 30.49. HRMS (ESI) calculated for $[C_{21}H_{37}N_2O_4PSi + H]^+$: 441.23330, found: 441.23213.

Diethyl (3-(2-(hydroxymethyl)-1H-benzo[d]imidazol-1-yl)propyl)phosphonate, (BimC₃PE)COH
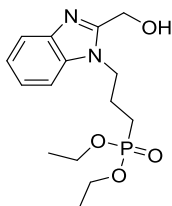
In a 10 mL flask, **(BimC₃PE)COSi** (0.68 g, 1.54 mmol) and TBAF (1 M in THF, 3.2 mL) were stirred at room temperature overnight. The solution was evaporated to dryness, dissolved in 100 mL ethyl acetate, washed with brine (20 mL × 3) and dried over MgSO₄. The solvent was then evaporated under reduced pressure and the product was obtained as a colorless oil. Yield: 62%. ^{1}H NMR (500 MHz, Chloroform-*d*) δ 7.65 – 7.61 (m, 1H), 7.34 – 7.30 (m, 1H), 7.24 – 7.16 (m, 2H), 5.36 (br, 1H), 4.85 (s, 2H), 4.30 (t, *J* = 7.5 Hz, 2H), 4.08 – 3.97 (m, 4H), 2.19 – 2.06 (m, 2H), 1.81 – 1.70 (m, 2H), 1.24 (t, *J* = 7.1 Hz, 6H). ^{13}C NMR (126 MHz, Chloroform-*d*) δ 153.79 (s), 141.39 (s), 134.93 (s), 123.10 (s),

122.43 (s), 119.36 (s), 109.78 (s), 61.93 (d, J = 6.5 Hz), 56.74 (s), 43.80 (d, J = 15.3 Hz), 22.95 (d, J = 4.8 Hz), 22.64 (d, J = 142.7 Hz), 16.44 (d, J = 5.9 Hz). ^{31}P NMR (243 MHz, Chloroform-d) δ 30.72. MS (ESI) m/z: [M + H]$^+$: 327.0; HRMS (ESI) calculated for [C$_{15}$H$_{23}$N$_2$O$_4$P + H]$^+$: 327.14682, found: 327.14613.

Diethyl (3-(2-formyl-1H-benzo[d]imidazol-1-yl)propyl)phosphonate, (BimC₃PE)CHO
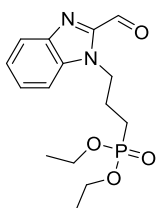
To a 25 mL flask, **(BimC₃PE)COH** (280 mg, 0.86 mmol) and 5 mL of dichloromethane were added and the mixture was put in an ice bath with Dess-Martin periodinane (424 mg, 1 mmol). After 2 h of stirring, the solution was diluted by adding 50 mL of dichloromethane and washed with saturated Na$_2$S$_2$O$_3$ and NaHCO$_3$ aqueous solution separately. The organic phase was then evaporated under reduced pressure and the product was obtained as a colorless oil. Yield: 95%. ^{1}H NMR (500 MHz, Chloroform-d) δ 10.03 (s, 1H), 7.85 (d, J = 8.3 Hz, 1H), 7.51 (d, J = 8.3 Hz, 1H), 7.44 – 7.40 (m, 1H), 7.35 – 7.31 (m, 1H), 4.68 – 4.59 (m, 2H), 4.09 – 3.95 (m, 4H), 2.15 – 2.03 (m, 2H), 1.76 – 1.65 (m, 2H), 1.23 (t, J = 7.1 Hz, 6H). ^{13}C NMR (126 MHz, Chloroform-d) δ 184.85 , 145.73 , 142.71 , 136.27 , 127.09 , 124.23 , 122.39 , 110.95 , 61.75 (d, J = 6.8 Hz), 44.57 (d, J = 16.4 Hz), 23.51 (d, J = 4.8 Hz), 22.67 (d, J = 143.1 Hz), 16.42 (d, J = 5.9 Hz). ^{31}P NMR (243 MHz, Chloroform-d) δ 30.40. MS (ESI) m/z: [M + H]$^+$:; HRMS (ESI) calculated for [C$_{15}$H$_{21}$N$_2$O$_4$P + H]$^+$: 325.13117, found: 325.13039.

Bis((1H-benzo[d]imidazol-2-yl)methyl)amine, H(BimH)₂
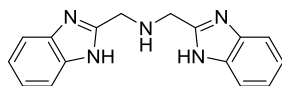

Prepared following a previously reported procedure.[107] White solid. ^{1}H NMR (700 MHz, Methanol-d_4) δ 7.59 – 7.48 (m, 4H), 7.28 – 7.16 (m, 4H), 4.11 (s, 4H). ^{13}C NMR (176 MHz, Methanol-d_4) δ 155.03, 123.51, 47.40. MS (ESI) *m/z*: $[M + H]^{+}$: 278.1.

Diethyl (3-(2-((bis((1H-benzo[d]imidazol-2-yl)methyl)amino)methyl)-1H-benzo[d]imidazol-1-yl)propyl)phosphonate, (BimH)₂(BimC₃PE)
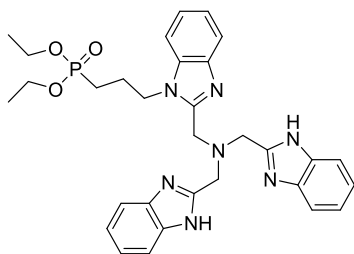
H(BimH)₂ (302 mg, 1.09 mmol) and **(BimC₃PE)CHO** (0.338 g, 1.04 mmol) were dissolved in dry methanol (10 mL). The solution was cooled to 0 ℃ and SOCl₂ (25 μL) was added followed by NaBH₃CN (342 mg, 5.45 mmol). The reaction mixture was stirred under N₂ for 10 h. The solution was evaporated to dryness and 50 mL of water was added. The aqueous solution was then extracted with CH₂Cl₂ (50 mL × 3) and the combined organic fractions were washed once with water (50 mL), and then dried over MgSO₄. The solvent was removed by rotary evaporation and the crude product was purified by silica-gel chromatography, using 2% MeOH in DCM as eluent. ^{1}H NMR (700 MHz, DMSO-d_6) δ 12.43 (br, 2H), 7.69 – 7.44 (m, 6H), 7.27 – 7.12 (m, 6H), 4.33 – 4.29 (m, 2H), 4.20 (s, 2H), 4.10 (s, 4H), 3.87 – 3.81 (m, 4H), 1.83 – 1.74 (m, 2H), 1.60 – 1.52

(m, 2H), 1.12 (t, J = 7.1 Hz, 6H). ^{13}C NMR (176 MHz, DMSO-d_6) δ 151.68 , 151.04 ,

143.17 , 142.01 , 135.39 , 134.20 , 122.30 , 122.05 , 121.55 , 121.17 , 119.09 , 118.59 ,

111.30 , 110.30 , 61.00 (d, J = 6.2 Hz), 51.14 , 50.03 , 43.05 (d, J = 18.1 Hz), 22.70 (d, J

= 4.0 Hz), 21.49 (d, J = 139.5 Hz), 16.24 (d, J = 5.7 Hz). ^{31}P NMR (243 MHz, DMSO-d_6)

δ 31.03. HRMS (ESI) calculated for $[C_{31}H_{36}N_7O_3P + H]^+$: 586.26900, found: 586.26768.

Diethyl   (3-(2-((bis((1-(1H,1H,2H,2H,3H,3H-perfluoroundecyl)-1H-benzo[d]imidazol-

2-yl)methyl)amino)methyl)-1H-benzo[d]imidazol-1-yl)propyl)phosphonate,

(BimC₃F₈)₂(BimC₃PE)
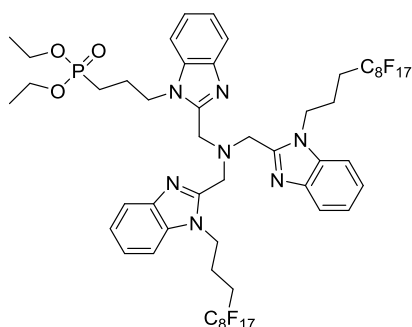
Prepared analogously to **(BimC₃F₈)₃** by alkylating **(BimH)₂(BimC₃PE)** with

1H,1H,2H,2H,3H,3H-perfluoroundecyl iodide. ^{1}H NMR (700 MHz, Methanol-d_4) δ 7.75

− 7.69 (m, 3H), 7.49 (d, J = 7.6 Hz, 1H), 7.46 (d, J = 7.6 Hz, 2H), 7.37 − 7.28 (m, 6H),

4.24 (s, 4H), 4.22 (s, 2H), 3.97 − 3.91 (m, 4H), 3.65 (t, J = 7.5 Hz, 4H), 3.57 (t, J = 7.6

Hz, 2H), 1.55 − 1.38 (m, 10H), 1.24 (t, J = 7.1 Hz, 6H), 0.92 − 0.85 (m, 2H). ^{13}C NMR

(176 MHz, Methanol-d_4) δ 151.93 , 151.90 , 142.65 , 142.55 , 136.06 , 136.04 , 125.15 ,

125.03 , 124.37 , 124.27 , 120.28 , 120.09 , 111.53 , 111.40 , 63.30 (d, J = 6.6 Hz), 50.53 ,

50.47 , 44.16 (d, J = 17.9 Hz), 43.14 , 28.26 (t, J = 22.2 Hz), 23.59 (d, J = 4.4 Hz), 22.18

(d, J = 142.8 Hz), 21.58 , 16.70 (d, J = 5.9 Hz). ^{31}P NMR (243 MHz, Methanol-d_4) δ

30.99. ^{19}F NMR (377 MHz, Methanol-d_4) δ -82.39, -115.08, -122.80, -122.94, -123.77, -123.92, -127.32. MS (ESI) *m/z*: [M + H]$^{+}$: 1506.2; HRMS (ESI) calculated for [C$_{53}$H$_{46}$F$_{34}$N$_7$O$_3$P + H]$^{+}$: 1506.29296, found: 1506.28940.

(3-(2-((Bis((1H-benzo[d]imidazol-2-yl)methyl)amino)methyl)-1H-benzo[d]imidazol-1-yl)propyl)phosphonic acid, (BimH)₂(BimC₃PA)
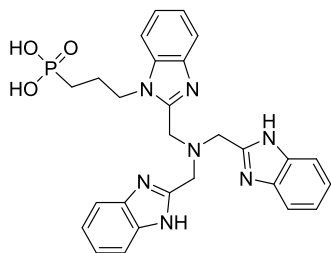
To a flask under argon atmosphere, **(BimH)₂(BimC₃PE)** (41 mg, 0.07 mmol) and DCM (10 mL) were added. Then SiMe$_3$Br (86 mg, 0.56 mmol) was slowly added and the mixture was stirred at room temperature for 2 d. The solvents were evaporated under reduced pressure; MeOH (20 mL) was added and stirred for 2 h and then evaporated under reduced pressure. The product was dried under a vacuum to yield **(BimH)₂(BimC₃PA)** with sufficient purity. ^{1}H NMR (700 MHz, Methanol-d_4) δ 8.00 − 7.88 (m, 2H), 7.85 − 7.80 (m, 4H), 7.65 − 7.57 (m, 6H), 4.93 − 4.73 (m, 8H), 2.31 − 2.24 (m, 2H), 2.06 − 1.99 (m, 2H). ^{13}C NMR (176 MHz, Methanol-d_4) δ 148.85 , 148.27 , 132.52 , 131.08 , 130.53 , 126.85 , 126.60 , 126.49 , 114.27 , 113.76 , 112.65 , 50.62 , 50.10 , 45.46 (d, *J* = 10.0 Hz), 23.22 (d, *J* = 138.4 Hz), 22.92 (d, *J* = 3.8 Hz). ^{31}P NMR (243 MHz, Methanol-d_4) δ 27.45. HRMS (ESI) calculated for [C$_{27}$H$_{28}$N$_7$O$_3$P + H]$^{+}$: 530.20640, found: 530.20528.

(3-(2-((Bis((1-(1H,1H,2H,2H,3H,3H-perfluoroundecyl)-1H-benzo[d]imidazol-2-

yl)methyl)amino)methyl)-1H-benzo[d]imidazol-1-yl)propyl)phosphonic   acid,

(BimC₃F₈)₂(BimC₃PA)
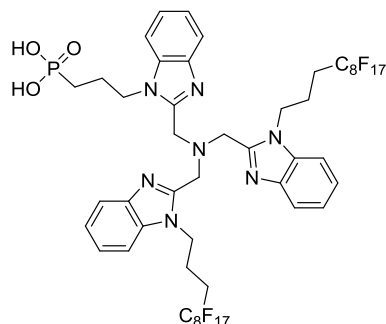
Prepared analogously to **(BimH)₂(BimC₃PA)** by treating **(BimC₃F₈)₂ (BimC₃PE)** with

SiMe₃Br. ¹H NMR (700 MHz, Methanol-d_4) δ 8.04 – 7.91 (m, 6H), 7.72 – 7.59 (m, 6H),

5.09 (s, 4H), 5.03 (s, 2H), 4.82 – 4.73 (m, 6H), 2.64 – 2.51 (m, 4H), 2.34 – 2.17 (m, 6H),

2.08 – 1.99 (m, 2H). ³¹P NMR (162 MHz, Methanol-d_4) δ 27.96. ¹⁹F NMR (377 MHz,

Methanol-d_4) δ -82.40, -115.18, -122.67, -122.93, -123.78, -124.28, -127.33. HRMS (ESI)

calculated for $[C_{49}H_{38}F_{34}N_7O_3P + H]^+$: 1450.23036, found: 1450.22631.
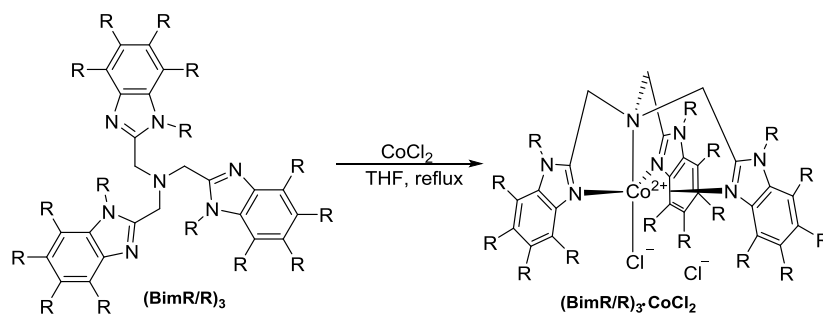
Scheme 3.4 Synthesis of Co(II) complexes.

Co-(BimC₃F₈)₃
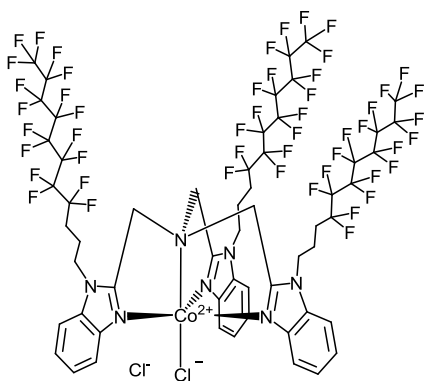
To a 50 mL flask, **(BimC₃F₈)₃** (179 mg, 0.1 mmol), anhydrous CoCl₂ (14 mg, 0.11 mmol) and 20 mL of THF were added and the resulting solution was stirred and refluxed for 2 h. After cooling, the solvent was evaporated under reduced pressure and the resulting solid was washed with water (5 ml $\times$ 3) to afford the product as a purple solid. MS (ESI) m/z: [**(BimC₃F₈)₃** + Co²⁺ + CF₃COO⁻]⁺:1958.8; [**(BimC₃F₈)₃** + Co²⁺ + Cl⁻]⁺: 1881.8. (0.1% CF₃COOH was added in the eluent of LCMS) Calcd. for C₅₇H₄₂Cl₂CoF₅₁N₇O₃ ([**Co(BimC₃F₈)₃** 3H₂O): C, 34.72; H, 2.15; N, 4.97. Found: C, 34.57; H, 2.38; N, 5.11. The single crystal X-ray structure of **Co-(BimC₃F₈)₃** was also obtained (for details, see **Section 3.2.3.5**). The other complexes were prepared analogously to **Co-(BimC₃F₈)₃** by refluxing the ligands with anhydrous CoCl₂ in THF.

3.2.3.2 Preparation of Working Electrodes

We selected fluorine-doped tin-oxide- (FTO) coated glass substrates to prepare catalyst-functionalized electrodes. The FTO conductive layer is transparent, oxidatively stable and tolerant to mechanical abrasion. FTO glass (15 ohm/sq, Hartford Glass) substrates (size: 1 cm $\times$ 3 cm) were cleaned by consecutive 30-min sonication in

detergent, deionized water, acetone and ethanol. After cleaning, the electrodes were dried at 120 ℃ for at least 1 h.

To prepare the working electrodes, planar FTO substrates were loaded with the molecular species by drop casting. A drop of a solution with a known concentration was deposited onto the surface of the electrode covering $1cm^2$. A 10^{-3} M solution of Co-complex in methanol was used to prepare stock solutions (total volume, 1 ml). Then, 10 μl of the stock solution was deposited onto the FTO electrodes to obtain different loadings.

Table 3.1 Contact angle measurement of surface-modified electrodes with 5×10^{-10} mol cm^{-2} loading of different Co-trisbenzimidazoles.

	Sample	Contact angle (^{o}) ± 1
0	FTO blank electrode	38
1	**Co–(BimH)$_3$**	21
2	**Co–(BimH/Me$_2$)$_3$**	51
3	**Co–(BimH/Cl$_2$)$_3$**	49
4	**Co–(BimH/NO$_2$)$_3$**	46
5	**Co–(BimH/F$_4$)$_3$**	69
6	**Co–(BimC$_4$H)$_3$**	57
7	**Co–(BimC$_{6+2}$H)$_3$**	62
8	**Co–(BimC$_{10}$H)$_3$**	64
9	**Co–(BimC$_3$F$_8$)$_3$**	109
10	**Co–(BimH)$_2$ (BimC$_3$PE)**	31
11	**Co–(BimH)$_2$ (BimC$_3$PA)**	16
12	**Co–(BimC$_3$F$_8$)$_2$ (BimC$_3$PE)**	87
13	**Co–(BimC$_3$F$_8$)$_2$ (BimC$_3$PA)**	52

| 14 | Co–(BimC$_4$CO$_2$K)$_3$ | 23 |
| 15 | Co–(BimSO$_3$K)$_3$ | 16 |

3.2.3.3 Electrochemical Data
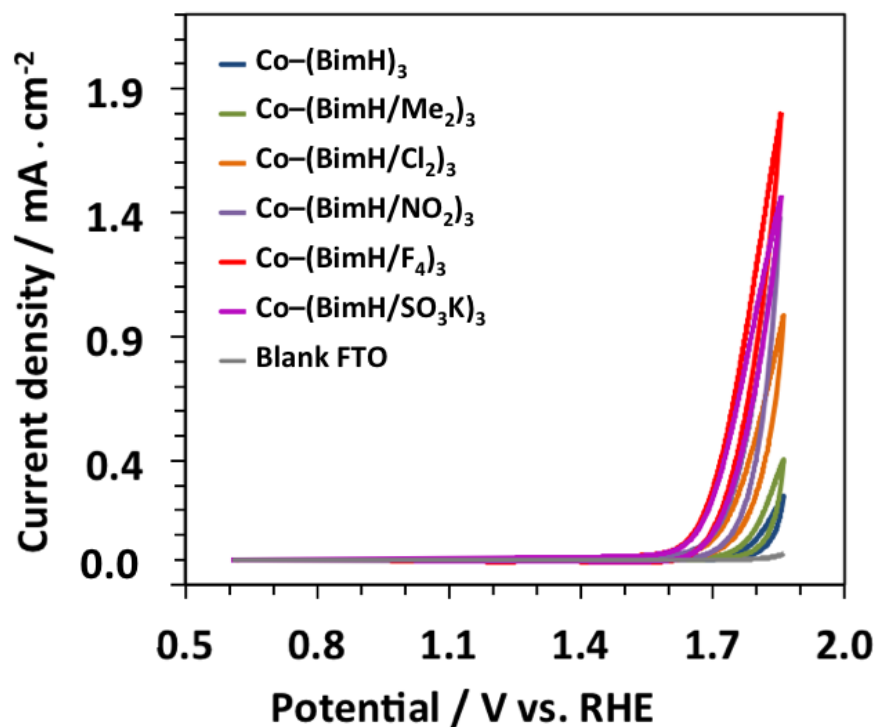
Figure 3.5 Cyclic voltammogram of trisbenzimidazole Co-complexes with benzene-ring-substituted variants **(BimH/R)$_3$**, in 0.1 M potassium phosphate buffer, pH 7 and 50 mV s^{-1} scan rate. Loading: 5×10^{-10} mol cm^{-2}.
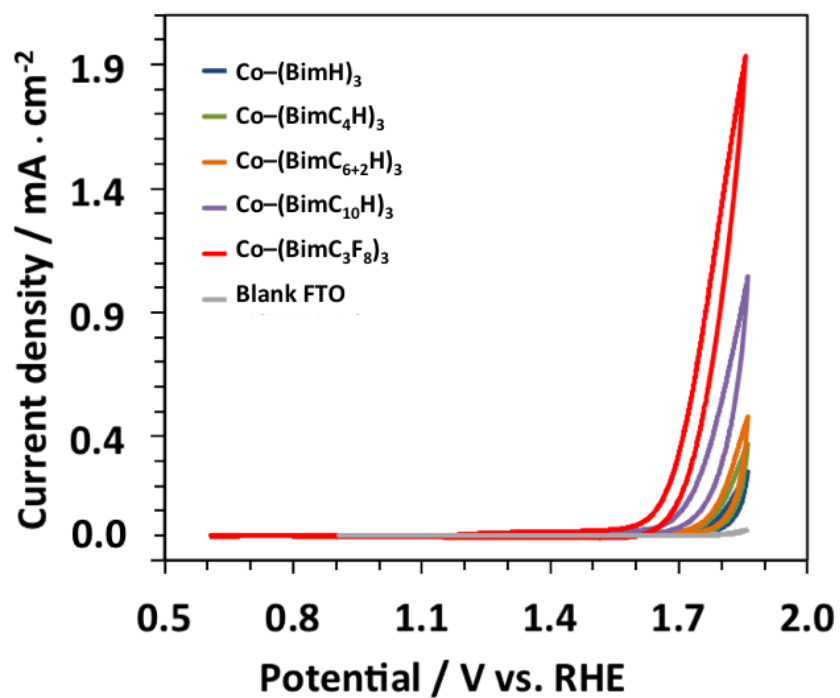
Figure 3.6 Cyclic voltammogram of Co-complexes with N-alkylated trisbenzimidazole derivatives **(BimR)$_3$**, at pH 7 in 0.1 M potassium phosphate buffer and 50 mV s^{-1} scan rate. Loading: 5×10^{-10} mol cm^{-2}.
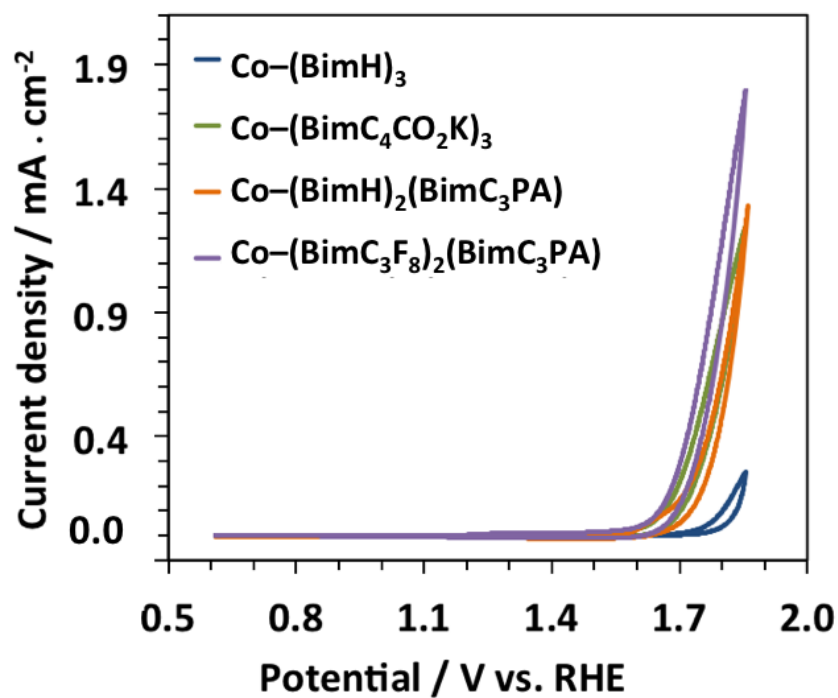
Figure 3.7 Cyclic voltammogram of Co-complexes with N-alkylated trisbenzimidazole derivatives **(BimR)₃** with carboxylic and phosphonic acids, in 0.1 M potassium phosphate buffer, pH 7 and 50 mV s^{-1} scan rate. Loading: 5×10^{-10} mol cm^{-2}.
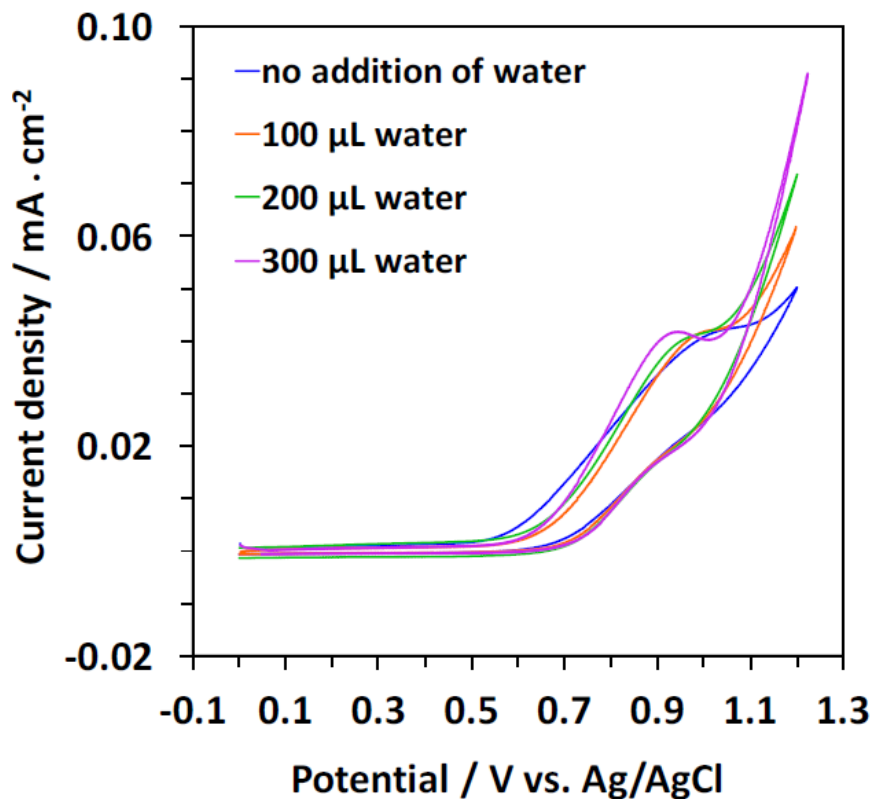
Figure 3.8 Cyclic voltammograms for 0.5 mM **Co-(BimC$_3$F$_8$)$_3$** in DMF (10 mL). No water added (blue curve) and 100-300 µL of water added (orange, green and purple curves). CVs were collected in a three-compartment cell at 100 mV/s with 0.1 M NBu$_4$PF$_6$ as supporting electrolyte, 3 mm diameter glassy carbon working electrode, Pt counterelectrode, and Ag/AgCl reference electrode. The midpoint potential for the redox event before the onset of the catalytic wave is 0.86 V vs Ag/AgCl.
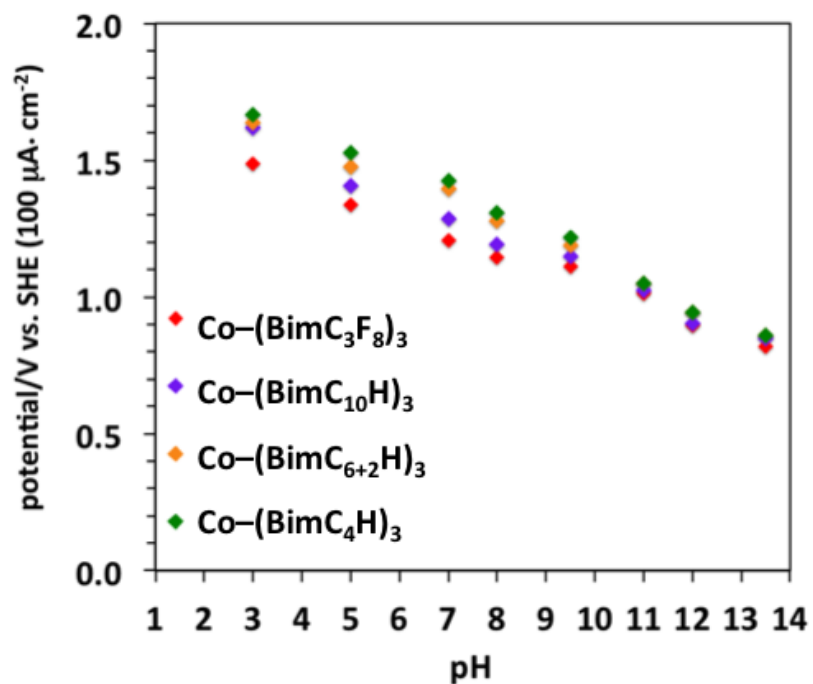
Figure 3.9 Dependence of the WOR onset potential (measured at 100 $\mu A \cdot cm^{-2}$) on the pH for Co complexes with N-alkylated trisbenzimidazole derivatives **(BimR)$_3$** (electrolyte concentration 0.1 M, in the presence of phosphate; $\Gamma = 5.0 \times 10^{-10}$ mol·cm^{-2}; scan rate 50 mV/s). Slope is $-(60\text{-}75)$ mV per pH unit. Electrolyte concentration: 0.1 M. Scan rate 50 mV/s.
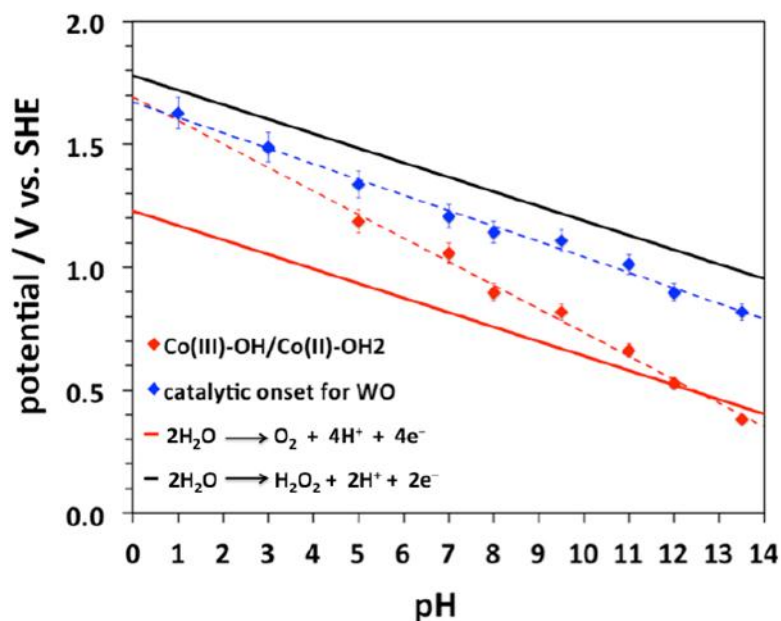
Figure 3.10 Blue diamonds ◆: Dependence of the WOR onset potential (measured at 100 $\mu A \cdot cm^{-2}$) on the pH for **Co-(BimC₃F₈)₃** (electrolyte concentration 0.1 M, in the presence of phosphate; $\Gamma = 5.0 \times 10^{-10}$ mol·cm^{-2}; scan rate 50 mV/s). Slope is −63 mV per pH unit. Red diamonds ◆: Dependence of the redox couple midpoint potential on the pH, slope −95 mV per pH unit. Red line: thermodynamic potential for water oxidation to oxygen via $4H^+/4e^-$ transfer. **Black line**: thermodynamic potential for water oxidation to H_2O_2 via $2H^+/2e^-$ transfer.
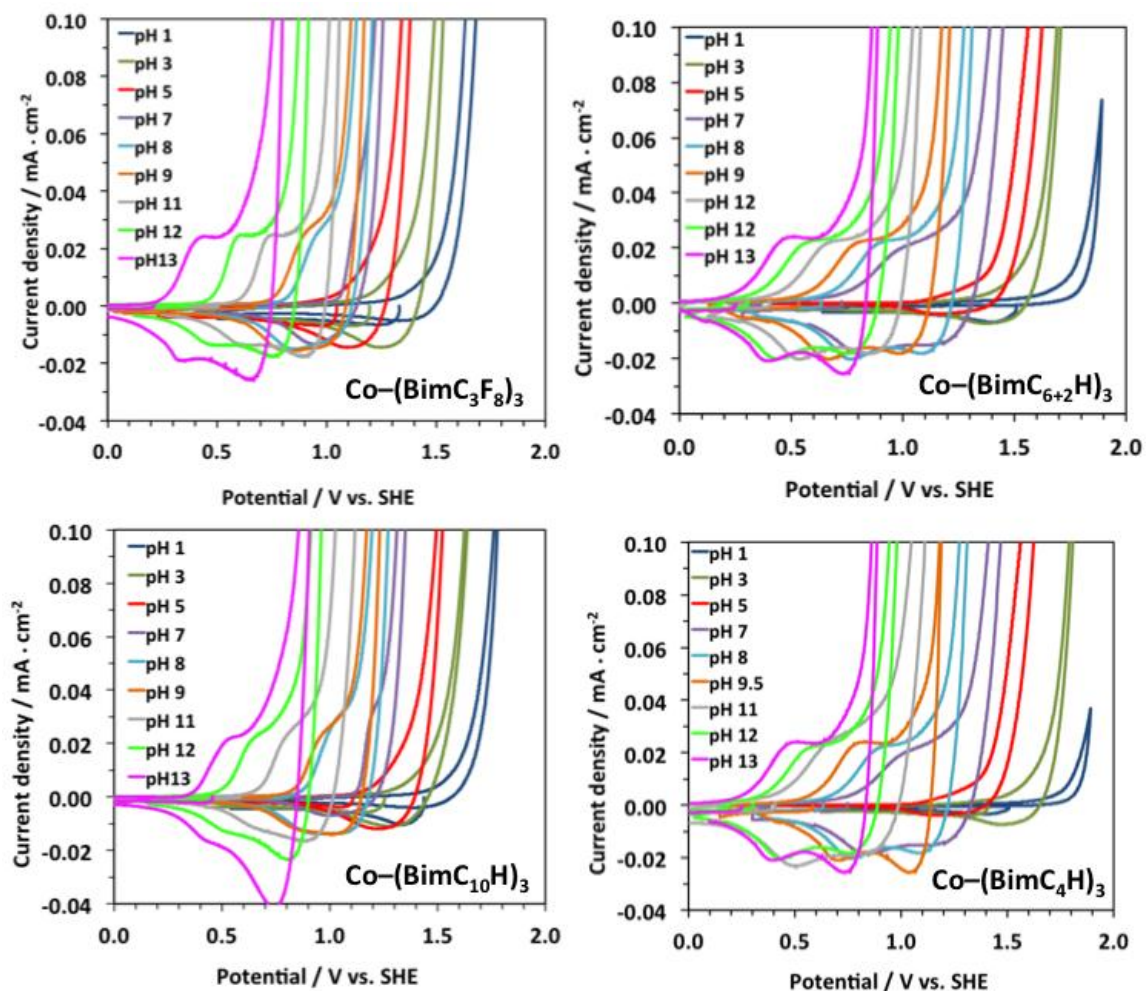
Figure 3.11 Magnified view of the CVs collected for Co complexes with N-alkylated trisbenzimidazole derivatives **(BimR)$_3$** (Γ = 5.0 $\times$ 10^{-10} mol·cm^{-2}) at different pH in the range 1-13 (0.1 M electrolyte concentration, scan rate 50 mV/s).
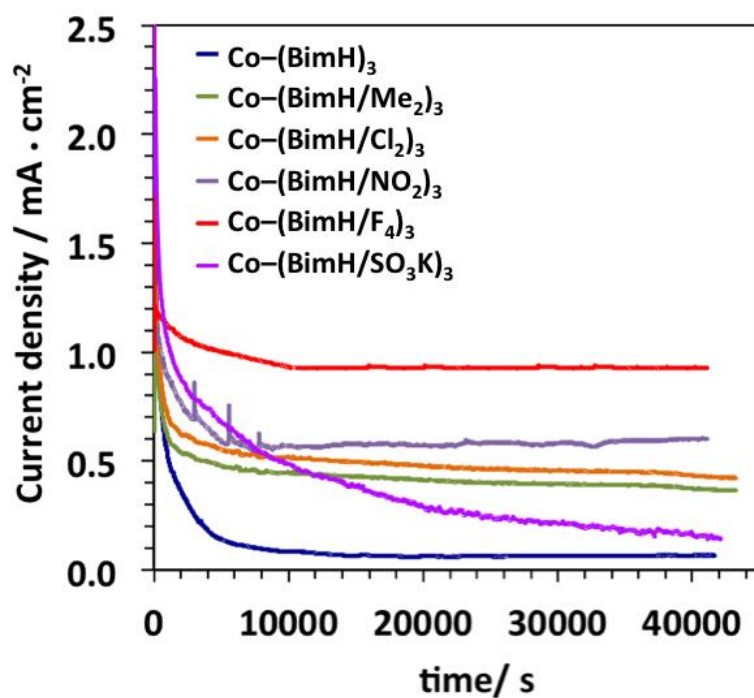
Figure 3.12 Controlled potential electrolysis of trisbenzimidazole Co-complexes with benzene-ring-substituted variants **(BimH/R)$_3$**, at 1.91 V vs. RHE, in 0.1 M potassium phosphate buffer, pH 7. Loading: 2×10^{-9} mol cm^{-2}.
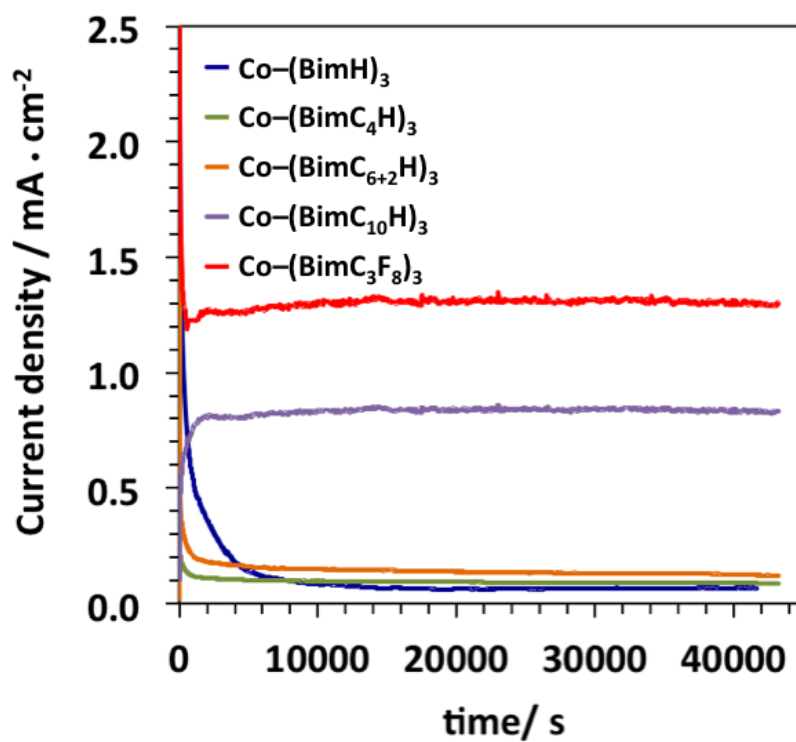
Figure 3.13 Controlled potential electrolysis of Co-complexes with N-alkylated trisbenzimidazole derivatives **(BimR)$_3$,** at 1.91 V vs. RHE, in 0.1 M potassium phosphate buffer, pH 7. Loading: 2×10^{-9} mol cm^{-2}.
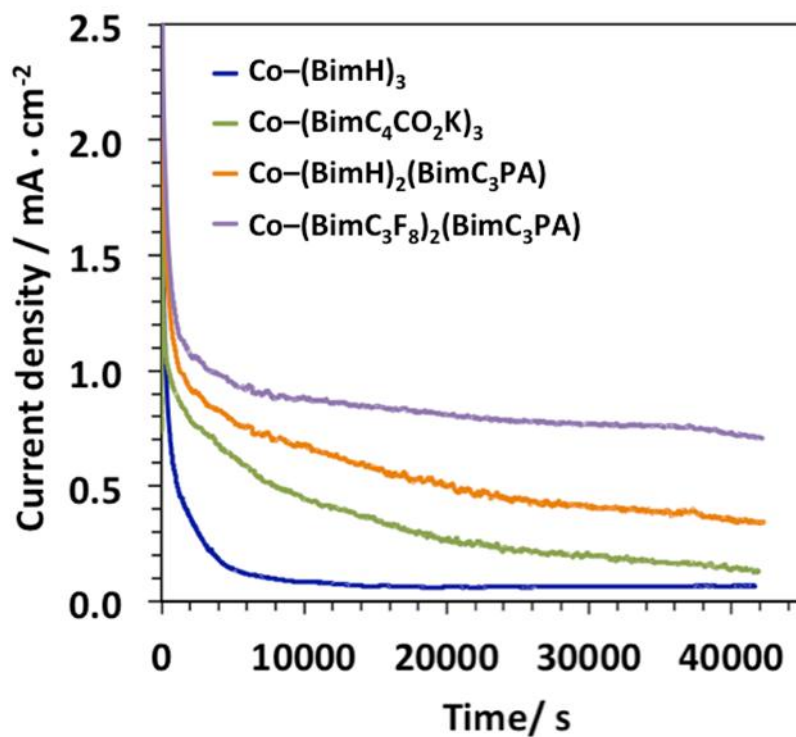
Figure 3.14 Controlled potential electrolysis of Co-complexes with N-alkylated trisbenzimidazole derivatives **(BimR)$_3$** with carboxylic and phosphonic acids, at 1.91 V vs. RHE, in 0.1 M potassium phosphate buffer, pH 7. Loading: 2×10^{-9} mol cm^{-2}.
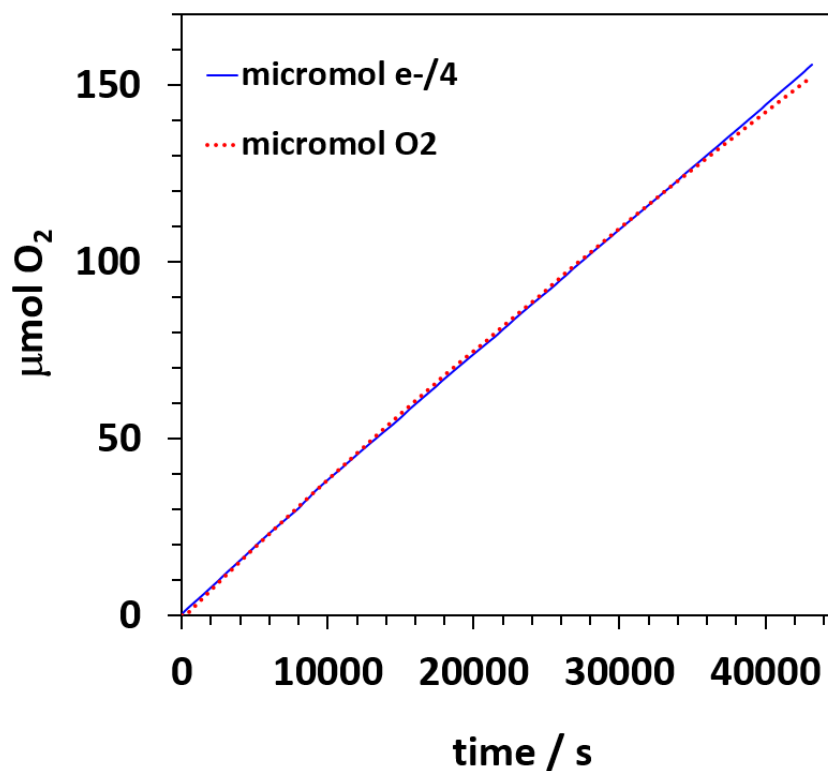
Figure 3.15 Oxygen evolution during controlled potential electrolysis **Co-(BimC$_3$F$_8$)$_3$** at 1.91 V vs. RHE, in 0.1 M potassium phosphate buffer, pH 7. Loading: 2×10^{-9} mol cm^{-2}.

Table 3.2 Onset potential and TOF obtained with electrodes modified with 0.5 - 2 $\times$ 10^{-9} mol cm^{-2} loading of different Co-trisbenzimidazoles.

	Sample	Onset potential (V vs. RHE) [a]	Current density (mA cm^{-2})[b]	TOF (s^{-1}) [c]
1	**Co–(BimH)$_3$**	1.86		-
2	**Co–(BimH/Me$_2$)$_3$**	1.74	0.37	0.48
3	**Co–(BimH/Cl$_2$)$_3$**	1.65	0.42	0.54
4	**Co–(BimH/NO$_2$)$_3$**	1.63	0.63	0.82
5	**Co–(BimH/F$_4$)$_3$**	1.62	0.94	1.22
6	**Co–(BimH/SO$_3$K)$_3$**	1.61		-

7	Co–(BimC$_4$H)$_3$	1.83	0.09	0.12
8	Co–(BimC$_{6+2}$H)$_3$	1.81	0.13	0.16
9	Co–(BimC$_{10}$H)$_3$	1.69	0.86	1.11
10	Co–(BimC$_3$F$_8$)$_3$	1.61	1.42	1.83[d]
11	Co–(BimH)$_2$ (BimC$_3$PA)	1.62		-
12	Co–(BimC$_3$F$_8$)$_2$ (BimC$_3$PA)	1.62		-
13	Co–(BimC$_4$CO$_2$K)$_3$	1.62		-

[a] Onset potential: potential when current density reaches 100 Microamperes per cm^2 during a cyclic voltammogram at 1 mV/s

[b] steady current reached during the cpe experiment at 1.91 V vs. RHE (see **Figure 3.12** and **Figure 3.13**)

[c] TOF: calculated from the steady current reached during the cpe experiment at 1.91 V vs. RHE

[d] TOF: calculated from the oxygen measurement during the cpe experiment at 1.91 V vs. RHE (see **Figure 3.15**).
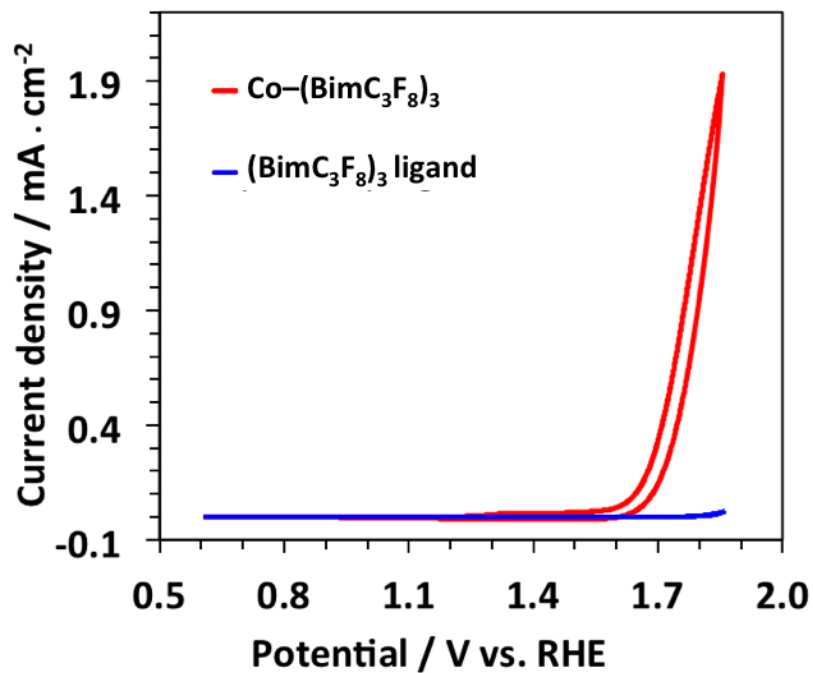
Figure 3.16 Cyclic voltammograms of **Co-(BimC$_3$F$_8$)$_3$** and **(BimC$_3$F$_8$)$_3$** ligand (Γ = 5 $\times 10^{-10}$ mol cm^{-2}) at pH 7 (0.1-M potassium phosphate buffer and 50 mV s^{-1} scan rate).
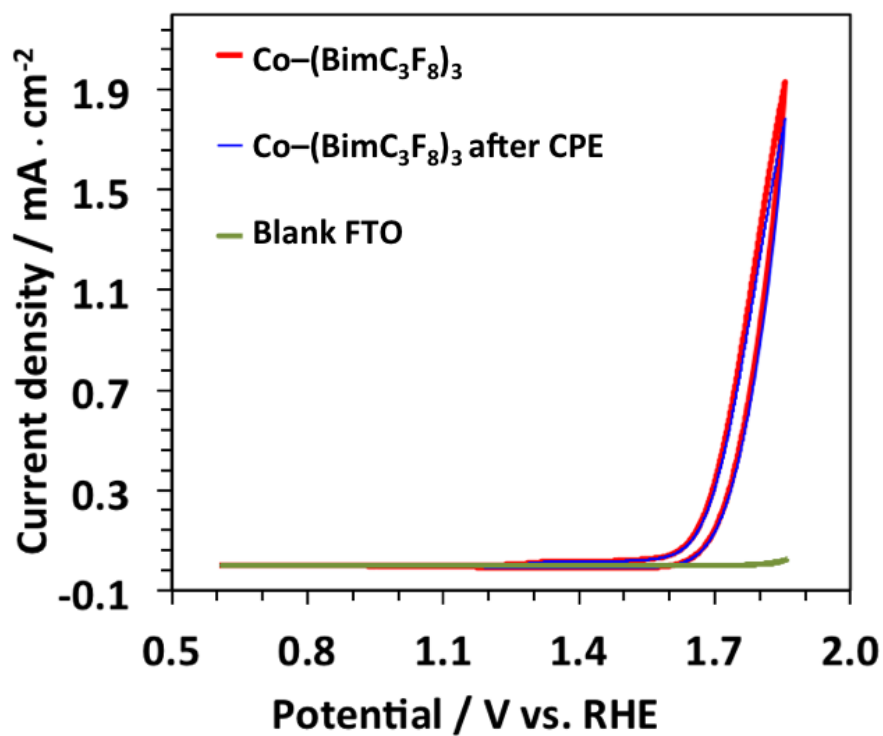
Figure 3.17 Cyclic voltammograms of **Co-(BimC$_3$F$_8$)$_3$** ($\Gamma = 5.0 \times 10^{-10}$ mol cm^{-2}) before and after CPE for 12 h at 1.85 V vs. RHE at pH 7 (0.1 M potassium phosphate buffer).
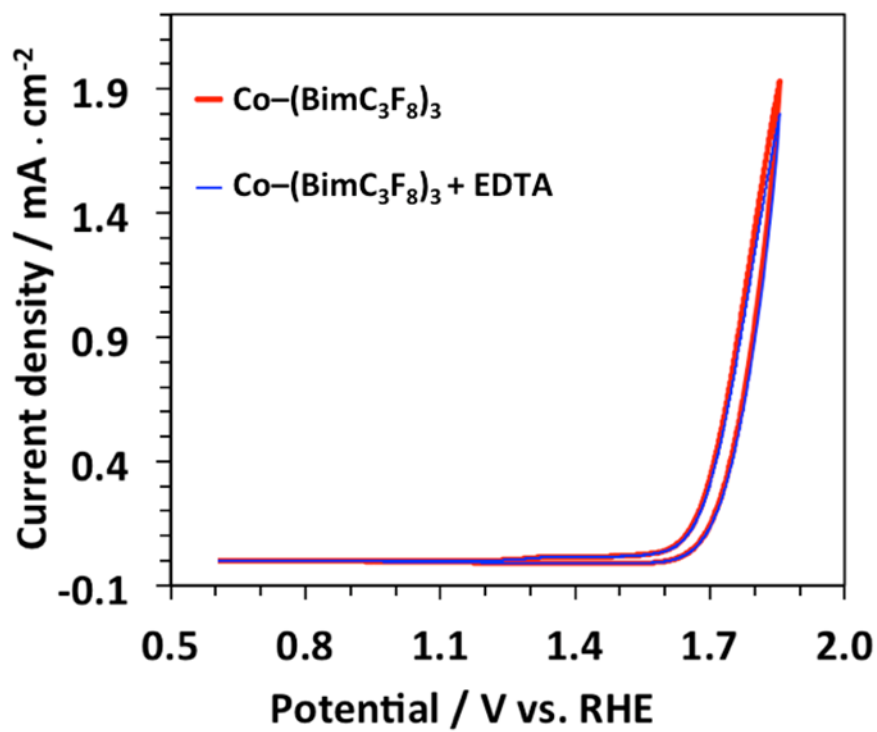
Figure 3.18 Cyclic voltammograms of **Co-(BimC₃F₈)₃** (Γ = 5.0 × 10^{-10} mol cm^{-2}) after addition of EDTA 0.05mM (0.1 M potassium phosphate buffer pH 7 and scan rate 50 mV/s).

3.2.3.4 Spectroscopic Characterization of the Co-complexes after electrochemistry
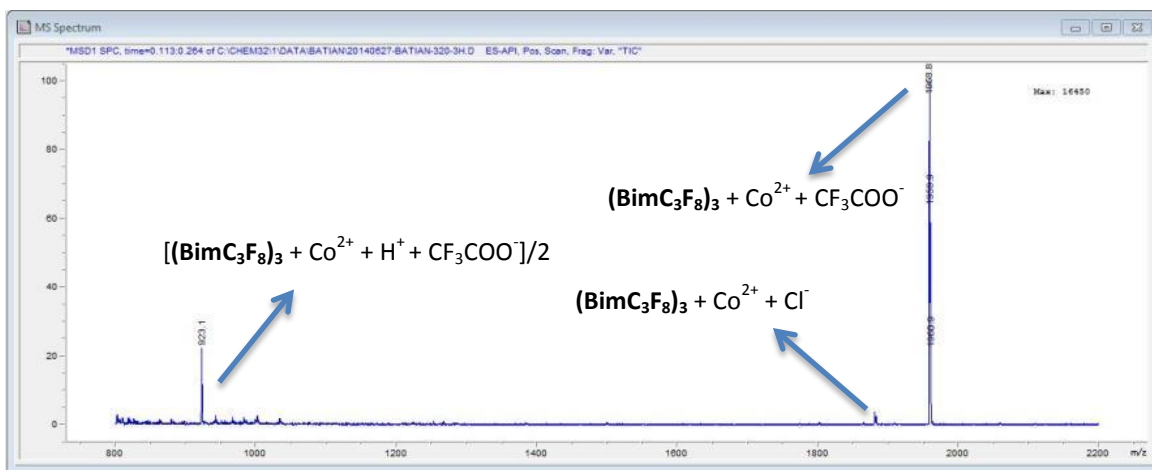
Figure 3.19 Mass spectra of **Co-(BimC₃F₈)₃** after controlled potential electrolysis at 1.91 V vs. RHE for 12 h at pH 7 (0.1-M potassium phosphate buffer).
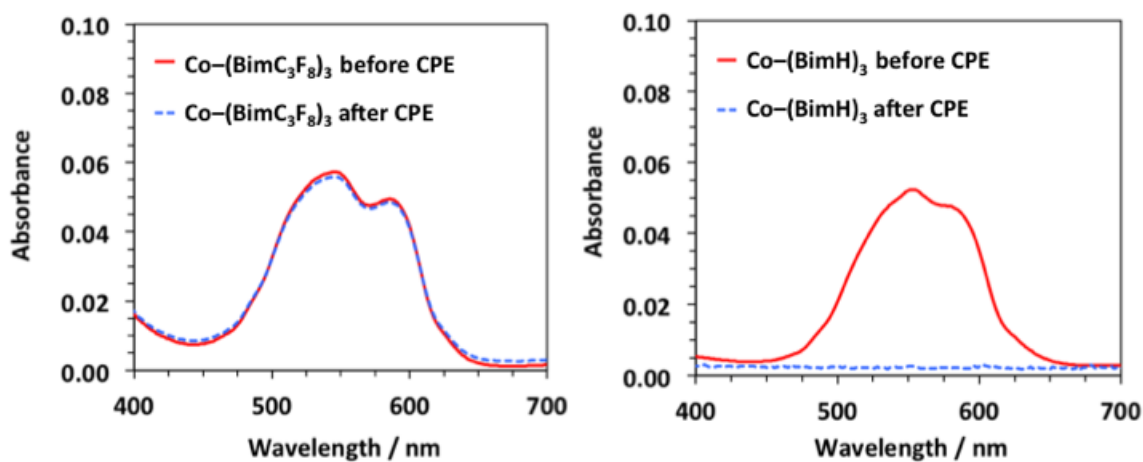
Figure 3.20 UV-Vis absorption spectra of **Co-(BimC₃F₈)₃** (left) and **Co-(BimH)₃** (right) in methanol (2×10^{-5} M), before and after controlled potential electrolysis at 1.91 V vs. RHE for 12 h (0.1 M potassium phosphate buffer, pH 7).

3.2.3.5 X-Ray Structure Determination

[CoCl(C$_{57}$H$_{36}$F$_{51}$N$_7$)]Cl (C$_4$H$_8$O)$_3$ (H$_2$O)$_2$
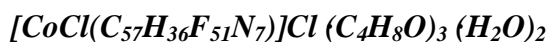
Crystals grew as a six-sided plates showing a strong dichroism, appearing pink or deep purple depending on orientation. X-ray intensity data from were collected at 200(2) K using a Bruker D8 QUEST diffractometer equipped with a PHOTON 100 CMOS area detector and an Incoatec microfocus source (Mo K radiation, = 0.71073 Å). Flash-cooling to lower temperatures resulted in visible cracking of the crystal. Some minor fractures were observed even at 200 K. The material loses crystallinity at room temperature in air or under oil over a period of ~1 hr. Data were collected on a large plate of approximate dimensions $0.56 \times 0.44 \times 0.24$ mm^3. Raw area detector data frames were reduced and corrected for absorption effects using the SAINT+ and SADABS programs. Final unit cell parameters were determined by least-squares refinement of 9691 reflections taken from the data set. The structure was solved by direct methods with SHELXT. Subsequent difference Fourier calculations and full-matrix least-squares refinement against F^2 were performed with SHELXL-2014 using OLEX2.

The compound crystallizes in the monoclinic system. The pattern of systematic absences in the intensity data was consistent with the space group $P2_1/c$, which was verified by structure solution. The asymmetric unit consists of one CoCl(C$_{57}$H$_{36}$F$_{51}$N$_7$)$^+$ cation, one chloride ion, three THF molecules of crystallization, and two water molecules. The crystal is afflicted with extensive disorder, affecting primarily the long fluorinated chains, but also interstitial solvent species. Two of the three independent -C$_8$F$_{17}$ arms of the C$_{57}$H$_{36}$F$_{51}$N$_7$ ligand show pronounced positional disorder. The disorder was modeled

with two components for chains C31-C38/F18-F34 and C50-C57/F35-F51. No disorder

was modeled for the third chain (C12-C19/F1-F17), but d(C-C) = 1.55(2) Å and d(C-F) =

1.35 Å distance restraints were applied, in addition to rigid-bond restraints (RIGU) for

the C and F displacement parameters. The largest residual electron density peaks

remaining after convergence are located near atoms of this arm, but trial modeling

showed the minor disorder fraction to be small, *ca.* < 20%, and difficulty was

encountered in achieving a stable model. This is the reason the single 'average' positional

model for this ligand arm was retained. The geometry of the other two -C_8F_{17} arms was

then restrained to have similar 1,2- and 1,3- C-C and C-F distances using SHELX SAME

instructions. Rigid-bond (RIGU) restraints were also applied to the anisotropic

displacement parameters of atoms in these chains. One THF molecule (O3S) was

restrained to adopt a similar geometry as the more well-ordered THF molecule O2S. The

two water molecules are each disordered over two closely spaced positions, whose total

occupancy was constrained to 1.0. In total 1116 restraints were used for the disorder

modeling. All non-hydrogen atoms were refined with anisotropic displacement

parameters except for the solvent species (isotropic). Hydrogen atoms bonded to carbon

were in general located in difference maps before being included as riding atoms.

Hydrogen atoms of the water molecules could not be located and were not calculated.

The largest residual electron density peak in the final difference map is 1.03 $e^-/Å^3$,

located 1.30 Å from F^2.
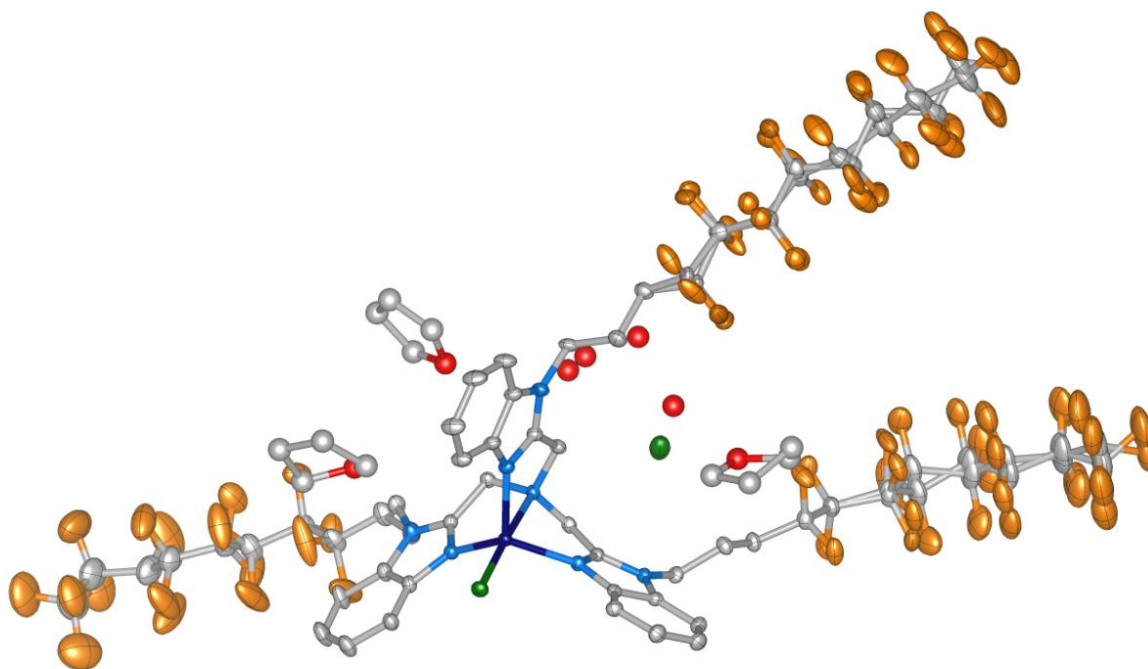
Figure 3.21 X-ray single crystal structure of **Co-(BimC₃F₈)₃**. Hydrogen atoms are omitted for clarity. Cobalt (dark blue), nitrogen (blue), carbon (gray), chloride (green), oxygen (red) and fluorine (orange).
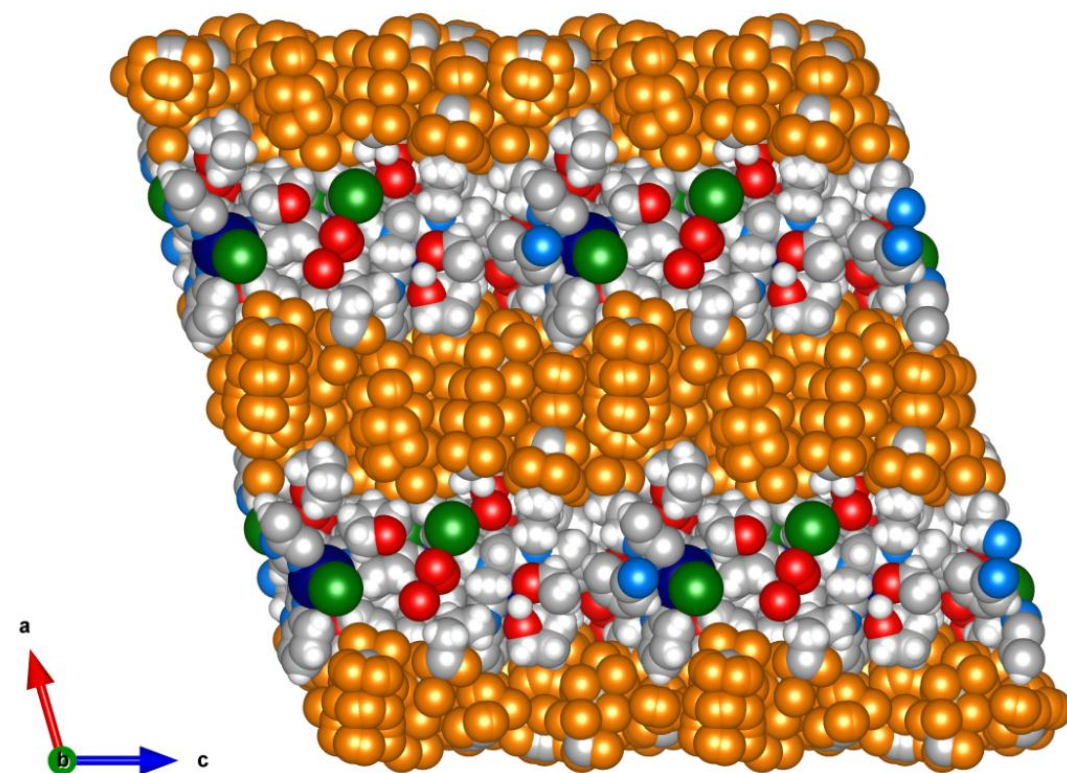
Figure 3.22 Packing viewed down the *b* axis (Van Der Waals space-filling). Cobalt (dark blue), nitrogen (blue), carbon (gray), chloride (green), oxygen (red), hydrogen (white) and fluorine (orange).
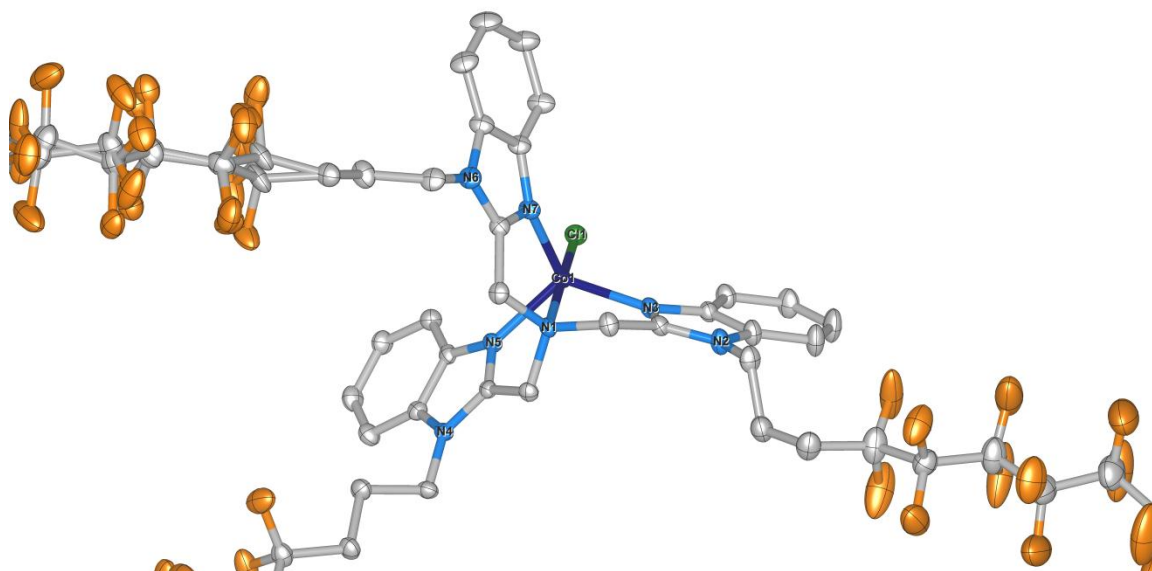
Figure 3.23 The coordination center of **Co-(BimC₃F₈)₃**. Hydrogen atoms, counter ions and solvents are omitted for clarity. Cobalt (dark blue), nitrogen (blue), carbon (gray), chloride (green) and fluorine (orange).

Table 3.3 Crystal Data and Structure Refinement Details for **Co-(BimC₃F₈)₃**.

Identification code	**Co-(BimC$_3$F$_8$)$_3$**
Empirical formula	C$_{69}$H$_{63}$Cl$_2$CoF$_{51}$N$_7$O$_5$
Formula weight	2169.10
Temperature/K	200(2)
Crystal system	monoclinic
Space group	P2$_1$/c
a/Å	24.5991(11)
b/Å	14.5605(6)
c/Å	25.6393(11)
α/°	90
β/°	106.1210(10)

γ/°	90
Volume/Å^3	8822.2(7)
Z	4
ρcalcg/cm^3	1.634
μ/mm^{-1}	0.414
F(000)	4348.0
Crystal size/mm^3	0.56 × 0.44 × 0.24
Radiation	MoKα (λ = 0.71073)
2Θ range for data collection/°	4.31 to 50.052
Index ranges	-29 ≤ h ≤ 29, -17 ≤ k ≤ 17, -30 ≤ l ≤ 30
Reflections collected	439740
Independent reflections	15563 [R$_{int}$ = 0.0758, R$_{sigma}$ = 0.0183]
Data/restraints/parameters	15563/1116/1397
Goodness-of-fit on F^2	1.057
Final R indexes [I>=2σ (I)]	R$_1$ = 0.0871, wR$_2$ = 0.2466
Final R indexes [all data]	R$_1$ = 0.1033, wR$_2$ = 0.2662
Largest diff. peak/hole / e Å^{-3}	1.03/-0.78

Table 3.4 Selected bond distances and angles of **Co-(BimC$_3$F$_8$)$_3$**.

Bond Length/Å			
Co1-N1	2.332(3)	Co1-N3	2.033(4)
Co1-N5	2.048(3)	Co1-N7	2.025(3)
Co1-Cl1	2.2975(11)		
Angle/°			
Cl1-Co1-N1	177.18(9)	N3-Co1-Cl1	103.34(10)
N3-Co1-N1	76.37(13)	N3-Co1-N5	119.90(14)
N5-Co1-Cl1	102.66(10)	N5-Co1-N1	75.24(13)
N7-Co1-Cl1	106.77(10)	N7-Co1-N1	75.82(13)
N7-Co1-N3	113.45(14)	N7-Co1-N5	109.15(14)

3.2.4 Conclusions

In conclusion, we have successfully immobilized the molecular water-oxidation catalyst **Co-(BimC$_3$F$_8$)$_3$** on the surface of an FTO electrode by exploiting its extreme hydrophobicity. The catalyst retained its molecular nature on the surface. To date, **Co-(BimC$_3$F$_8$)$_3$** is the most efficient Co-based molecular catalyst reported for the electrocatalytic oxidation of water at neutral pH in terms of overpotential, TOF, and long-term stability. The utilization of extreme hydrophobicity for immobilization and conformational lock-in of flexible molecular catalysts on the surfaces is general, broadly applicable to other electrocatalytic systems, and has the potential to enable the development of "ideal" anodes for economically relevant photo/electrocatalytic water splitting.

3.3 Understanding the Catalytic Pathway by DFT Computation

In order to better understand the catalytic pathway of water oxidation catalyzed by our catalysts, a DFT calculation was also performed.

In **Section** 错误!未找到引用源。, we proposed that the superior catalytic activity of **Co-(BimC$_3$F$_8$)$_3$** among the catalysts library（错误!未找到引用源。）was mainly ascribed to the immobilization of the catalysts on FTO electrode via hydrophobicity. For the catalysts with different N-alkylated tails, their electronic structures didn't vary from

each other significantly. Herein, we should be able to gain an insight by study the simplest **Co-(BimH)₃** catalyst.

3.3.1 The Establishment of Coupled Equilibria

Co^{IV} species have been widely considered as the active species for the water nucleophilic attack (WNA) step in the cobalt catalyzed water oxidation. The O–O bond formation product of WNA could further release O_2 and regenerate the initial Co^{II} catalyst. In our catalytic system, the activation path way of the initial catalyst **[Co^{II}]$^+$** to the O–O bond forming **[Co^{IV}=O]$^+$** specie may be characterized by considering the coupled equilibria in **Scheme 3.5**.[108-110]
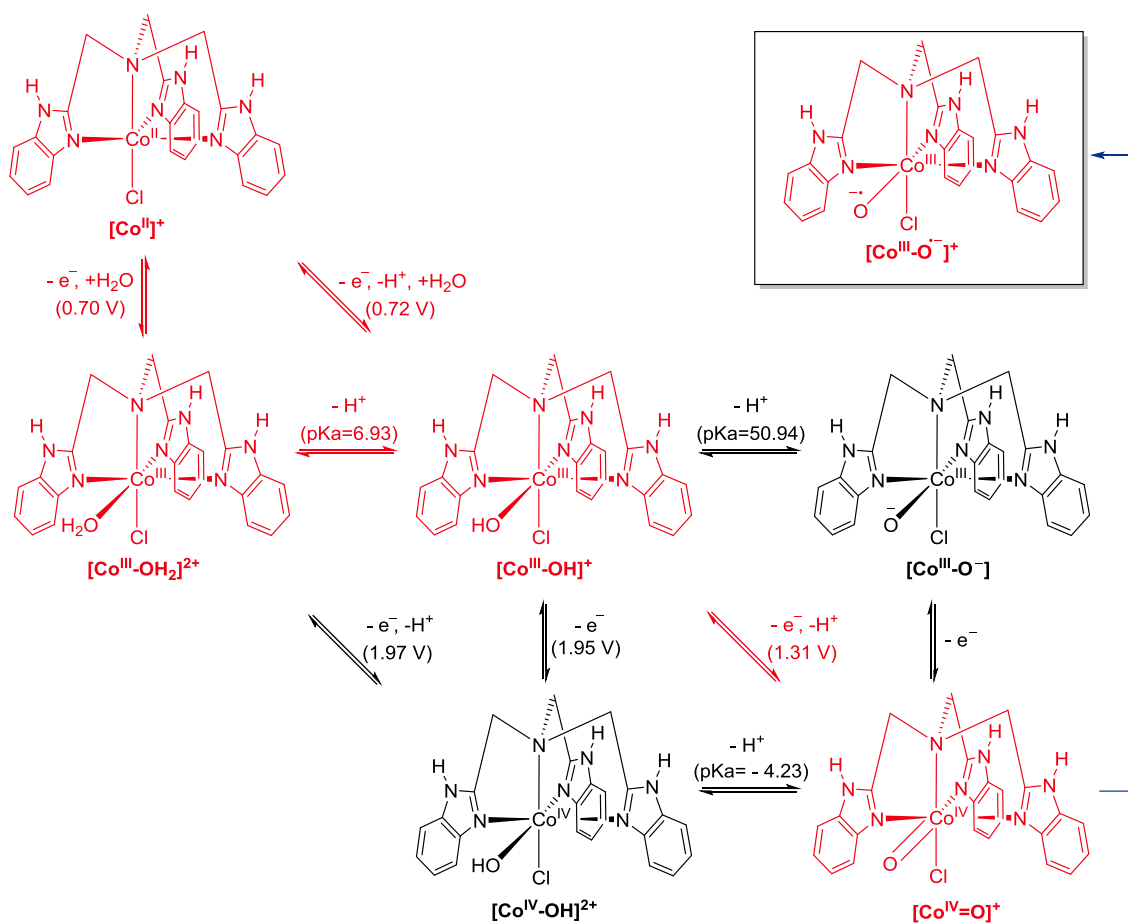
Scheme 3.5 Plausible intermediates involved in the PCET process from $[\mathbf{Co^{II}}]^+$ (upper left) to $[\mathbf{Co^{IV}=O}]^+$ (bottom right) species. Vertical equilibria are correlated to one-electron reductions and diagonal equilibria are correlated to PCET (expressed as standard reduction potentials vs. SHE at pH=7); Horizontal equilibria are correlated to the dissociation of a proton (expressed as pKa values). Later Mulliken spin density analysis indicated that $[\mathbf{Co^{IV}=O}]^+$ should be better expressed as $[\mathbf{Co^{III}-O^{\cdot-}}]^+$ (see **Section 3.3.2**).

In **Scheme 3.5**, the upper left is the initial catalyst $[\mathbf{Co^{II}}]^+$ and the bottom right is the $[\mathbf{Co^{IV}=O}]^+$ specie which was supposed to be able to mediate the WNA process. The horizontal steps represent acid-base equilibria, their free energies were presented as pKa

values. The vertical steps represent one-electron redox reactions, their free energies were expressed as standard reduction potentials vs. SHE at pH=7. The diagonal steps represent PCET equilibria and were also expressed as standard reduction potentials.

By carefully evaluation of each possible intermediate and equilibria, we are able to identify an energetically feasible path from the initial $[Co^{II}]^+$ to $[Co^{IV}=O]^+$, as shown in **Scheme 3.5**, the favorable intermediates and equilibria were marked as red. The standard redox potential of the first PCET process from $[Co^{II}]^+$ to $[Co^{III}-OH]^+$ was calculated as only 0.72 V vs. SHE at pH=7, quite close to the one-electron transfer process from $[Co^{II}]^+$ to $[Co^{III}-OH_2]^{2+}$, which was 0.70 V. The coordination of a H_2O ligand to the cobalt(III) center significantly lower its pKa value, which was only 6.93. The dissociation of a proton to sequentially generate $[Co^{III}-OH]^+$ also quite facile. However, both the one electron reduction and one proton dissociation of $[Co^{III}-OH]^+$ to $[Co^{IV}-OH]^+$ and $[Co^{III}-O^-]^+$ were found to be too energetically, which were 1.95 V and 50.94 (pKa) separately. Instead, the PCET process from $[Co^{III}-OH]^+$ to $[Co^{IV}=O]^+$ was only 1.31 V, which is much more energetically feasible.

3.3.2 Investigation of Mulliken Spin Density

The analysis of the spin density (**Figure 3.24** and **Table 3.5**) shows that the spin distribution of the bottom right intermediate (**Scheme 3.5**) is not consistent with a $[Co^{IV}=O]^+$, but rather $[Co^{III}-O^{\cdot-}]^+$. In both $[Co^{II}]^+$ and $[Co^{III}-O^{\cdot-}]^+$, the spin distribution on the **(BimH)$_3$** ligand and Cl ligand are negligible. Thus, the PCET step starting from $[Co^{III}-OH]^+$ leads to $[Co^{III}-O^{\cdot-}]^+$ instead of $[Co^{IV}=O]^+$.

(A)

(B)

(C)

(D)
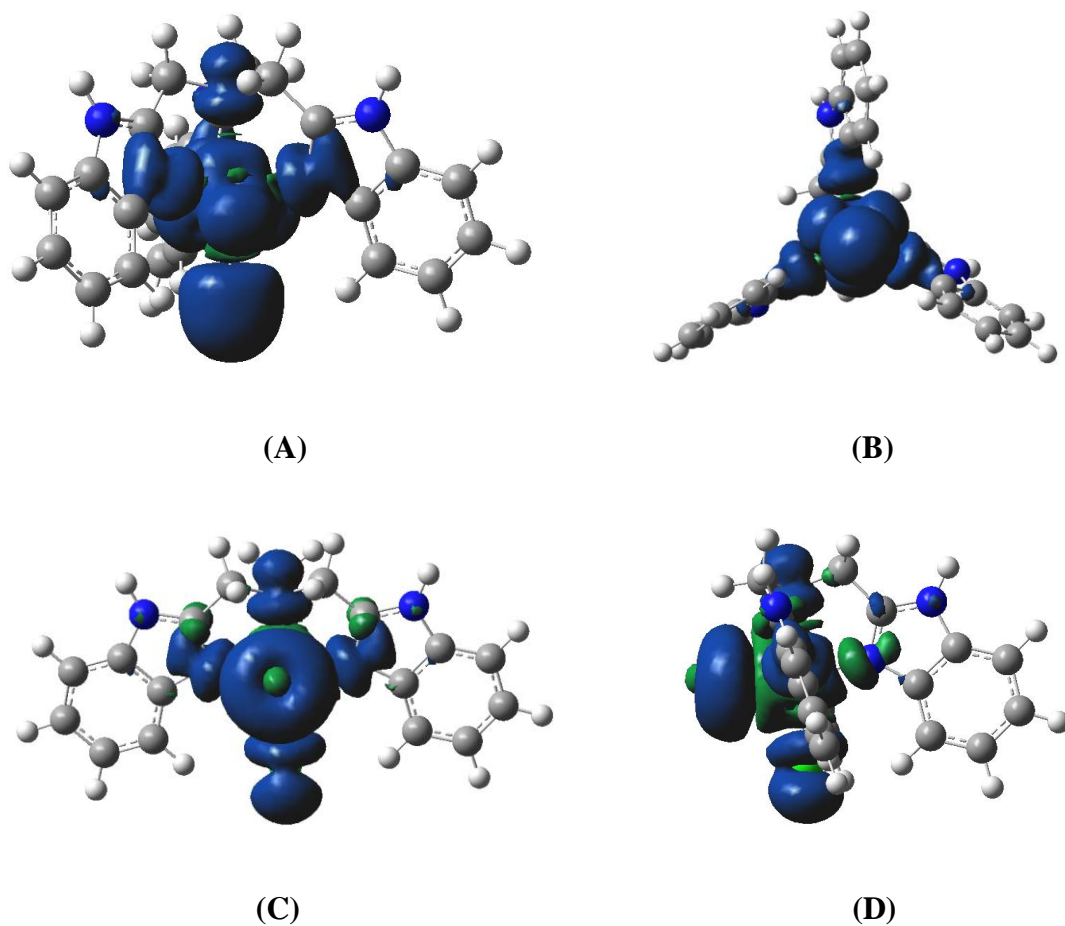
Figure 3.24 Different views of spin density plots for (A&B) $[Co^{II}]^+$ and (C&D) $[Co^{IV}=O]^+$ (actually is $[Co^{III}-O^{\cdot-}]^+$) at the B3LYP/6-31G(d)/SDD level of theory.

Table 3.5 B3LYP Mulliken spin densities (a.u.) on selected units of $[Co^{II}]^+$ and $[Co^{IV}=O]^+$ (actually is $[Co^{III}-O^{\cdot-}]^+$).

	Co	**(BimH)$_3$**	Cl	O
$[Co^{II}]^+$	2.72	0.16	0.12	-
$[Co^{IV}=O]^+$ or $[Co^{III}-O^{\cdot-}]^+$	1.88	0.12	0.09	0.90

3.3.3 Frontier Molecular Orbitals of $[Co^{III}\text{-}O^{\cdot-}]^+$.

The investigation of the frontier molecular orbitals of $[Co^{III}\text{-}O^{\cdot-}]^+$ (**Figure 3.25**), especially the LUMO (**Figure 3.25D**) indicating that the p shape orbital of the oxygen atom was capable to receive the nucleophilic attack from a p shape HOMO of a water molecule.

(A) HOMO-1   **(B)** HOMO
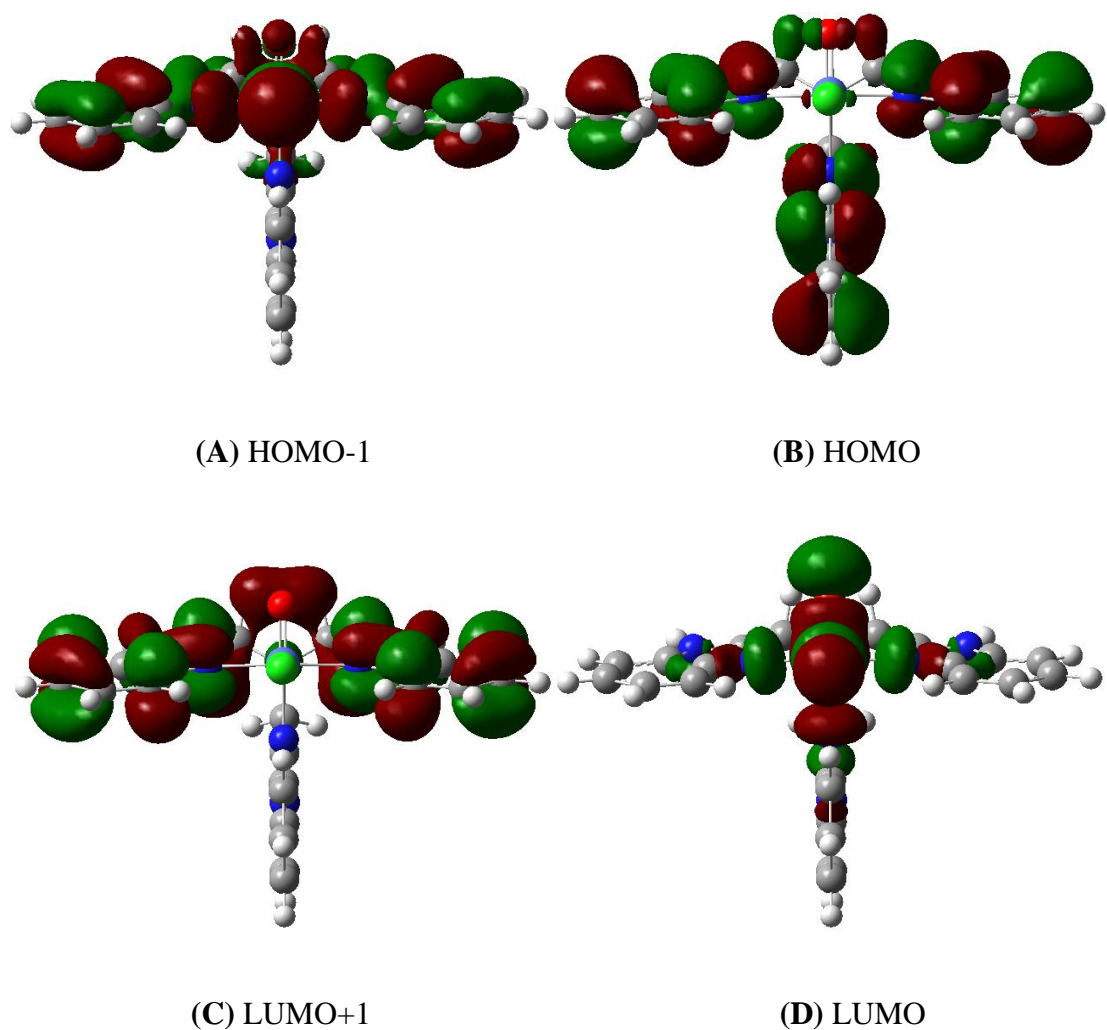
(C) LUMO+1   **(D)** LUMO

Figure 3.25 B3LYP/6-31G(d)/SDD molecular orbital plots for $[Co^{III}\text{-}O^{\cdot-}]^+$. (A) HOMO-1; (B) HOMO; (C) LUMO+1; (D) LUMO.

3.3.4 Transition States of the WNA on $[Co^{III}\text{-}O^{\cdot-}]^{+}$.

We were able to locate a TS structure $[Co^{III}\text{-}O^{\cdot-}]^{+} \text{-} H_2O^{\ddagger}$ (**Figure 3.26**) by introducing a first-solvation-shell water molecule[111, 112] to the WNA process of $[Co^{III}\text{-}O^{\cdot-}]^{+}$. The Co–O and O–O bonds are 1.786 Å and 1.839 Å separately. The activation energy associated with WNA for $[Co^{III}\text{-}O^{\cdot-}]^{+} \text{-} H_2O^{\ddagger}$ is predicted to be 18.6 kcal/mol (**Scheme 3.6**). The experimental rate of the best catalysts in our library **Co-(BimC₃F₈)₃** is 1.83 s^{-1}, according to Eyring equation,

$$k = \frac{k_B T}{h} e^{-\frac{\Delta G^{\neq}}{RT}}$$

it suggests that for the rate determining step at 298 K, the maximum activation free energy is 17.1 kcal/mol, which is quite close to the calculated activation barrier (only with a difference of 1.5 kcal/mol). Based on these results, we proposed that the key O–O bond formation step involves oxidation of the starting $[Co^{II}]^{+}$ specie to reach $[Co^{III}\text{-}O^{\cdot-}]^{+}$, then followed by a water nucleophilic attack.
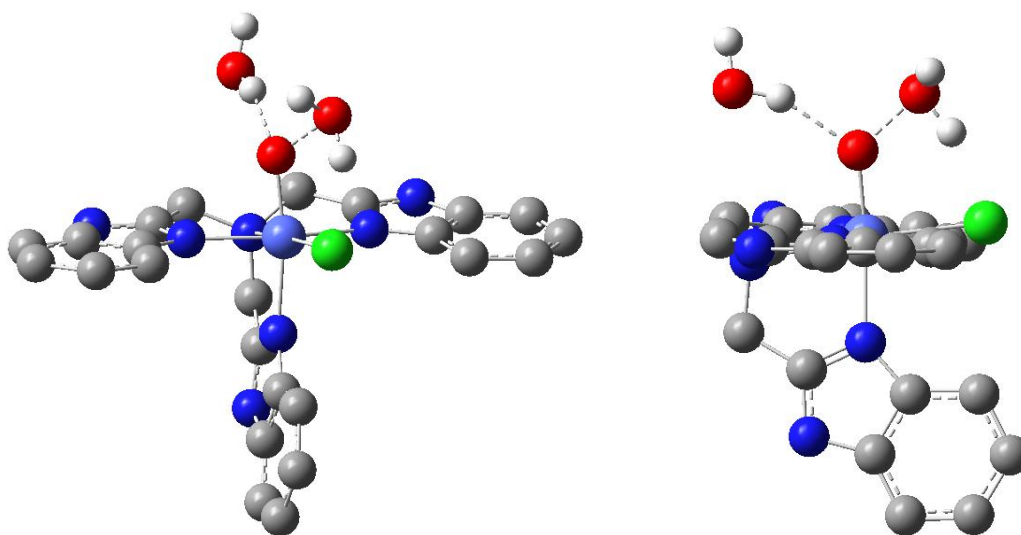
Figure 3.26 Different views of transition state structures $[Co^{III}\text{-}O^{\cdot-}]^+ \cdot H_2O^{\ddagger}$, a first-solvation-shell water molecule was also included (r_{Co-O}: 1.786 Å; r_{O-O}: 1.839 Å). For clarity, hydrogen atoms of the ligand were omitted. Colors for atoms: C (gray), H (white), N (blue), O (red), Cl (green) and Co (gray blue).
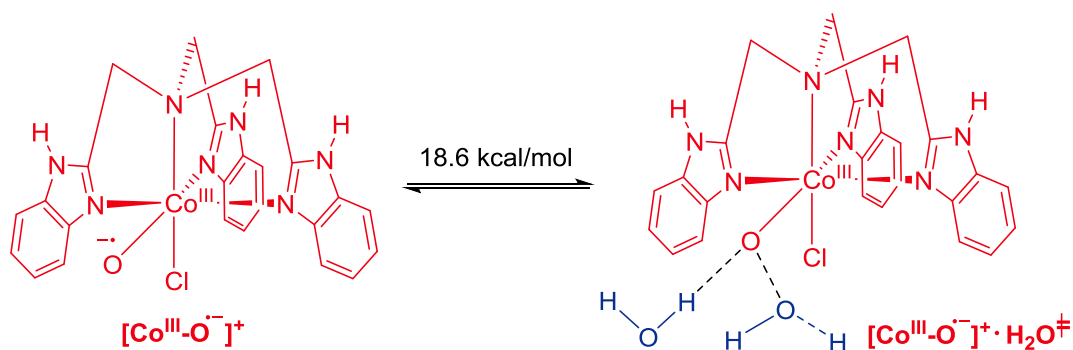
Scheme 3.6 The activation barrier of the water nucleophilic attack of $[Co^{III}\text{-}O^{\cdot-}]^+$.

While the experimental TOF value of **Co-(BimH)₃** is negligible, and taking account that the electronic properties of **Co-(BimH)₃** and **Co-(BimC₃F₈)₃** are similar, these results reinforced that the turn over activity difference between **Co-(BimH)₃** and its N-

alkylated derivatives are mainly due to their immobility on electrode, and such immobility could be ascribed to their hydrophobicity.

3.3.5 Experimental Section

3.3.5.1 Computational Methods

All DFT calculations were carried out using the Gaussian 09 package.[113] Geometry optimizations were performed with the B3LYP[114-116] functional using the 6-31G* basis set.[117] Cobalt was represented with the Stuttgart [8s7p6d2f|6s5p3d2f] ECP10MDF contracted pseudopotential basis set.[118, 119] All geometries were verified by vibrational frequency analysis. Thermal correction of free energy were added to single-point M06-L[120-122] electronic energies computed with the 6-311+G(2df,p) basis set on main group atoms and the SDD basis set on Co. Solvation effects associated with water as solvent were accounted for using the SMD continuum solvation model.[123] Redox potential and pKa calculations followed the receipt from Cramer group.[110, 112]

3.3.5.2 Optimized Geometries

Figure 3.27 to **Figure 3.33** shows the optimized geometries of all the intermediates investigated in the present study. For each structure, two different views were presented. All the hydrogen atoms from the **(BimH)₃** ligand are omitted for clarity. Colors of atoms: C (gray), H (white), N (blue), O (red), Cl (green) and Co (gray blue).
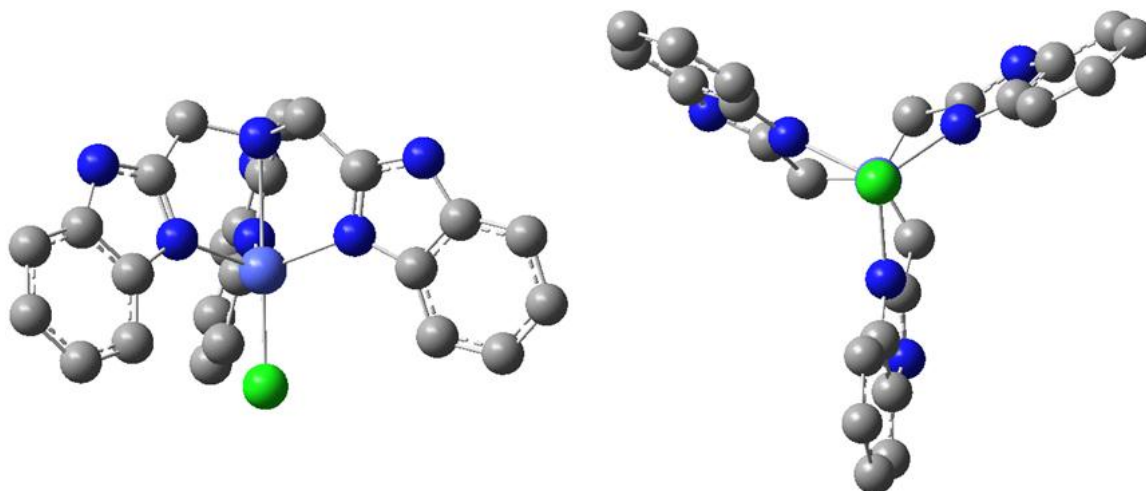
Figure 3.27 Optimized geometry of $[Co^{II}]^+$.
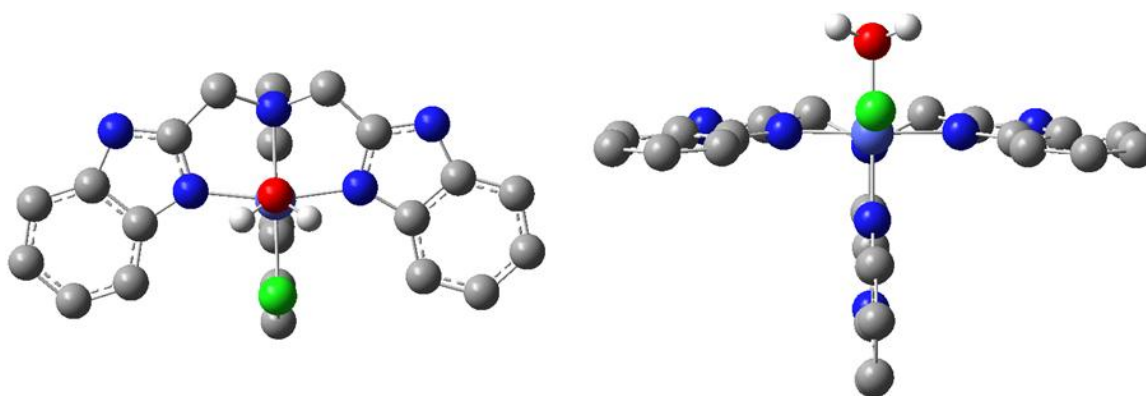
Figure 3.28 Optimized geometry of $[Co^{III}\text{-}H_2O]^{2+}$.
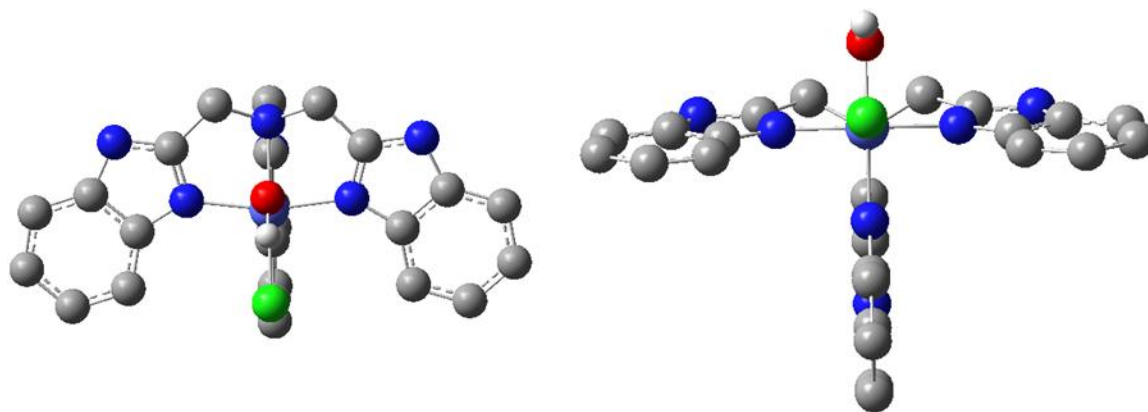
Figure 3.29 Optimized geometry of **[Co^{III}-OH]$^+$**.
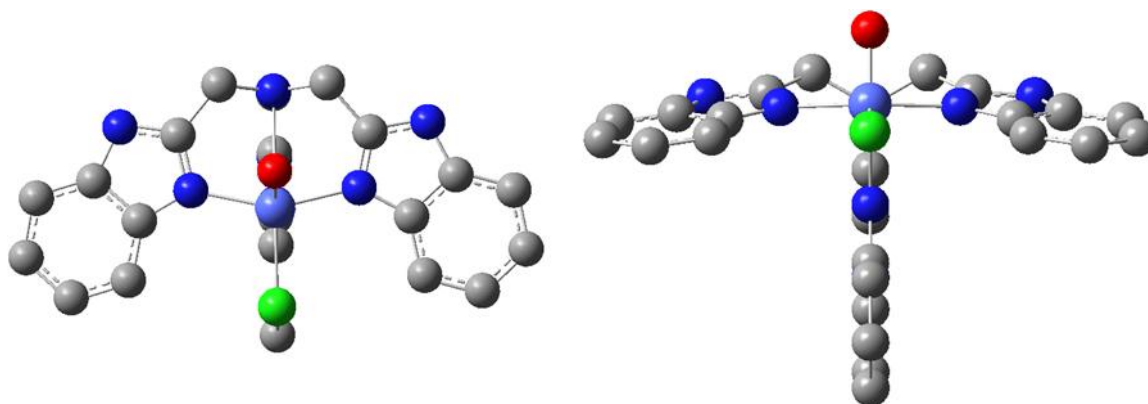
Figure 3.30 Optimized geometry of **[Co^{III}-O$^-$]**.
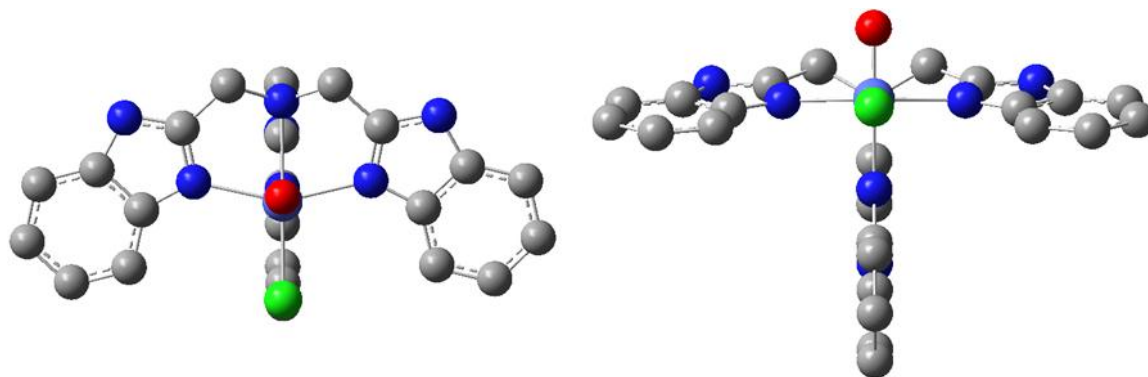
Figure 3.31 Optimized geometry of **[Co^{III}-O$^{\cdot-}$]$^+$**.
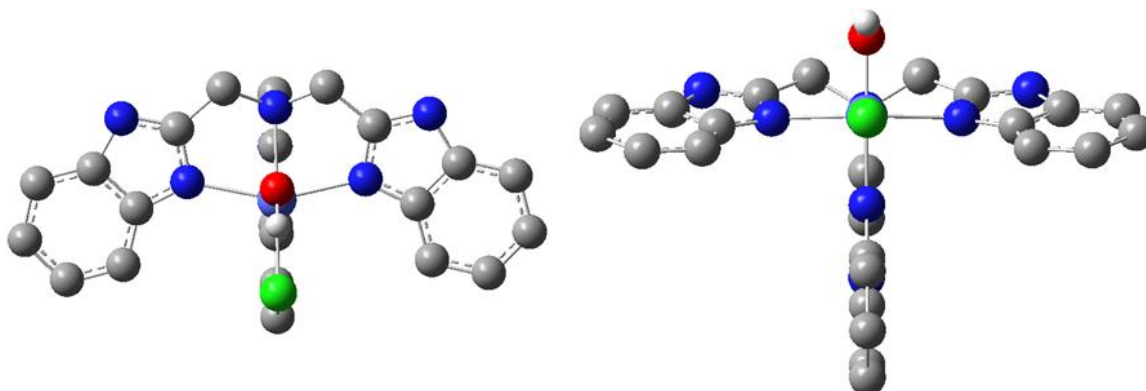
Figure 3.32 Optimized geometry of $[\text{Co}^{IV}\text{-OH}]^{2+}$.
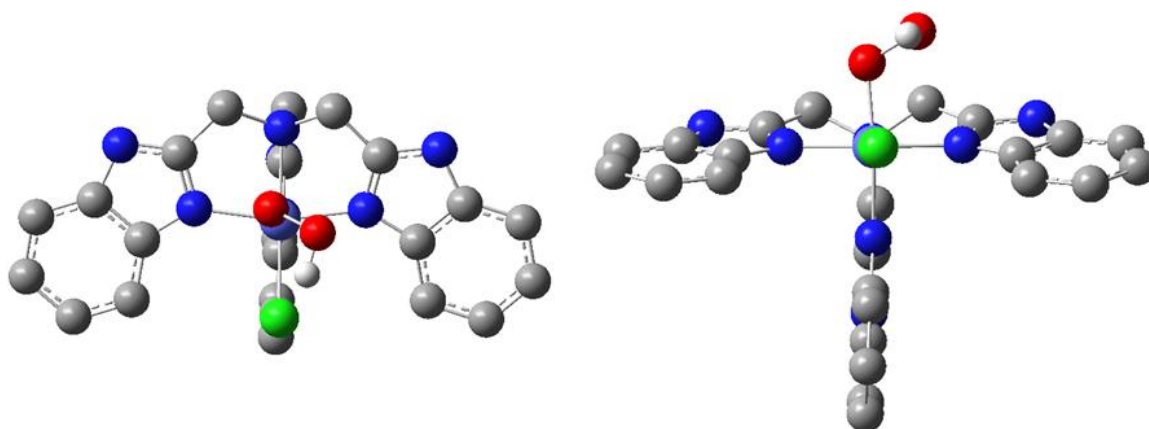
Figure 3.33 Optimized geometry of $[\text{Co}^{III}\text{-OOH}]^{+}$.

3.3.6 Conclusions

In **Section 3.3**, DFT calculation identified an energetically feasible pathway starting from the initial $[\text{Co}^{II}]^{+}$ catalyst to the active WNA specie $[\text{Co}^{III}\text{-O}^{\cdot-}]^{+}$. A transition state of the O−O bond forming water nucleophilic attack on $[\text{Co}^{III}\text{-O}^{\cdot-}]^{+}$ was also successfully located, with an activation barrier of 18.6 kcal/mol. All these study indicates that **Co-(BimH)$_3$** should be an active catalyst for electrocatalytic water oxidation, however, its experimental turnover activity was indeed negligible. In contrast, **Co-(BimC$_3$F$_8$)$_3$**, which

has the similar electron structure with **Co-(BimH)$_3$,** shown a TOF of 1.83 s^{-1}. These results reinforced that the immobilization of a catalyst on electrode is one of the most important point to achieve a better design of water oxidation catalyst.

APPENDICES - Materials and Methods

Materials:

All reagents and solvents were provided by commercial suppliers (Sigma-Aldrich, Fisher Scientific, Alfa Aesar and VWR) and used without further purification, unless otherwise noted.

Nuclear Magnetic Resonance Spectroscopy (NMR):

^{1}H, ^{13}C, and ^{19}F spectra were obtained at 298 K using Bruker AVQ 700 MHz, 600 MHz, 500 MHz or 400 MHz instruments. Chemical shifts are reported as δ (ppm) values, using either TMS or residual solvent peaks as an internal standard, and coupling constants (*J*) as Hz values.

Gas Chromatography - Mass Spectrometry (GC-MS):

GC-MS analyses were performed on an Agilent 7820A gas chromatograph equipped with a 30m $\times$ 0.25mm HP-5MS capillary column (25μ film thickness) and an Agilent 5975C mass-selective detector.

Size Exclusion Chromatography (SEC):

The molecular weight and the molecular weight distribution of polymers were determined from SEC using an Agilent liquid chromatography system fitted with refractive index (RID) and UV-Vis detectors, using two identical PLgel columns (5 μm, MIXED-C) in connected series with THF as the mobile phase (1 mL/min). The column

and flow path were temperature controlled at 25 ℃. Data analysis was performed using GPC-Addon for ChemStation software from Agilent.

Mass Spectrometry (MS):

Mass spectra are acquired using electrospray ionization (ESI) with an Agilent 6130 Quadrupole LC-MS instrument. HRMS analyses were performed in the Analytical Core Lab, 4700 King Abdullah University of Science and Technology, Thuwal, 23955-6900, Saudi Arabia.

Dissolved Oxygen Measurements (DO):

Dissolved oxygen was measured using a Mettler Toledo SG6 SevenGO Pro instrument with an Inlab 605 dissolved oxygen probe.

Dynamic Light Scattering (DLS):

DLS measurements were performed to determine the size distribution of monomer aggregates in solution or bulk using a Malvern Zetasizer Nano ZS instrument equipped with a 632.8 nm He-Ne laser. The measurement angle was 173°. The cells were temperature-controlled at 25 ±0.1 ℃.

Atomic Force Microscopy (AFM):

AFM images were obtained on an Agilent 5400 SPM instrument in tapping mode, using Pico View software. Silicon cantilevers were obtained from Bruker (k = 42 N/m; fo = 320 kHz; T: 4um; L: 125 um; W: 40 um). Gwyddion 2.33 was used for data analysis and visualization of AFM images.

Transmission Electron Microscopy (TEM):

Imaging was performed on a Titan G2 80–300 kV transmission electron microscope (FEI Inc.) equipped with a 4 k×4 k CCD camera (US4000, Gatan, Inc.). Cryo-TEM: Imaging was performed with a low dose on a Titan Krios operating at 300 kV. Images were recorded in zero loss imaging mode using an energy filter (GIF Tridiem, Gatan, Inc) with a slit width of 20 eV.

Attenuated Total Reflectance–Fourier Transform Infrared Spectroscopy (ATR-FTIR):

A Thermo Scientific Nicolet 6700 instrument, equipped with nitrogen purge and aligned for signal clarity, was used to collect the data. The instrument was calibrated before sampling against a newly cleaned (acetone) and dried crystal surface. 32 Scans from 4000 to 550 cm^{-1} were recorded for each sample.

Ultraviolet-Visible Absorption Spectroscopy (UV-Vis):

UV-Vis spectra were recorded using a JASCO spectrophotometer at room temperature. The wavelength was recorded from 800 – 200 nm at a scan speed of 400 nm/min and a data interval of 1 nm.

Contact angle

Contact angles were measured using a contact angle goniometer (KRUSS EasyDrop Standard) at ambient pressure and temperature; static angle measurements were made from 1-µl drops of deionized water on the surface of silicon wafer slides modified with Co-trisbenzimidazole complexes.

Electrochemical measurements

Electrochemical measurements were performed on a BioLogic Science Instrument potentiostat electrochemical workstation in a glass cell equipped with an FTO working electrode (effective area 1 cm^2), a spiral Pt counter electrode and an Ag/AgCl (in saturated KCl electrolyte) reference electrode. Cyclic voltammetry (CV) and controlled potential bulk electrolysis (CPE) were performed in pH-buffered aqueous solutions at room temperature. The water used in all experiments was distilled and deionized by a Milli-Q system from Millipore; pH was measured using a pH electrode from Fisher Scientific.

Oxygen evolution was measured by GC analysis (TCD detector). The turnover number (TON) and frequency (TOF) were calculated from the amount of oxygen detected and the amount of cobalt loading, yielding a value for the amount of oxygen formed per cobalt and per second.

TON = mol O_2 (after 8 hour)/mol Co

TOF = mol O_2/s/mol Co

Faradaic efficiency was calculated with respect to the theoretical amount of oxygen produced. The amount of oxygen produced was in turn calculated using the steady-state current obtained from controlled potential electrolysis, in which the current is given in electrons passed per second. Assuming water oxidation is a four-electron process, this value is divided by four to give the amount of oxygen formed per second.

Theoretical amount of oxygen:

$$\text{mol } O_2/s = \frac{I\,(A)}{F*4}$$

F= Faradaic constant = 9.64853399×10^4 A s / mol

Faradaic efficiency = measured amount of oxygen $\times$ 100 / theoretical amount of oxygen

REFERENCES

1.   Hydrophobe. https://en.wikipedia.org/wiki/Hydrophobe#Superhydrophobicity.

2.   Silverstein, T. P., *J. Chem. Educ.* **1998,** *75* (1), 116-118.

3.   Fluorocarbon. https://en.wikipedia.org/wiki/Fluorocarbon.

4.   Hamza, M. A.; Serratrice, G.; Stebe, M. J.; Delpuech, J. J., *J. Am. Chem. Soc.* **1981,** *103* (13), 3733-3738.

5.   Fersht, A., *Structure and mechanism in protein science : a guide to enzyme catalysis and protein folding*. W.H. Freeman: New York, 1999; p xxi, 631 p.

6.   Rose, G. D.; Fleming, P. J.; Banavar, J. R.; Maritan, A., *Proc. Natl. Acad. Sci. USA*. **2006,** *103* (45), 16623-16633.

7.   Whittaker, J. W., *Chem. Rev.* **2003,** *103* (6), 2347-2363.

8.   Que, L.; Tolman, W. B., *Nature* **2008,** *455* (7211), 333-340.

9.   Israelachvili, J. N., *Intermolecular and surface forces*. 3rd ed.; Academic Press: Burlington, MA, 2011; p xxx, 674 p.

10.   Dwars, T.; Paetzold, E.; Oehme, G., *Angew. Chem. Int. Edit.* **2005,** *44* (44), 7174-7199.

11.   La Sorella, G.; Strukul, G.; Scarso, A., *Green Chem.* **2015,** *17* (2), 644-683.

12.   Grätzel, M.; Kalyanasundaram, K., *Kinetics and catalysis in microheterogeneous systems*. M. Dekker: New York, 1991; p xii, 525 p.

13.   Vriezema, D. M.; Aragones, M. C.; Elemans, J. A. A. W.; Cornelissen, J. J. L. M.; Rowan, A. E.; Nolte, R. J. M., *Chem. Rev.* **2005,** *105* (4), 1445-1489.

14.   Förch, R.; Schönherr, H.; Jenkins, A. T. A., *Surface design : applications in bioscience and nanotechnology*. Wiley-VCH: Weinheim, 2009; p xxiii, 511 p.

15.   Liu, F. J.; Kong, W. P.; Qi, C. Z.; Zhu, L. F.; Xiao, F. S., *ACS Catal.* **2012,** *2* (4), 565-572.

16.   Noshadi, I.; Kumar, R. K.; Kanjilal, B.; Parnas, R.; Liu, H.; Li, J. T.; Liu, F. J., *Catal. Lett.* **2013,** *143* (8), 792-797.

17. Corma, A.; Domine, M.; Gaona, J. A.; Jorda, J. L.; Navarro, M. T.; Rey, F.; Perez-Pariente, J.; Tsuji, J.; McCulloch, B.; Nemeth, L. T., *Chem. Commun.* **1998,** (20), 2211-2212.

18. Tojo, G.; Fernández, M., *Oxidation of alcohols to aldehydes and ketones*. Springer: New York, NY, 2010.

19. Shi, Z. Z.; Zhang, C.; Tang, C. H.; Jiao, N., *Chem. Soc. Rev.* **2012,** *41* (8), 3381-3430.

20. Parmeggiani, C.; Cardona, F., *Green Chem.* **2012,** *14* (3), 547-564.

21. Semmelhack, M. F.; Schmid, C. R.; Cortes, D. A.; Chou, C. S., *J. Am. Chem. Soc.* **1984,** *106* (11), 3374-3376.

22. Gamez, P.; Arends, I. W. C. E.; Sheldon, R. A.; Reedijk, J., *Adv. Synth. Catal.* **2004,** *346* (7), 805-811.

23. Hoover, J. M.; Stahl, S. S., *J. Am. Chem. Soc.* **2011,** *133* (42), 16901-16910.

24. Allen, S. E.; Walvoord, R. R.; Padilla-Salinas, R.; Kozlowski, M. C., *Chem. Rev.* **2013,** *113* (8), 6234-6458.

25. Sheldon, R. A., Green Catalytic Oxidations in Water. In *Metal-Catalyzed Reactions in Water*, Dixneuf, P. H.; Cadierno, V., Eds. Wiley-VCH: Weinheim, 2013; pp 139-172.

26. ten Brink, G. J.; Arends, I. W. C. E.; Sheldon, R. A., *Science* **2000,** *287* (5458), 1636-1639.

27. Figiel, P. J.; Sibaouih, A.; Ahmad, J. U.; Nieger, M.; Raisanen, M. T.; Leskela, M.; Repo, T., *Adv. Synth. Catal.* **2009,** *351* (16), 2625-2632.

28. Zhang, G.; Han, X.; Luan, Y.; Wang, Y.; Wen, X.; Xu, L.; Ding, C.; Gao, J., *RSC Adv* **2013,** *3* (42), 19255-19258.

29. Mugemana, C.; Chen, B. T.; Bukhryakov, K. V.; Rodionov, V., *Chem. Commun.* **2014,** *50* (58), 7862-7865.

30. Harth, E. M.; Hecht, S.; Helms, B.; Malmstrom, E. E.; Frechet, J. M. J.; Hawker, C. J., *J. Am. Chem. Soc.* **2002,** *124* (15), 3926-3938.

31. Hecht, S.; Frechet, J. M. J., *Angew. Chem. Int. Edit.* **2001,** *40* (1), 74-91.

32. Dichtel, W. R.; Baek, K. Y.; Frechet, J. M. J.; Rietveld, I. B.; Vinogradov, S. A., *J. Polym. Sci. Pol. Chem* **2006,** *44* (17), 4939-4951.

33.   Koda, Y.; Terashima, T.; Nomura, A.; Ouchi, M.; Sawamoto, M., *Macromolecules.* **2011,** *44* (12), 4574-4578.

34.   Marsat, J. N.; Heydenreich, M.; Kleinpeter, E.; Berlepsch, H. V.; Bottcher, C.; Laschewsky, A., *Macromolecules.* **2011,** *44* (7), 2092-2105.

35.   Dias, A. M. A.; Freire, M.; Coutinho, J. A. P.; Marrucho, I. M., *Fluid. Phase. Equilibr* **2004,** *222*, 325-330.

36.   Riess, J. G., *Chem. Rev.* **2001,** *101* (9), 2797-2919.

37.   Chan, T. R.; Hilgraf, R.; Sharpless, K. B.; Fokin, V. V., *Org. Lett.* **2004,** *6* (17), 2853-2855.

38.   Donnelly, P. S.; Zanatta, S. D.; Zammit, S. C.; White, J. M.; Williams, S. J., *Chem. Commun.* **2008,** (21), 2459-2461.

39.   Schweinfurth, D.; Demeshko, S.; Khusniyarov, M. M.; Dechert, S.; Gurram, V.; Buchmeiser, M. R.; Meyer, F.; Sarkar, B., *Inorg. Chem.* **2012,** *51* (14), 7592-7597.

40.   Hawker, C. J.; Bosman, A. W.; Harth, E., *Chem. Rev.* **2001,** *101* (12), 3661-3688.

41.   Matyjaszewski, K.; Xia, J. H., *Chem. Rev.* **2001,** *101* (9), 2921-2990.

42.   Charleux, B.; Nicolas, J.; Guerret, O., *Macromolecules.* **2005,** *38* (13), 5485-5492.

43.   Bosman, A. W.; Vestberg, R.; Heumann, A.; Frechet, J. M. J.; Hawker, C. J., *J. Am. Chem. Soc.* **2003,** *125* (3), 715-728.

44.   Ott, C.; Hoogenboom, R.; Schubert, U. S., *Chem. Commun.* **2008,** (30), 3516-3518.

45.   Lacroix-Desmazes, P.; Andre, P.; Desimone, J. M.; Ruzette, A. V.; Boutevin, B., *J. Polym. Sci. Pol. Chem* **2004,** *42* (14), 3537-3552.

46.   Chen, B. T.; Bukhryakov, K. V.; Sougrat, R.; Rodionov, V. O., *ACS Catal.* **2015,** *5* (2), 1313-1317.

47.   Horvath, I. T., *Accounts. Chem. Res.* **1998,** *31* (10), 641-650.

48.   Ragagnin, G.; Betzemeier, B.; Quici, S.; Knochel, P., *Tetrahedron* **2002,** *58* (20), 3985-3991.

49.   Gheorghe, A.; Cuevas-Yanez, E.; Horn, J.; Bannwarth, W.; Narsaiah, B.; Reiser, O., *Synlett* **2006,** (17), 2767-2770.

50.   Hoover, J. M.; Ryland, B. L.; Stahl, S. S., *ACS Catal.* **2013,** *3* (11), 2599-2605.

51.   Kumpulainen, E. T. T.; Koskinen, A. M. P., *Chem-eur. J.* **2009,** *15* (41), 10901-10911.

52.   Sjoblom, J.; Blokhus, A. M.; Wei, M. S.; Friberg, S. E., *J. Colloid Interf. Sci* **1990,** *140* (2), 481-491.

53.   Furuya, T.; Strom, A. E.; Ritter, T., *J. Am. Chem. Soc.* **2009,** *131* (5), 1662-1663.

54.   Zheng, J.; Lin, S. Y.; Zhu, X. H.; Jiang, B. W.; Yang, Z.; Pan, Z. Y., *Chem. Commun.* **2012,** *48* (50), 6235-6237.

55.   Liu, J. X.; Ma, S. M., *Org. Lett.* **2013,** *15* (20), 5150-5153.

56.   Lin, C. K.; Lu, T. J., *Tetrahedron* **2010,** *66* (51), 9688-9693.

57.   Lewis, N. S.; Nocera, D. G., *Proc. Natl. Acad. Sci. USA.* **2006,** *103* (43), 15729-15735.

58.   Cook, T. R.; Dogutan, D. K.; Reece, S. Y.; Surendranath, Y.; Teets, T. S.; Nocera, D. G., *Chem. Rev.* **2010,** *110* (11), 6474-6502.

59.   Eisenberg, R.; Gray, H. B., *Inorg. Chem.* **2008,** *47* (6), 1697-1699.

60.   Hurst, J. K., *Science* **2010,** *328* (5976), 315-316.

61.   Kärkäs, M. D.; Verho, O.; Johnston, E. V.; Åkermark, B., *Chem. Rev.* **2014,** *114* (24), 11863-12001.

62.   Gersten, S. W.; Samuels, G. J.; Meyer, T. J., *J. Am. Chem. Soc.* **1982,** *104* (14), 4029-4030.

63.   Duan, L.; Bozoglian, F.; Mandal, S.; Stewart, B.; Privalov, T.; Llobet, A.; Sun, L., *Nature Chem.* **2012,** *4*, 418-423.

64.   Mola, J.; Mas-Marza, E.; Sala, X.; Romero, I.; Rodríguez, M.; Viñas, C.; Parella, T.; Llobet, A., *Angew. Chem. Int. Edit.* **2008,** *47* (31), 5830-5832.

65.   Wang, L.; Fan, K.; Daniel, Q.; Duan, L.; Li, F.; Philippe, B.; Rensmo, H.; Chen, H.; Sun, J.; Sun, L., *Chem. Commun.* **2015,** *51* (37), 7883-7886.

66.   deKrafft, K. E.; Wang, C.; Xie, Z.; Su, X.; Hinds, B. J.; Lin, W., *ACS Appl. Mater. Inter.* **2012,** *4* (2), 608-613.

67.   Harriman, A.; Pickering, I. J.; Thomas, J. M.; Christensen, P. A., *Journal of the Chemical Society, Faraday Transactions* **1988,** *84* (8), 2795-2806.

68.   Chen, Z.; Concepcion, J. J.; Jurss, J. W.; Meyer, T. J., *J. Am. Chem. Soc.* **2009,** *131* (43), 15580-15581.

69.   Chen, Z.; Concepcion, J. J.; Meyer, T. J., *Dalton Trans.* **2011,** *40* (15), 3789-3792.

70.   Esswein, A. J.; Surendranath, Y.; Reece, S. Y.; Nocera, D. G., *Energy & Environmental Science* **2011,** *4* (2), 499-504.

71.   Kanan, M. W.; Nocera, D. G., *Science* **2008,** *321* (5892), 1072-1075.

72.   Jiao, F.; Frei, H., *Energy & Environmental Science* **2010,** *3* (8), 1018-1027.

73.   Roger, I.; Symes, M. D., *J. Am. Chem. Soc.* **2015,** *137* (43), 13980-13988.

74.   Han, Y.; Wu, Y.; Lai, W.; Cao, R., *Inorg. Chem.* **2015,** *54* (11), 5604-5613.

75.   Okamura, M.; Kondo, M.; Kuga, R.; Kurashige, Y.; Yanai, T.; Hayami, S.; Praneeth, V. K. K.; Yoshida, M.; Yoneda, K.; Kawata, S.; Masaoka, S., *Nature* **2016,** *530*, 465-468.

76.   Fillol, J. L.; Codolà, Z.; Garcia-Bosch, I.; Gómez, L.; Pla, J. J.; Costas, M., *Nature Chem.* **2011,** *3* (10), 807-813.

77.   Chebotareva, N.; Nyokong, T., *Electrochim. Acta* **1997,** *42* (23‚Äì24), 3519 - 3524.

78.   Nakazono, T.; Parent, A. R.; Sakai, K., *Chem. Commun.* **2013,** *49* (56), 6325-6327.

79.   Han, A.; Wu, H.; Sun, Z.; Jia, H.; Du, P., *Phys. Chem. Chem. Phys.* **2013,** *15* (30), 12534-12538.

80.   Singh, A.; Chang, S. L. Y.; Hocking, R. K.; Bach, U.; Spiccia, L., *Energy & Environmental Science* **2013,** *6* (2), 579-586.

81.   Surendranath, Y.; Nocera, D. G., *Prog. Inorg. Chem.* **2011**, 505-560.

82.   Cao, R.; Lai, W.; Du, P., *Energy & Environmental Science* **2012,** *5* (8), 8134-8157.

83.   Hurst, J. K.; Cape, J. L.; Clark, A. E.; Das, S.; Qin, C., *Inorg. Chem.* **2008,** *47* (6), 1753-1764.

84.   Wang, D.; Groves, J. T., *Proceedings of the National Academy of Sciences* **2013,** *110* (39), 15579-15584.

85.   Xien, L.; Fengying, W., *Coordin. Chem. Rev.* **2012,** *256*, 1115 - 1136.

86.   Dau, H.; Limberg, C.; Reier, T.; Risch, M.; Roggan, S.; Strasser, P., *ChemCatChem* **2010,** *2* (7), 724-761.

87.   Brimblecombe, R.; Dismukes, G. C.; Swiegers, G. F.; Spiccia, L., *Dalton Trans.* **2009,** (43), 9374-9384.

88.   Vannucci, A. K.; Alibabaei, L.; Losego, M. D.; Concepcion, J. J.; Kalanyan, B.; Parsons, G. N.; Meyer, T. J., *Proceedings of the National Academy of Sciences* **2013,** *110* (52), 20918-20922.

89.   Lei, H.; Han, A.; Li, F.; Zhang, M.; Han, Y.; Du, P.; Lai, W.; Cao, R., *Phys. Chem. Chem. Phys.* **2014,** *16* (5), 1883-1893.

90.   Wasylenko, D. J.; Palmer, R. D.; Schott, E.; Berlinguette, C. P., *Chem. Commun.* **2012,** *48* (15), 2107-2109.

91.   Stracke, J. J.; Finke, R. G., *J. Am. Chem. Soc.* **2011,** *133* (38), 14872-14875.

92.   Hong, D.; Mandal, S.; Yamada, Y.; Lee, Y.-M.; Nam, W.; Llobet, A.; Fukuzumi, S., *Inorg. Chem.* **2013,** *52* (16), 9522-9531.

93.   Morlanés, N.; Joya, K. S.; Takanabe, K.; Rodionov, V., *Eur. J. Inorg. Chem.* **2015,** *2015* (1), 49-52.

94.   Brimblecombe, R.; Bond, A. M.; Dismukes, G. C.; Swiegers, G. F.; Spiccia, L., *Phys. Chem. Chem. Phys.* **2009,** *11* (30), 6441-6449.

95.   Wada, T.; Tanaka, K., *Eur. J. Inorg. Chem.* **2005,** *2005* (19), 3832-3839.

96.   Thompson, L. K.; Ramaswamy, B. S.; Seymour, E. A., *Canadian Journal of Chemistry* **1977,** *55* (5), 878-88.

97.   Cariou, R.; Chirinos, J. J.; Gibson, V. C.; Jacobsen, G.; Tomov, A. K.; Britovsek, G. J. P.; White, A. J. P., *Dalton Trans.* **2010,** *39* (38), 9039-9045.

98.   Rodionov, V. O.; Presolski, S. I.; Gardinier, S.; Lim, Y.; Finn, M. G., *J. Am. Chem. Soc.* **2007,** *129* (42), 12696-12704.

99.   Hotchkiss, P. J.; Jones, S. C.; Paniagua, S. A.; Sharma, A.; Kippelen, B.; Armstrong, N. R.; Marder, S. R., *Accounts. Chem. Res.* **2011,** *45* (3), 337-346.

100.   Dogutan, D. K.; McGuire, R.; Nocera, D. G., *J. Am. Chem. Soc.* **2011,** *133* (24), 9178-9180.

101.   Surendranath, Y.; Kanan, M. W.; Nocera, D. G., *J. Am. Chem. Soc.* **2010,** *132* (46), 16501-16509.

102.   Hyde, J. T.; Hanson, K.; Vannucci, A. K.; Lapides, A. M.; Alibabaei, L.; Norris, M. R.; Meyer, T. J.; Harrison, D. P., *ACS Appl. Mater. Inter.* **2015,** *7* (18), 9554-9562.

103. Rodionov, V. O.; Presolski, S. I.; Gardinier, S.; Lim, Y. H.; Finn, M. G., *J. Am. Chem. Soc.* **2007,** *129* (42), 12696-12704.

104. Ichikawa, K.; Nakata, K.; Ibrahim, M. M., *Chem. Lett.* **2000,** (7), 796-797.

105. Phillips, M. A., *J. Chem. Soc.* **1928**, 2393-2399.

106. O'Shaughnessy, J.; Aldabbagh, F., *Synthesis* **2005,** (7), 1069-1076.

107. Cariou, R.; Chirinos, J. J.; Gibson, V. C.; Jacobsen, G.; Tomov, A. K.; Britovsek, G. J. P.; Whitea, A. J. P., *Dalton Trans.* **2010,** *39* (38), 9039-9045.

108. Yang, X. F.; Baik, M. H., *J. Am. Chem. Soc.* **2004,** *126* (41), 13222-13223.

109. Yang, X. F.; Baik, M. H., *J. Am. Chem. Soc.* **2008,** *130* (48), 16231-16240.

110. Ertem, M. Z.; Cramer, C. J., *Dalton Trans.* **2012,** *41* (39), 12213-12219.

111. Bozoglian, F.; Romain, S.; Ertem, M. Z.; Todorova, T. K.; Sens, C.; Mola, J.; Rodriguez, M.; Romero, I.; Benet-Buchholz, J.; Fontrodona, X.; Cramer, C. J.; Gagliardi, L.; Llobet, A., *J. Am. Chem. Soc.* **2009,** *131* (42), 15176-15187.

112. Ertem, M. Z.; Gagliardi, L.; Cramer, C. J., *Chem. Sci.* **2012,** *3* (4), 1293-1299.

113. Frisch, M. J.; Trucks, G. W.; Schlegel, H. B.; Scuseria, G. E.; Robb, M. A.; Cheeseman, J. R.; Scalmani, G.; Barone, V.; Mennucci, B.; Petersson, G. A.; Nakatsuji, H.; Caricato, M.; Li, X.; Hratchian, H. P.; Izmaylov, A. F.; Bloino, J.; Zheng, G.; Sonnenberg, J. L.; Hada, M.; Ehara, M.; Toyota, K.; Fukuda, R.; Hasegawa, J.; Ishida, M.; Nakajima, T.; Honda, Y.; Kitao, O.; Nakai, H.; Vreven, T.; Montgomery Jr., J. A.; Peralta, J. E.; Ogliaro, F.; Bearpark, M. J.; Heyd, J.; Brothers, E. N.; Kudin, K. N.; Staroverov, V. N.; Kobayashi, R.; Normand, J.; Raghavachari, K.; Rendell, A. P.; Burant, J. C.; Iyengar, S. S.; Tomasi, J.; Cossi, M.; Rega, N.; Millam, N. J.; Klene, M.; Knox, J. E.; Cross, J. B.; Bakken, V.; Adamo, C.; Jaramillo, J.; Gomperts, R.; Stratmann, R. E.; Yazyev, O.; Austin, A. J.; Cammi, R.; Pomelli, C.; Ochterski, J. W.; Martin, R. L.; Morokuma, K.; Zakrzewski, V. G.; Voth, G. A.; Salvador, P.; Dannenberg, J. J.; Dapprich, S.; Daniels, A. D.; Farkas, Ö.; Foresman, J. B.; Ortiz, J. V.; Cioslowski, J.; Fox, D. J. *Gaussian 09*, Gaussian, Inc.: Wallingford, CT, USA, 2009.

114. Becke, A. D., *Phys. Rev. A* **1988,** *38* (6), 3098-3100.

115. Becke, A. D., *J. Chem. Phys.* **1993,** *98* (7), 5648-5652.

116. Lee, C. T.; Yang, W. T.; Parr, R. G., *Phys. Rev. B* **1988,** *37* (2), 785-789.

117. Hehre, W. J., *Ab initio molecular orbital theory*. Wiley: New York, 1986; p xviii, 548 p.

118.   Dolg, M.; Wedig, U.; Stoll, H.; Preuss, H., *J. Chem. Phys.* **1987,** *86* (2), 866-872.

119.   Martin, J. M. L.; Sundermann, A., *J. Chem. Phys.* **2001,** *114* (8), 3408-3420.

120.   Zhao, Y.; Truhlar, D. G., *J. Chem. Phys.* **2006,** *125* (19).

121.   Zhao, Y.; Truhlar, D. G., *Accounts. Chem. Res.* **2008,** *41* (2), 157-167.

122.   Zhao, Y.; Truhlar, D. G., *Theor. Chem. Acc.* **2008,** *120* (1-3), 215-241.

123.   Marenich, A. V.; Cramer, C. J.; Truhlar, D. G., *J. Phys. Chem. B* **2009,** *113* (18), 6378-6396.